ANALYSIS ON THE EFFECT OF TRENCH GEOMETRY ON FILM COOLING EFFECTIVENESS OF SHAPED HOLES USING RANS SIMULATION

K. P. Pasan Sanjeeva

(178260A)

Degree of Master of Engineering

Department of Mechanical Engineering

University of Moratuwa
Sri Lanka

February 2022

ANALYSIS ON THE EFFECT OF TRENCH GEOMETRY ON FILM COOLING EFFECTIVENESS OF SHAPED HOLES USING RANS SIMULATION

Karnuna Pathirannehelage Pasan Sanjeeva

(178260A)

Thesis submitted in partial fulfillment of the requirements for the degree of Master of Engineering in Mechanical Engineering

Department of Mechanical Engineering

University of Moratuwa
Sri Lanka

February 2022

DECLARATION

I declare that this is my own work and this thesis does not incorporate without acknowledgement any material previously submitted for a Degree or Diploma in any other University or institute of higher learning and to the best of my knowledge and belief it does not contain any material previously published or written by another person except where the acknowledgement is made in the text.

Also, I hereby grant to University of Moratuwa the non-exclusive right to reproduce and distribute my thesis, in whole or in part in print, electronic or other medium. I retain the right to use this content in whole or part in future works (such as articles or books).

Signature: Date:

Name of Student: K P P Sanjeeva Registration No: 178260A

The above candidate has carried out research for the Master's thesis under my supervision.

Name of the supervisor: Dr. R. A. C. P. Ranasinghe

Signature of the supervisor: Date:

Abstract

Diffused shaped holes have shown superior cooling performance over the other shapes of holes in many situations. In the present study, numerical simulation using realizable k-ε model with enhanced wall treatments as implemented in Ansys Fluent solver was performed to study the effect of trench geometry made at 7-7-7 shaped hole exit on cooling effectiveness. The predictions were generated at different depth ratios of the trench geometry. Three different blowing ratios of M = 1.5, 3, and 5 were employed with different depth ratios of h/D = 0.25, 0.5, and 1. Altogether nine cases were run to generate predictions and three cases without trench, h/D = 0, at different blowing ratios of M = 1.5, 3, and 5 were run as the baseline. All cases were maintained at density ratio of DR = 1.5 and turbulence intensity or Tu = 0.5%.

Based on the error analyses and the comparisons performed to flow field patterns and cooling effectiveness variations during the validation, the realizable k-ε model with enhanced wall treatment was selected among standard k-ω, SST k-ω and realizable k-ε for predictions. When compared to the baseline, not only the modified geometry presents better cooling effectiveness according to the laterally averaged effectiveness, but superior lateral spreading of coolant can also be observed at higher depth ratio of trench. Maintaining higher blowing ratios at lower slot depth ratio such as h/D = 0.25 is only a waste of coolant without improvements to cooling effectiveness while higher cooling effectiveness can be obtained by higher blowing ratios at higher trench depth ratios. Based on the laterally averaged effectiveness, the cooling effectiveness is improved by increasing the trench depth at all blowing ratios investigated. Based on the lateral effectiveness variations, the coolant jet has shown a skewness at higher blowing ratios and lower trench depth ratios while the skewness becomes invisible at lower blowing ratios and lower trench depths. A steeper decay can be observed in laterally averaged effectiveness at high blowing ratios (M = 5) and low slot depth ratios (h/D = 0.25) due to the jet penetration into mainstream thereby degrading the cooling performance.

Key words: *cooling effectiveness, film cooling, shaped hole, trench geometry, turbulence modeling*

Acknowledgements

It is great pleasure for me to acknowledge all the advices, guidance and assistance rendered to me by all the lecturers of the Department of Mechanical Engineering, University of Moratuwa.

Secondly, I would like to express my deepest appreciation to my supervisor Dr. R. A. C. P. Ranasinghe for his advice, patience aspiration and devotion to complete the work. I would like to express my sincere appreciation to our course coordinator, non-academic staff and all the students of the MEng/PGDip in Energy Technology program, those who gave me the fullest support in my studies.

I profoundly thank my wife Mrs. Jayani Rajatheja who has sacrificed her valuable time and relived me from my responsibilities as a husband in many domestic matters. I respectfully acknowledge my father and mother who supported me in every possible ways.

Finally, I would like to express my appreciation to everyone who contributes with aspiration or in actual work to the success of completion of studies related to this academic program.

K. P. P. Sanjeeva

Thank You,

Department of Mechanical Engineering,

University of Moratuwa.

Table of Contents

List of Figures

List of Tables

Symbols and Abbreviations

Symbols

A	Hole cross-sectional area
AR	Area ratio, A_{exit}/A_{inlet}
D	Film cooling hole diameter
M	Blowing ration, $\rho_c U_c/\rho_\infty U_\infty$
DR	Density ratio, ρ_c/ρ_∞
h	Depth of trench
k	Turbulent kinetic energy
L	Hole length
P	Lateral distance between holes, pitch
R	Radius of diffused outlet interior edges
t	Hole breakout width
Tu	Free-stream turbulence
T	Temperature
α	Injection angle of film hole
β_{fwd}	Laidback angle for diffused outlet
β_{lat}	Lateral expansion of film hole
ε	Turbulence dissipation rate
γ	Specific heat ratio
ω	Specific turbulence dissipation rate
η	Adiabatic film cooling effectiveness, $(T_\infty - T_{aw})/(T_\infty - T_c)$
η_{th}	Thermal efficiency
x	Downstream distance measured from the hole exit
y	Vertical distance from the surface
z	Lateral distance measured from center line

Subscripts

aw	Adiabatic wall
c	Coolant at hole inlet
f	With film cooling
w	Wall
0	Without film cooling
∞	Free-stream

Abbreviation

CRVP	Counter Rotating Vortex Pair
LES	Large Eddy Simulation
RANS	Reynolds Averaged Navier Ststokes
RKE	Realizable k-ε
RSM	Reynolds Stress Models
STW	Standard k-ω
SST KW	Shear Stress Transport k-ω
URANS	Unsteady Reynolds Averaged Navier Ststokes
RMSE	Root-Mean Squared Error

1 INTRODUCTION

Gas turbine engine is the heart of aircraft population and power generation sector in the world. Therefore designing high performance gas turbine engines is a vital task in their applications. According to the Brayton cycle analysis, thermal efficiency as well as power output depends on turbine inlet temperature. As shown in Figure 1-1, the engine specific power output increases when increasing turbine rotor inlet temperature. The ideal performance line represents an engine working perfectly without any losses. As shown in Figure 1-1, several gas turbine engines such as Von ohain, whittle, J42, JT8D etc. have been illustrated how their turbine inlet temperatures increases with increasing specific power output.

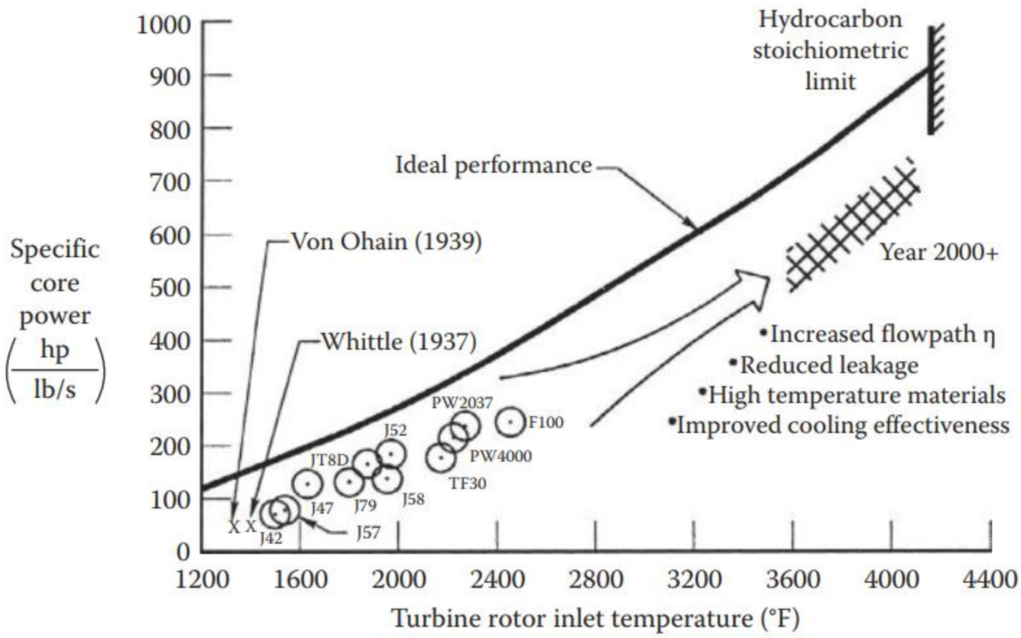

Figure 1-1: Turbine power output as a function of the turbine inlet temperature [1]

Equation 1-1 shows the thermal efficiency for gas turbine engine based on the Brayton cycle using cold-air-standard assumptions [2].

$$\boldsymbol{\eta_{th} = 1 - \frac{1}{r_p^{\frac{\gamma-1}{\gamma}}}} \quad \text{-------------} \ \mathbf{1\text{-}1}$$

r_p is the pressure ratio through the compressor and γ is specific heat ratio. If the pressure ratio is increased thermal efficiency increases according the above expression [2]. For a given power output, higher pressure ratios increase the thermal efficiency of the engine without changing engine size [3]. Engine size depends on the mass flow through the engine [3]. Enclosed area of the power cycle on T-s diagram as shown in Figure 1-2, which is temperature and specific entropy diagram , represents the power output per unit mass flow [2] [3]. Turbine inlet temperature gets increased when increasing pressure ratio since the combustion happens under high pressure [2]. Figure 1-2 shows 0-3/-4/-5/ cycle with increased pressure ratio and it has the same enclosed area as the shaded cycle of 0-3-4-5 maintaining the same power output per unit mass flow rate through the engine and keeping the engine size constant. To increase the thermal efficiency while keeping same combustion temperature to avoid formation of NO_X, turbine inlet temperature at 4 should be increased to 4/.

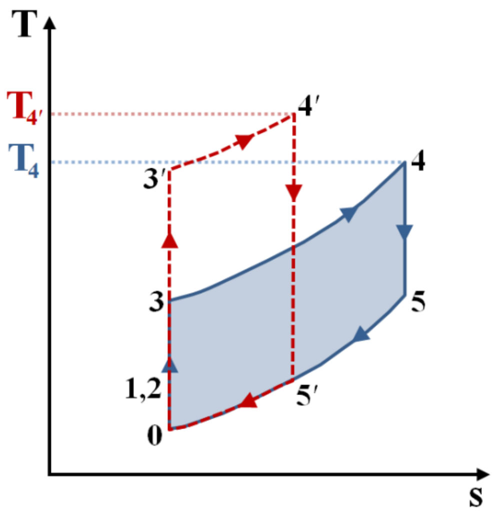

Figure 1-2: Ideal Brayton Cycle [3]

However, increasing turbine inlet temperature is limited in terms of material technology of turbine blade/vane since the melting temperature of the metal is achieved by the turbine inlet temperature (Figure 1-3). Therefore development of thermal barrier coatings and sophisticated turbine cooling technologies has become a vital aspect of gas turbine design and development process.

1.1 Turbine blade cooling

The engine cooling systems are responsible to ensure that thermal stresses of the blade are minimized by reducing temperature gradients and blade surface temperature. It increases the life of the design and maintains the safe operating conditions. The coolant often the air is extracted from the compressor and directed to the blade cooling system. Too little amount of coolant flow reduces the life of the components while too high amount of cooling flow reduces the engine performance. Therefore optimum coolant flow must be obtained to increase the cooling performance thus protecting components of the blade. The turbine inlet temperature is in excess of 1600 ^{0}C in advanced military engines [4]. Cooling systems in the turbine components use 20%-30% of total fluid flow in the turbine [4].

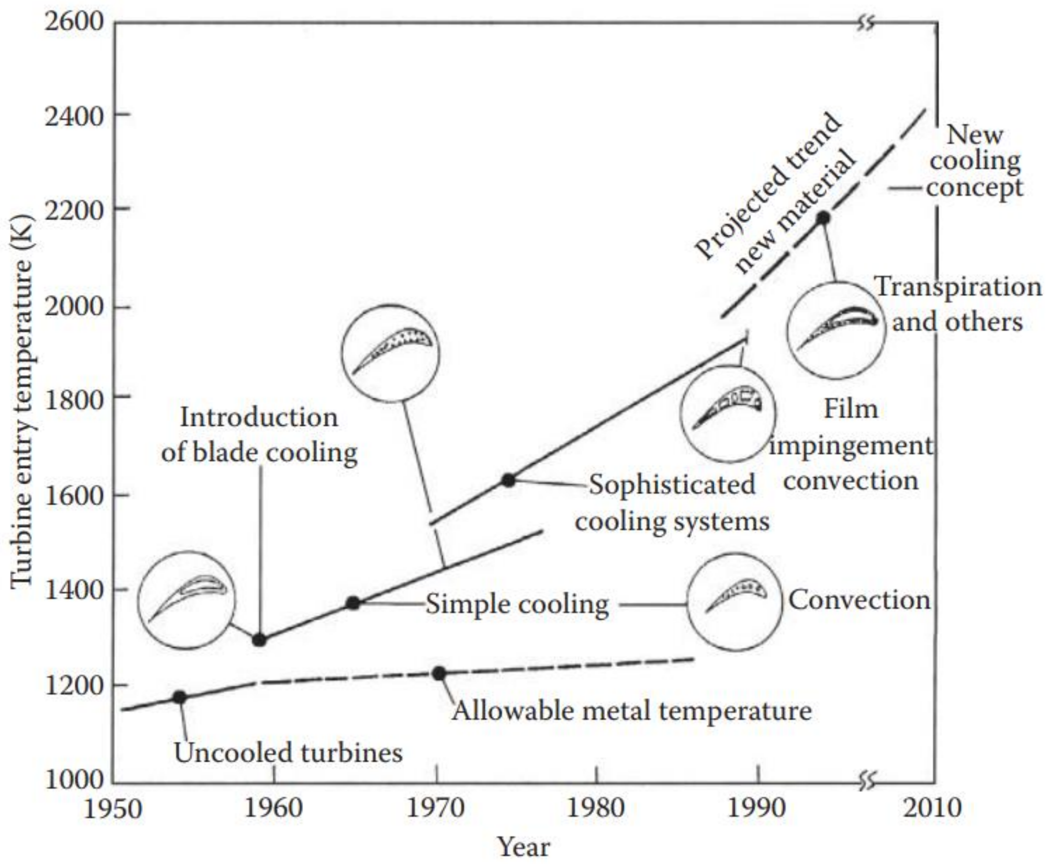

Figure 1-3: Turbine inlet temperature over the years [1]

There are two types of cooling methods which are internal and external (Figure 1-4). Internal cooling uses internal passages of the blade such that the coolant flows through the passages. On the other hand, discrete holes made on the blade surface are sued in external cooling. The coolant with high pressure inside the blade passages injects to the hot mainstream. After that, a thin coolant film is formed on the surface thereby protecting blade surface. As a result of that, convective heat flux associated with the hot surface is reduced by the thin film layer. Land-based gas turbines are utilized film cooling method with excess of 1400 ^{0}C as one of the popular cooling technologies [4].

1.2 Film cooling

Internal passages of the gas turbine blade used convective cooling methods during the initial stage of turbine cooling [4]. These methods used compressor bleed air with high pressure and the coolant circulates through the convection passages inside the blade.

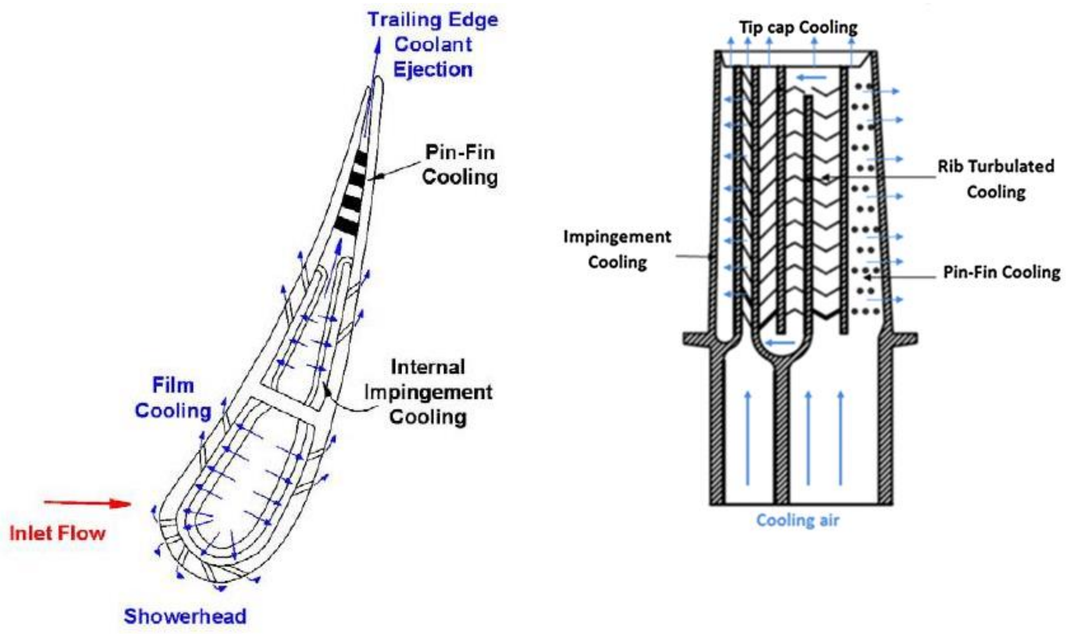

Figure 1-4: Schematic illustration of different cooling techniques

The film cooling technology was introduced in 1970s whereby the holes were drilled on the blade surface and bleed air passing through the convection passages was exhausted through the holes [4]. In today's engine, the first and second stages of the turbine use this technology in all regions in the blade.

Due to the larger thermal and mechanical stresses experienced by the blade, discrete holes are being used in the film cooling without using porous surface or slots which have weak structural integrity [4]. Slots are applicable in the region of trailing edge of the blade. When designing a blade film cooling system it is considerable that the cooling efficiency should be maximized with sufficient coolant mass flow rate. That mass flow rate should not be higher than a certain limit after which the drop of thermal efficiency of the engine would be greater than the increase achieved by the higher turbine inlet temperature [5]. Researchers and engineers have continuously tried to design more efficient film cooling holes such that the coolant jet attaches the blade external surface near the injection region and also far downstream [5]. In order to minimize aerodynamic losses and prevent the reduction of coolant concentration, these film cooling designs should be able to reduce turbulent mixing of two streams with different momentum (the hot gas flow and coolant flow) [5].

1.3 Film cooling analysis

The cost involved in manufacturing and repairing film cooling holes is significant. The total cost of manufacturing depends on the method used for making holes. Generally electro discharge machining (EDM) or laser drilling are used [4]. The cost of laser drilling is significantly lower than electro discharge machining (EDM). Electro discharge machining is flexible when considering hole shape and hole placement [4]. Therefore ability to predict the local temperature distribution on airfoil is important because of significant cost of manufacturing and the cost incurred in airfoil failure [4]. Therefore the models of local temperature distribution based on the relevant parameters from the flow physics are playing important role in the process of gas turbine blade cooling system design and analysis.

Surface heat flux without film cooling can be written using convective heat transfer coefficient, h_0

$$\boldsymbol{q_0 = h_0(T_{ref} - T_w)} \text{ ------------- } \mathbf{1\text{-}2}$$

Where, T_w is the wall temperature of the surface to be cooled. T_{ref} is free stream temperature, T_∞.

Heat flux with film cooling can be written using convective heat transfer coefficient, h_f [6],

$$\boldsymbol{q_f = h_f(T_{aw} - T_w)} \text{ ------------- } \mathbf{1\text{-}3}$$

When having film cooling, T_{ref} is replaced by the adiabatic wall temperature which is denoted by T_{aw}. The closest fluid temperature to the adiabatic surface is defined as adiabatic wall temperature. This is a good reference and $(T_{aw} - T_w)$ is the driving force to the heat transfer into the surface [6]. The adiabatic wall temperature is reduced by the coolant film layer formed on the surface. Then the heat flux into the surface is reduced since $(T_{aw} - T_w)$ is small. However, coolant jet-mainstream interaction may improve the heat transfer performance [7]. As a result, film cooling performance could be degraded. Therefore, cooling performance cannot be analyzed based only on the adiabatic wall temperature or heat transfer coefficient [7] [8]. Then, a new parameter of net heat flux reduction (NHFR) is defined for evaluation of the cooling performance. It takes into account the both the effects of increased heat transfer coefficient and decreased gas temperature by coolant film [7] [8] [4].

Net heat flux reduction, NHFR,

$$\boldsymbol{\Delta q_r = \frac{(q_0 - q_r)}{q_0} = 1 - \frac{h_f}{h_0}[(T_{aw} - T_w)/(T_\infty - T_w)]} \text{ ------------- } \mathbf{1\text{-}4}$$

$$\boldsymbol{\Delta q_r = 1 - \frac{h_f}{h_0}\left(1 - \frac{\eta}{\phi}\right)} \text{ ------------- } \mathbf{1\text{-}5}$$

Where, non-dimensional metal temperature, $\phi = (T_\infty - T_w)/(T_\infty - T_{c,internal})$; $T_{c,internal}$ is the temperature of the coolant flowing inside the internal cooling passages of the turbine airfoil. Temperature of the metal surface is defined as the metal temperature, which was not simulated in the present study. This parameter is usually taken as 0.6 for NHFR calculation and data analysis [8].

Non-dimensional adiabatic wall temperature, $\eta = (T_\infty - T_{aw})/(T_\infty - T_{c,exit})$. Literature characterizes the film cooling performance by using this non-dimensional number called *adiabatic film cooling effectiveness*. h_f/h_0 is usually called heat transfer augmentation which has shown small effect on the NHFR [7]. Therefore, the present investigation used the adiabatic film cooling effectiveness to analyze cooling performance for 7-7-7 shaped hole with trench geometry. In this thesis, film cooling effectiveness or cooling effectiveness simply refers to adiabatic film cooling effectiveness defined by the aforementioned expression.

Blowing ratio (M) and density ratio (DR) are main facets which affects the adiabatic film cooling effectiveness variation. They are defined as, $M = \rho_c U_c/\rho_g U_g$ which refers to the quotient of the division of the mass flux of coolant to the mass flux of mainstream. $DR = \rho_c/\rho_g$, which refers to the quotient of the division of the coolant density to the mainstream density. In the present study, density ratio and free-stream turbulence intensity remain constant at 1.5 and 0.5% respectively and different blowing ratios were employed in different simulations.

1.4 Scope of the research

Various film hole shapes can be found in the literature with different cooling performance. Cylindrical hole shape is usually used in film cooling due to their easiness to manufacture. However with modern manufacturing facilities, the shaped holes such as expanded exit holes are used in film cooling to achieve higher cooling performance. In past studies, the cylindrical hole with shallow transverse slots (or called shallow trench) have been studied experimentally and numerically. Those research have shown that having shallow trench at the hole exit improves the cooling performance. These trenches can be manufactured easily when applying coatings on turbine blades. On the other hand, 2D transverse slots made on the surface shows superior cooling performance compared to 3D discrete hole rows. However, the 2D transverse slot cannot be used in gas turbine blades due to the loss of structural integrity. Therefore researchers are interested in finding discrete hole shapes which behaves like 2D transverse slots, to obtain superior cooling performance. As a result, the shaped holes with expanded exits have been developed and shown superior performance compared to the cylindrical holes. Due to the lack of literature for the shallow trench in expanded exit hole, it is interested in studying the cooling effectiveness for expanded exit hole with a trench. This study was totally based on numerical simulation while some experimental results from the literature were used to validate the model.

1.5 Aim and Objectives

Aim

To analyze the adiabatic film cooling effectiveness of gas turbine blades using shaped holes with trench geometry

Objectives

- To evaluate the predictions of RANS turbulence models for film cooling of shaped holes
- To investigate the effect of trench geometry of shaped holes on adiabatic film cooling effectiveness
- To investigate the effect of trench geometry of shaped holes on flow field

1.6 Outline of the thesis

The thesis has discussed the effect of geometry modification made at the hole exit on the cooling performance. A trench at the hole exit (or called transverse continuous slot) was made and performed numerical simulation using Realizable k-ε model with enhanced wall treatments as implemented in Ansys Fluent solver. The predicted results for different geometries of the trench have then been discussed qualitatively and identified general behavior and trends of film cooling effectiveness and flow field. ***Chapter 1*** gives an introduction to the film cooling, its performance analysis and the present study. In ***Chapter 2***, literature review, has focused on the past studies on shaped film holes and their cooling performance. ***Chapter 3***, methodology, has discussed about setting up the experimental cases in Ansys Fluent for validation. It moreover appears geometry of the computational space and which boundary conditions are set to the computational space. ***Chapter 4***, results and discussion, has devoted to discuss the validation of the model, illustrate the predicted results of modified geometry, and discuss the cooling performance and flow field to identify the general behavior and trends. ***Chapter 5*** has closed the thesis by presenting key conclusions and findings drawn from the results and discussion.

2 LITERATURE REVIEW

From the literature, round or cylindrical film holes have been the standard shape in film cooling due to easiness in manufacturing. Cylindrical film cooling holes have been investigated experimentally and numerically at a greater level. Coolant jet ejected from round cooling holes are lifted off and penetrated into main stream at larger blowing ratios (M > 0.5) which dramatically affects the cooling performances [5, 4, 9]. The mainstream has the possibility to cover the immediate downstream of hole exit with larger blowing ratios. Moreover, the cooling performance degrades as a result of lower lateral spreading. At higher blowing ratios, the expanded exit holes have shown better performance than the round holes since it has shown the diffusion of the coolant and less insertion of coolant into mainstream. Shaped holes have laterally and forward expansion at the hole exit and it shows significant improvement of cooling performance with well-spread coolant over the surface. In addition, the adiabatic effectiveness of shaped holes shows a less sensitivity to blowing ratios and shows remarkable cooling performance compared to cylindrical holes [4]. The expansions at the hole exit are made to achieve similar behavior like 2D transverse slots which shows the ideal film cooling performance with uniformly distributed cooling supply [10] [11]. Meanwhile, a shallow trench can also be made at the hole exit to achieve the 2D slot-like behavior [12].

2.1 Cooling performance of shaped Holes

Typical shaped hole designs and cylindrical hole designs are shown in Figure 2-1. Laidback, fan-shaped, laidback fan-shaped and conical holes are the basic shaped holes classified in the literature [13]. The laidaback hole have expansion into surface at the injection while fan-shaped hole are expanded in lateral direction. Expansions in both directions are found in laidback fan-shaped holes, which can be considered as a combination of laidback hole and fan-shaped hole [13]. Equal amount in the expansions occurs in each direction around its centerline while the area of conical hole increases from inlet to exit [13]. Convergent slot hole (CONSOLE) has a transition from cylindrical shape to a continuous slot at the exit [13]. There is a transformation from the cylindrical hole to the slot. Coolant accelerates when passing through CONSOLE hole since the area from entrance to exit decreases [13].

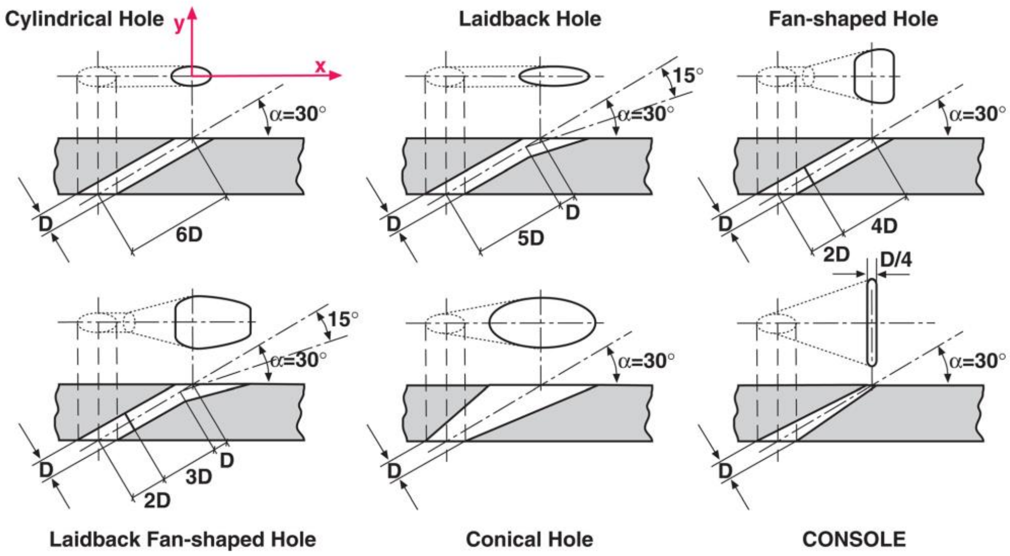

Figure 2-1: Basic hole designs [13]

Two dimensional external flow occurs in two dimensional film cooling. On the other hand, the coolant flow injects to the main stream uniformly through continuous slot across the span [6]. Typical designs of two-dimensional uniform injections are shown in Figure 2-2, which for instance are used in combustion chambers, afterburner nozzles and rockets [6] [14]. A uniform film layer over the surface is created by the continuous slot injection and it shows superior film cooling performance than the three dimensional discrete holes across the span, which have been used in gas turbine blade cooling [6] [10].

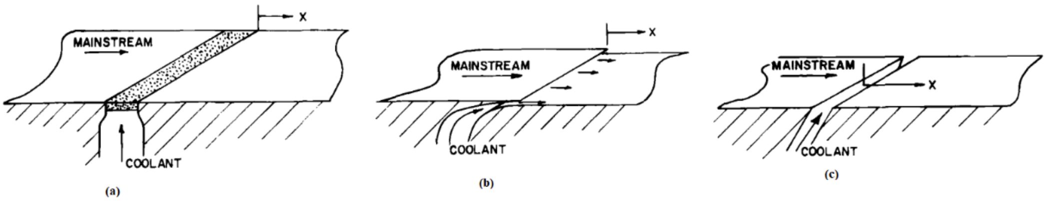

Figure 2-2: Two-dimensional film cooling geometries (a) porous slot (b) tangential injection (c) slot angled to mainstream [6]

The injection geometry affects in second order in two-dimensional film cooling compared to the three-dimensional film cooling which have discrete film holes across the span [6]. In spite of that, continuous injection slots can't usually be used because of structural integrity and life of the part [4] [6] [15]. Therefore discrete film holes, even rows of multiple cooling holes, have been used in three-dimensional film cooling [6]. Many research have been conducted for cylindrical holes to reveal the flow structures and cooling performance based on the parameters affected significantly to the flow and thermal characteristics [16]. The cooling effectiveness has been found to be considerably different compared to continuous slot [14]. Moving from cylindrical film hole to shaped film holes occurs first for high performance gas turbine engines used in military applications and gas turbines with extremely high turbine inlet temperature [10] [17]. Then it dramatically moves to the commercial gas turbine engines [10]. These shaped holes shows slot-like performance because expansion occurs at the hole exit [10]. The hole exit area can be increased in the injection plane using shaped holes [10]. Jet diffusion of shaped holes at the injection lower the blowing ratio and aerodynamic mixing losses. Substantial coolant coverage in lateral direction can also be observed. This helps to enhance cooling effectiveness and turbine efficiency [10] [18]. Shaped holes decrease the blowing ratio at the hole exit thereby lessening the penetration of coolant jet into the mainstream [18] [19]. Consequently, the improved spreading of the coolant in lateral direction increases effectiveness of the coolant film [18] [19].

Many researchers have identified key features in film cooling flow in many years of research. The cooling behavior of diffuser holes and cylindrical holes is vital to understand. At low and high blowing ratios, some essential contrasts between cylindrical and fan-shaped holes can be seen in Figure 2-3 [20]. At low blowing rate, the highest effectiveness of cylindrical hole has been shown along the center line while the film cooling effectiveness variation of fan-shaped holes have resulted in two maximums in lateral direction [20]. At high blowing rate, cylindrical holes have shown the jet lift-off and then the jet reattaches the surface at the distance downstream around four diameters while the fan-shape hole exhibits higher film cooling effectiveness with good lateral spreading [20]. Due to this jet lift-off of cylindrical holes, coolant is mixing well with hot gas leaving pronounced depletion of cooling effectiveness [20, 21]. At higher blowing ratios, shaped holes improve the film cooling effectiveness while it generally shows better lateral spreading [20] [21] [22].

The fan-shaped holes have not shown the jet lift-off in the elevated blowing ratios and the coolant and hot gas have mixed poorly. Cooling effectiveness and lateral spreading have been improved by fan-shaped holes at higher blowing rates [20]. The improved spreading of coolant in lateral direction is a result of hole exit’s expansion in lateral sides [20]. A high cooling effectiveness occurs in an extended area over a longer surface distance.

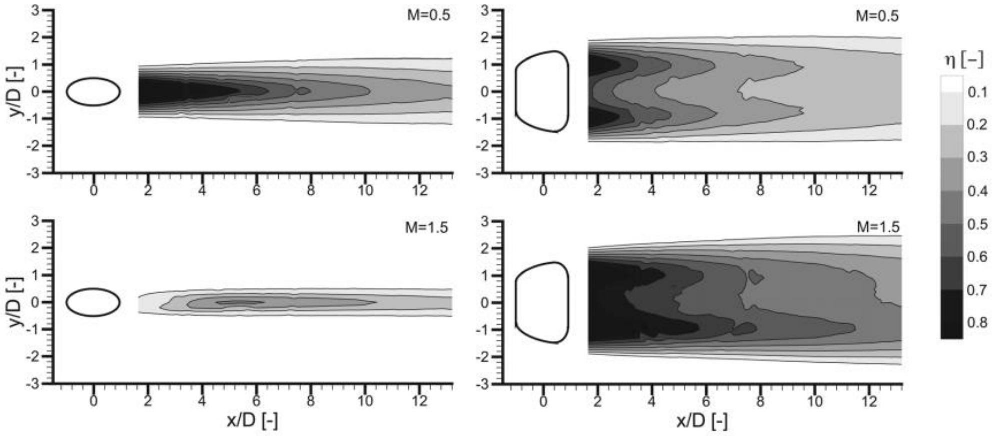

Figure 2-3: Local film cooling effectiveness of cylindrical and fan-shaped holes at low and high blowing rates [20]

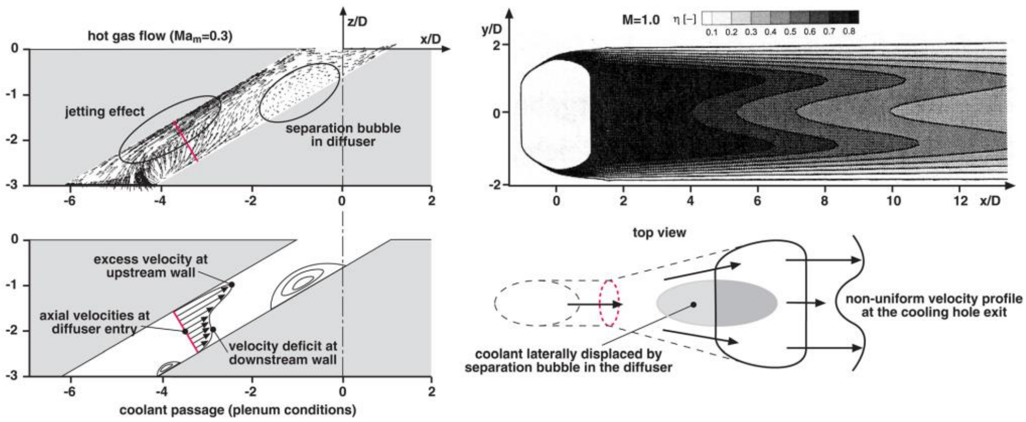

Figure 2-4: Schematic representation of flow phenomena typically seen in shaped holes [20]

The fan-shaped hole has shown the separation region developed on the leeward side wall of the diffuser part as depicted by Figure 2-4. The velocity profile is non-symmetric at the diffuser inlet, since the coolant is moving towards the hole's centerline. Very low velocities caused due to the non-symmetric velocity profile in downstream part of the hole while the upstream part carries very high velocities of the coolant [20]. This is known as the jetting effect. An adverse pressure gradient occurred within the diffuser tends to separate the coolant flow [20]. The coolant displaced sideways by the separation region makes the usual bimodal effectiveness pattern [13] [20] [23]. Thus, the separation region supports for the lateral spreading of coolant as well as to enhance film cooling effectiveness [20].

As illustrated in Figure 2-5, a significant difference for cooling effectiveness and heat transfer coefficients was observed for cylindrical and fan-shaped hole in low and high blowing ratios [20]. No notable difference of film cooling effectiveness was observed when moving along the downstream direction [20]. The fan-shaped hole has not shown superior cooling performance with low blowing ratio [20]. It has exhibited a noticeable improvement of film cooling effectiveness with high blowing ratio [20].

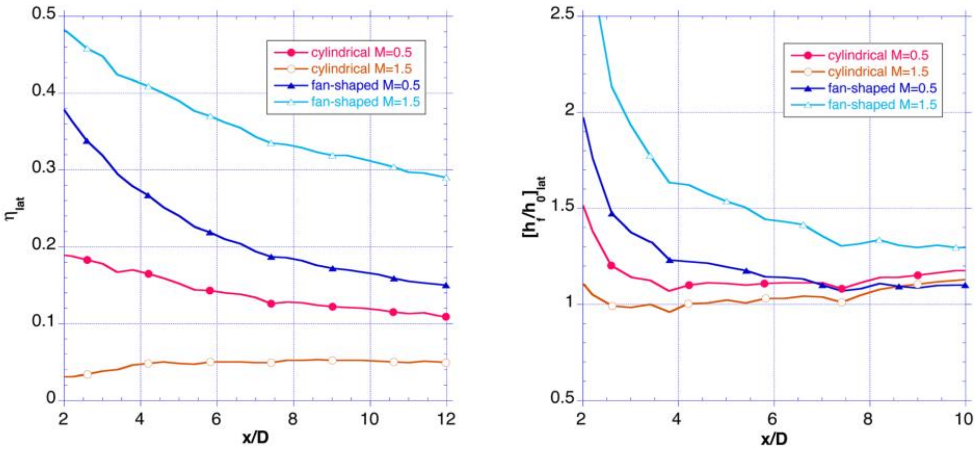

Figure 2-5: Laterally averaged film cooling effectiveness (left) and related heat transfer coefficients (right) [20]

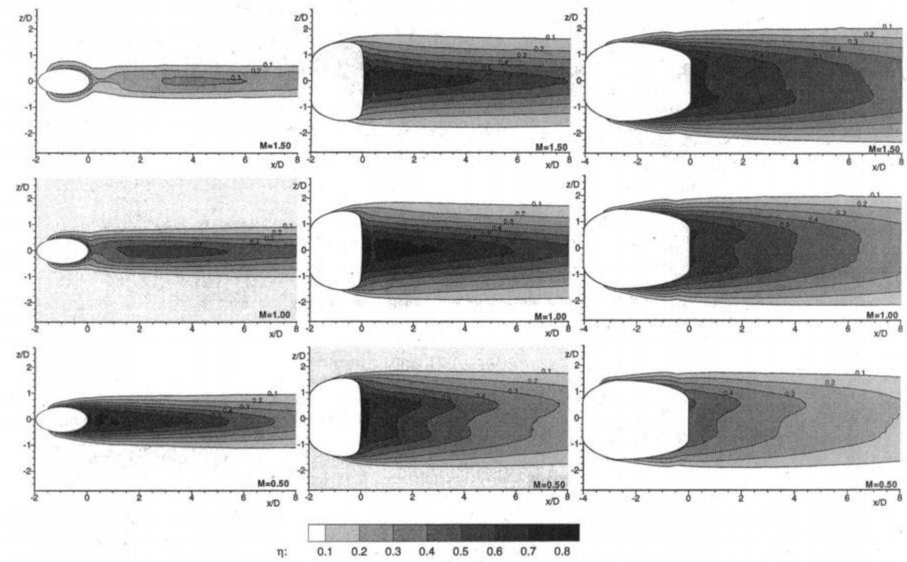

Figure 2-6: Local film cooling effectiveness for the cylindrical, fan-shaped, and laid-back fan-shaped hole [21]

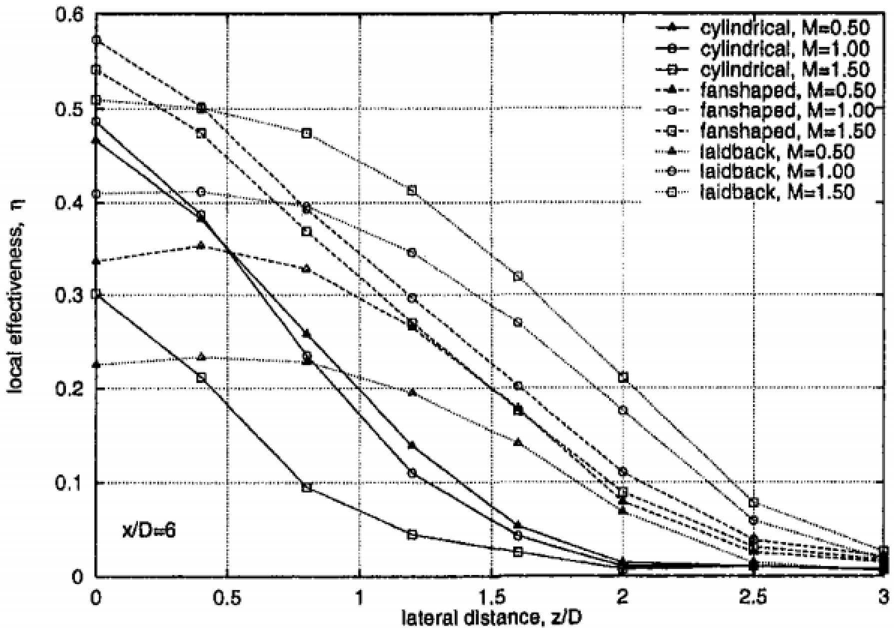

Figure 2-7: Local lateral effectiveness, η for the three holes [21]

Figure 2-6 presents experimental results of two-dimensional film cooling effectiveness of cylindrical, fan-shaped and laidback fan-shaped holes [21]. These distributions were taken by IR camera at various blowing ratios such as 0.5, 1.0 and 1.5 and hot gas Mach number of 0.6. It has shown comparison among the aforementioned hole shapes. Laidback fan-shaped holes have shown higher lateral spreading compared to the fan-shaped hole (Figure 2-6) [21]. Figure 2-7 shows local lateral effectiveness for cylindrical hole, fan-shaped hole and laidback fan-shaped hole at mainstream Mach number of 0.6. For high blowing rates, laidback fan-shaped holes have maintained higher lateral spreading while the lateral spreading of fan-shaped holes is limited [21].

At low blowing ratio, laterally averaged film cooling effectiveness has been lesser in laidback fan-shaped holes than fan-shaped holes since the laidback portion contributes to mix the coolant and the hot gas (Figure 2-8) [21]. As exhibited in Figure 2-8, the variation of laterally averaged film cooling effectiveness has been illustrated for cylindrical, fan-shaped and laidback fan-shaped holes at mainstream Mach number of 0.6.

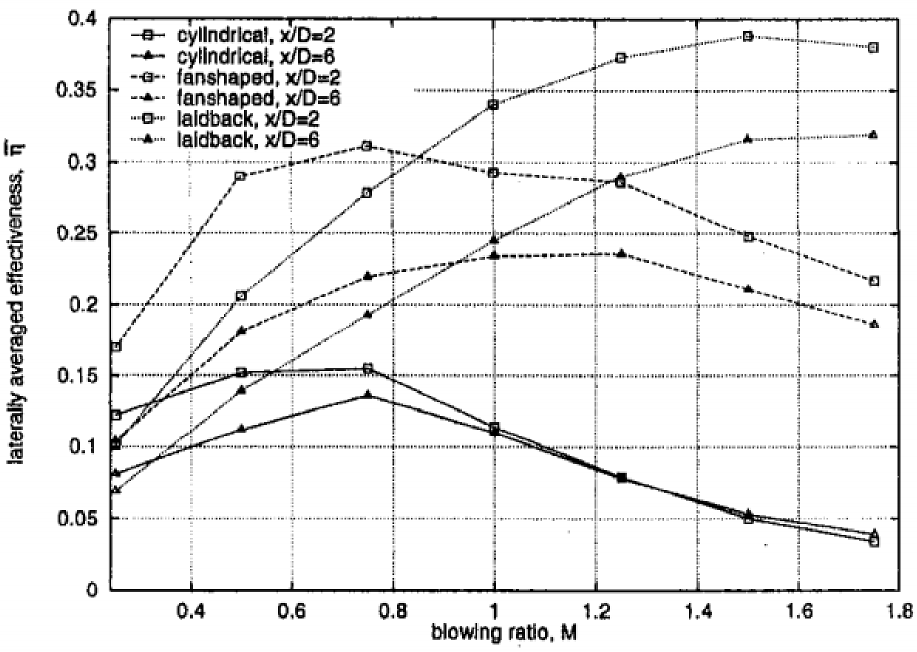

Figure 2-8: Effect of blowing ratio (M) on laterally averaged effectiveness $\overline{\eta}$ for the three holes [21]

The most research work has compared their results of new cooling holes with cylindrical holes considering it as baseline. The cylindrical holes show well-known jet detachment at higher blowing ratios [24]. A baseline shaped hole without jet detachment has been developed to be used for comparison purposes of new cooling hoel designs [24]. This hole has been developed with both of forward and lateral expansions in the diffuser section hiding the bimodal distribution of the lateral effectiveness pattern [24]. The bimodal distribution that can be seen commonly in shaped holes with higher expansion angles can be hidden by reducing expansion angle of the diffuser section [13]. Therefore the baseline shaped hole with 7^0 expansion angles in the both directions, lateral and stream-wise, has not shown a bimodal cooling effectiveness pattern. This baseline shaped hole with modifications at the hole exit was used in this study.

The experimental cooling effectiveness pattern of the baseline shaped hole are shown in Figure 2-9. The higher blowing ratio has shown narrower cooling pattern than that of low blowing ratio. Cooling patterns at low blowing ratio merges at the mid-pitch in the downstream while higher blowing ratio shows the narrow pattern which the coolant jet poorly contact with the surface [25].

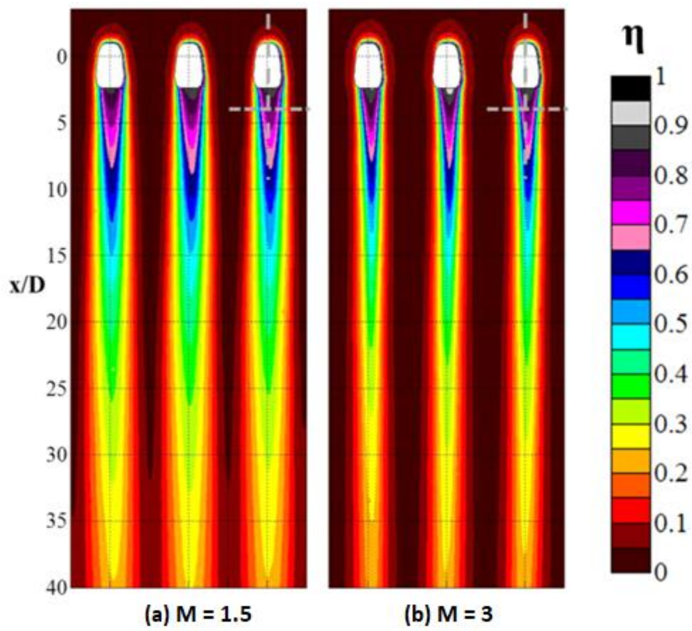

Figure 2-9: Adiabatic effectiveness contours at DR = 1.5 and turbulence intensity of 0.5% [25]

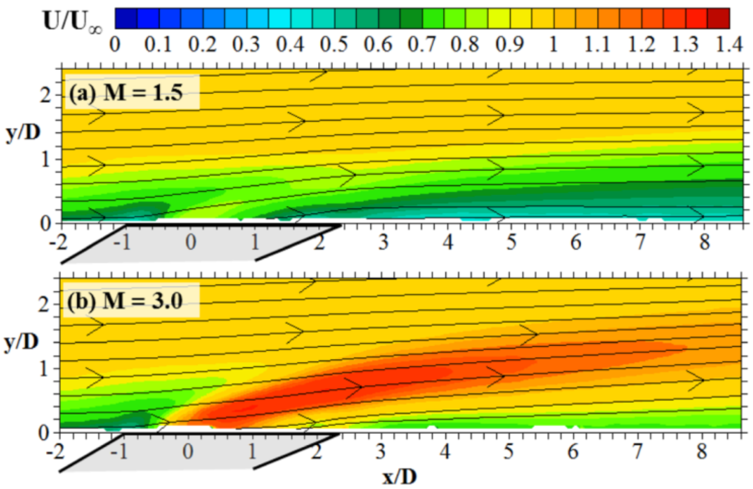

Figure 2-10: Contours of time-mean stream-wise velocity and streamline on centerline plane for DR = 1.5, Tu = 0.5% [25]

The jet penetration into the mainstream makes effectiveness pattern narrow at higher blowing ratios. The stream-wise velocity contours at M = 1.5 and 3 as shown in Figure 2-10 provides how the penetration occurs [25]. When having coolant jet with low momentum, mainstream ingestion explains why the centerline effectiveness is lower. Thole et al. [26] have observed the mainstream ingestion of low momentum coolant jet for laidback fan-shaped holes. Higher blowing ratios produced higher momentum coolant jet thereby resisting mainstream ingestion. The ingestion of mainstream into the coolant jet can be used to explain the sharp decay in laterally averaged effectiveness at low blowing ratios as shown in Figure 2-11, and Figure 2-12 [24].

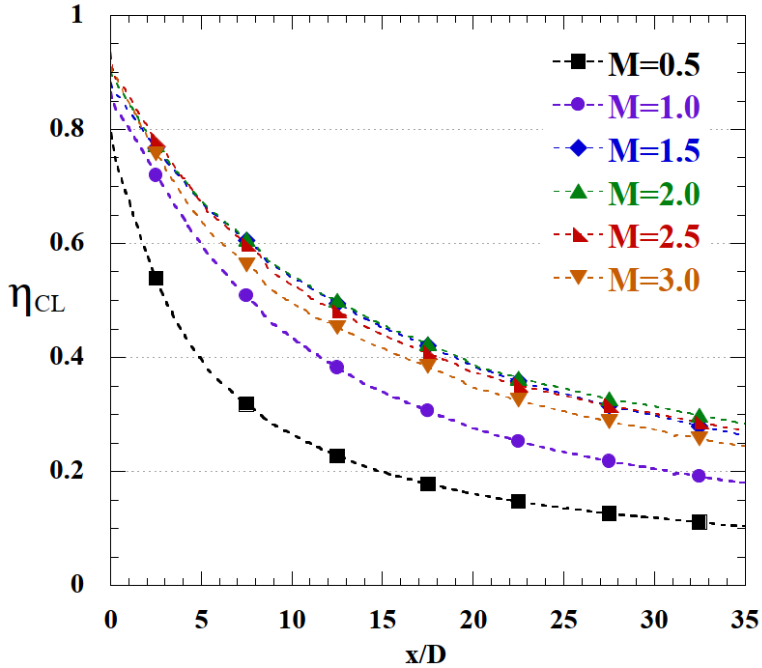

Figure 2-11: 7-7-7 shaped hole centerline effectiveness at DR = 1.5 and free stream turbulence of 0.5% [24]

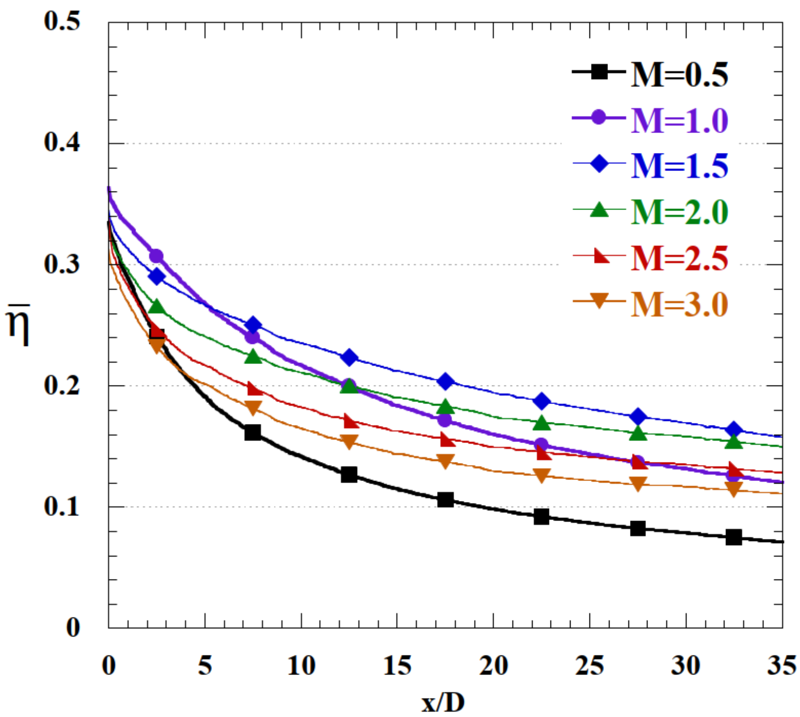

Figure 2-12: 7-7-7 shaped hole laterally averaged effectiveness at DR = 1.5 and free stream turbulence of 0.5% [24]

2.2 Flow field with shaped hole

Flow phenomena inside film hole and external jet-cross flow interaction has been studied in the literature and identified that the in-hole CRVP and the external CRVP are the main flow structures in film cooling, which significantly affect the film cooling effectiveness [27].

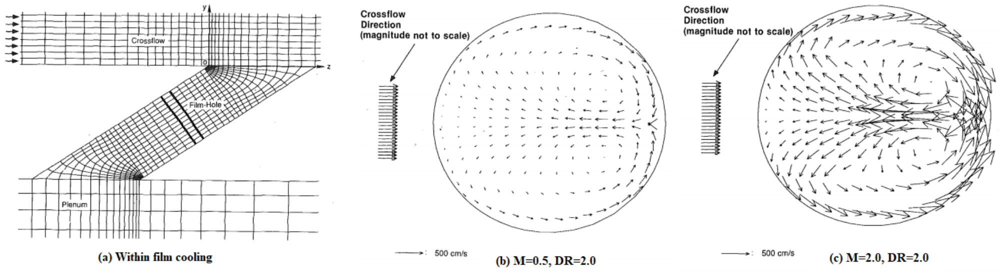

Figure 2-13: Counter rotating vortex pair within cylindrical film hole [27]

Navier-Stokes equations have computed CRVP generated inside cylindrical hole as shown in Figure 2-13 [27]. A plane perpendicular to the general flow direction inside the hole has been chosen to present these secondary flows and the location of this plane is shown as two bold lines in Figure 2-13 (a). With blowing ratio, it was observed that the strength of these secondary flows (or CRVP) increases [27]. The secondary flow in the coolant flow direction generates the in-hole CRVP as the coolant from the plenum turns at the entrance of the inclined tube [27]. Many researchers have been tried to identify the mechanism to generate the in-hole CRVP and external CRVP.

The vorticity in the in-hole boundary layer has been identified as the creator of the CRVP [28]. According to this assumption, the comparison of several hole shapes have presented that the X-component of the in-hole vorticity generates CRVP, which X is in the mainstream flow direction [29]. According to their explanation, the forward-diffused holes should perform well compared to the laterally-diffused holes. CRVP was captured by RKE-based DES model while the vorticity in the jet boundary layer has been regarded as the main source for CRVP generation [30].

The in-hole boundary layer has been presented as the cause of CRVP formation [31]. In addition, the in-hole flow separation at the entrance of hole affects the CRVP formation. Yuan et al. [32] have presented that the formation of the CRVP is led by the mechanism named hanging vortex. Shear layer have been identified as the main factors for CRVP formation [33]. Jet and cross-flow interaction and the in-hole vorticity contribute to create the shear layer.

Figure 2-14 presents four basic flow structures in the jet-cross flow interaction related to cylindrical jet. Horseshoe vortex is one of the major flow structures, which wraps around the base of the jet issuing from cylindrical hole [34]. Approaching boundary layer experience an adverse pressure gradient from the cylindrical jet and thus separating the flow [34]. This flow separation is responsible to generate the horseshoe vortex. Jet shear-layer vortices occur due to Kelving-Helmholtz instability acting on the annular shear layer of the issuing jet [34]. The CRVP dominant in the far field were identified to generate by impulsion of the jet to cross flow [34, 35]. As shown in Figure 2-14, immediate downstream of the hole is the region where wake vortices generates between the wall and the jet [34].

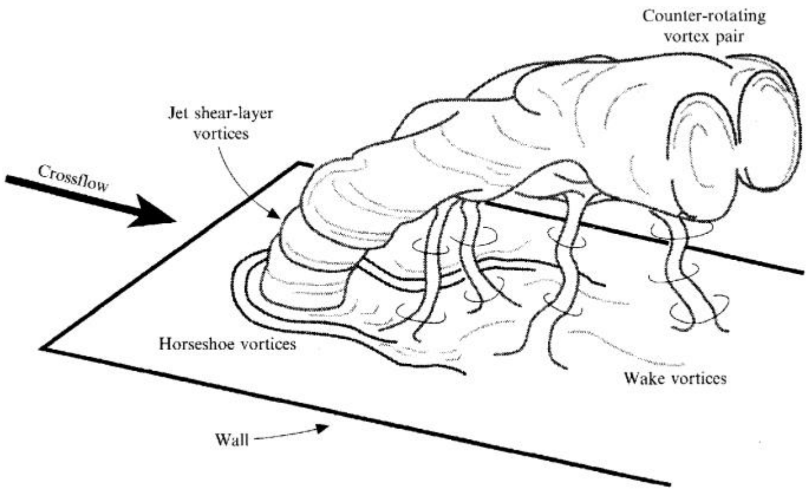

Figure 2-14: Basic flow structure in jet-cross flow interaction for cylindrical hole [34]

Even this wake vortices have somewhat similar characteristics to the wake generated behind a cylinder, there is significant differences in terms of the wake formation [34]. The two ends of wake vortices terminate at the jet and on the wall and span of these vortices enlarge continually in the downstream [34]. Based on unsteady simulations, CRVP and the ring-like vortex (RLV) have been regarded to be generated by the shear layer [36]. The formation of the RLV was recognized as a result of rolling up of shear layer. Then the CRVP formation is by elongating RLV axially on lee side of the coolant jet [36].

The wall boundary layer effects on formation of CRVP does not initiate the CRVP but it strengthens the CRVP [37]. However, its effects on jet flow field is in low level consideration. There are two cases that have been numerically simulated with different boundary layer thicknesses (δ) at the jet injection. Case (I) has zero boundary layer thickness while case (II) has 0.5 boundary layer thickness [37]. Figure 2-15 and Figure 2-16 shows the formation of CRVP under the two different boundary layer thicknesses and its influence to the strength of CRVP.

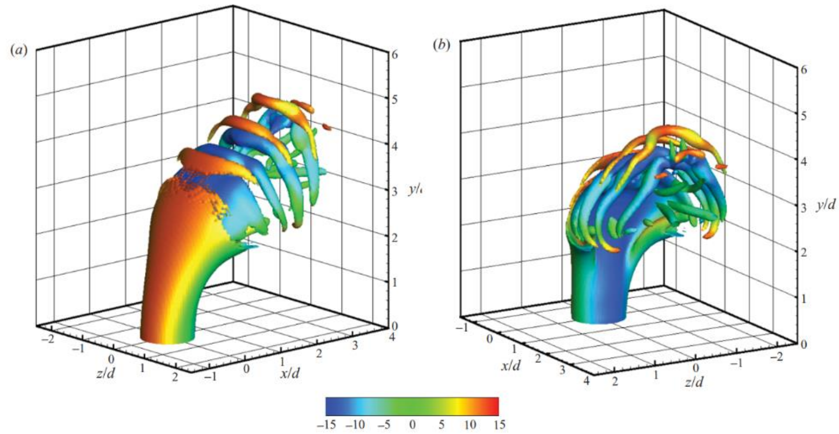

Figure 2-15: Vorticity magnitude ω_z of the jet (a) windward side (b) lee side (Case I) [37]

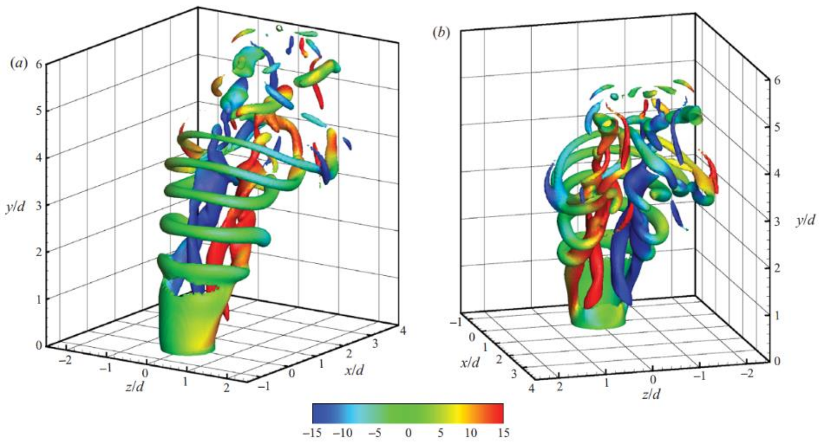

Figure 2-16: Vorticity magnitude ω_z of the jet (a) windward side (b) lee side (Case II) [37]

A specific vortex structure can be seen with some shaped holes compared to cylindrical holes. Anti-kidney vortex pair (or called negative vortex pair) whose direction of rotation is opposite to CRVP is generated and it reduces the negative effect of CRVP on film cooling effectiveness [38]. Film cooling effectiveness is degraded since the CRVP with jet-liftoff draws the hot mainstream under the coolant jet as shown in Figure 2-17 [38]. The anti-kidney vortices which improves the coolant lateral spreading minimized the degradation of cooling effectiveness and it is reducing jet lift-off as shown in Figure 2-18 [38]. Formation mechanism of anti-kidney vortices in shaped holes has been explained by Heven et al. [38]

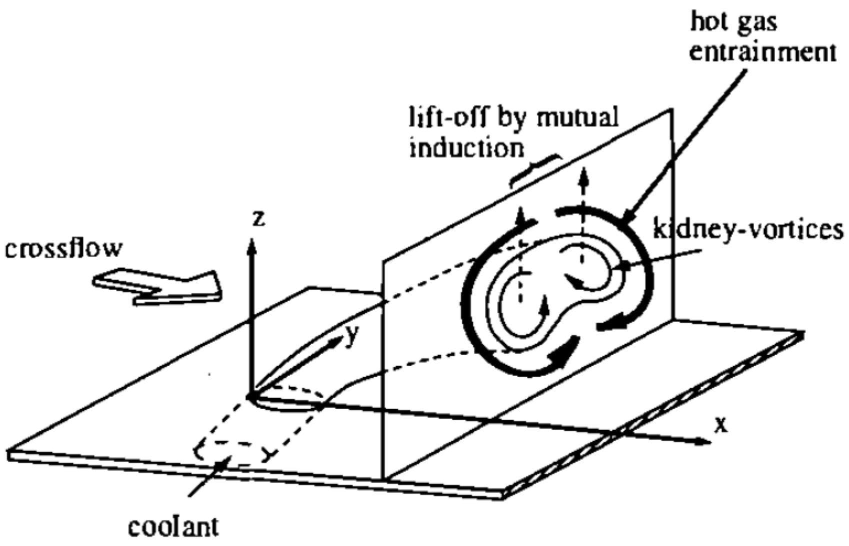

Figure 2-17: Counter rotating vortex pair (or kidney vortices) [38]

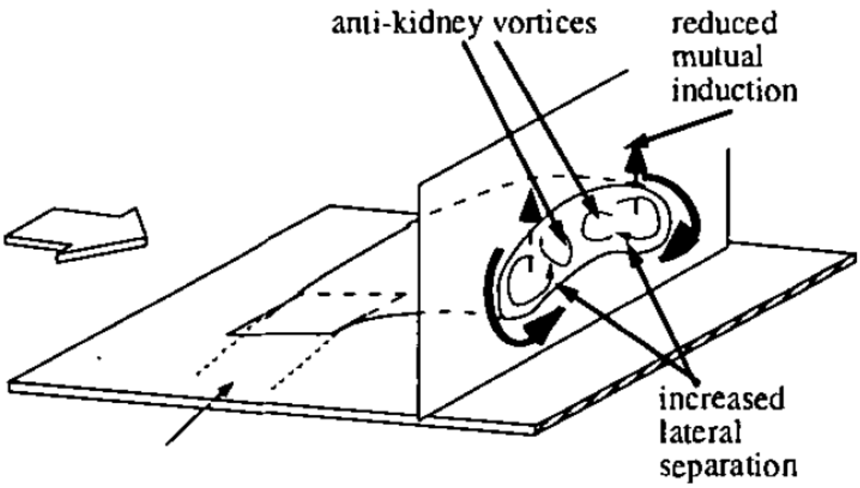

Figure 2-18: Anti-kidney vortices [38]

The formation of the kidney and anti-kidney vortices have been explained by using double deck structure [38]. The double deck structure consists of lower deck and upper deck vortical structures as shown in Figure 2-19 and Figure 2-20. The lower deck is steady since its vortical flow structures are always present while the upper deck structures are present intermittently. For rectangle hole with low aspect ratio, upper deck structure is in the sense of rotation similar to kidney vortices as shown in Figure 2-19. For rectangle hole with high aspect ratio, the upper deck vortical structure which is in opposite direction to the kidney vortices was demonstrated as anti-kidney vortices as shown in Figure 2-20. The lower deck is formed by the side wall vorticities of the rectangle exit while the leading edge vorticity is responsible to form the upper deck.

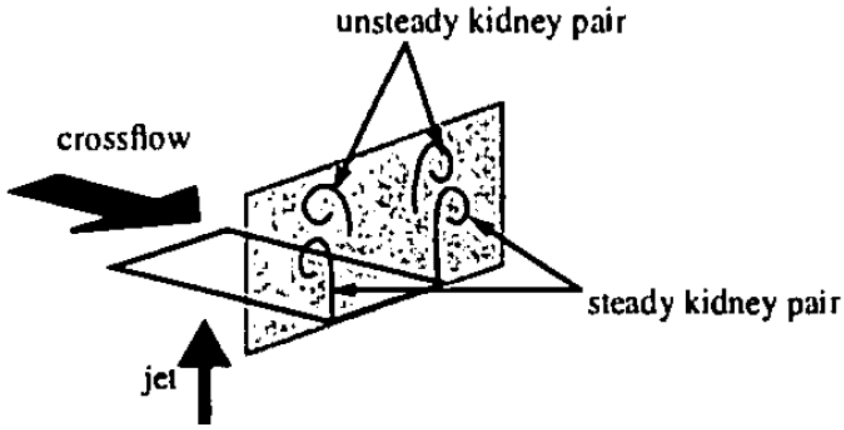

Figure 2-19: Double deck structure for low aspect ratio [38]

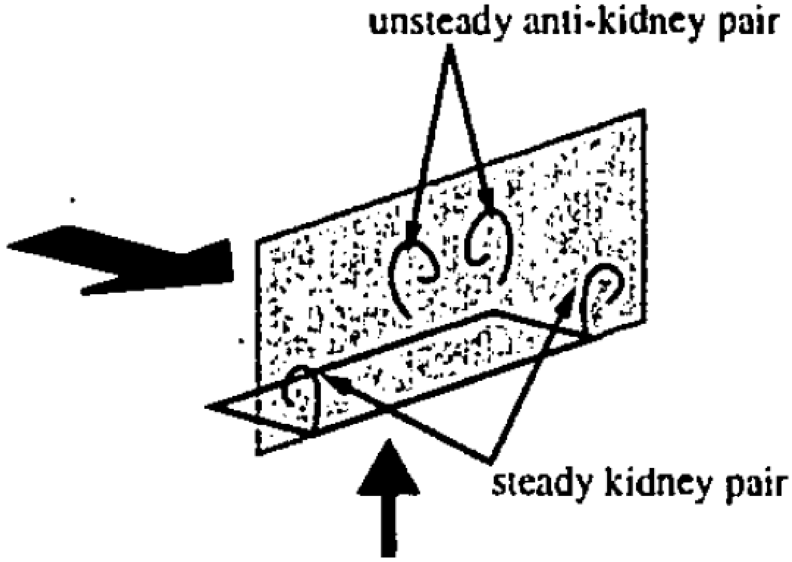

Figure 2-20: Double deck structure for high aspect ratio [38]

The CRVP of "7-7-7 shaped hole" generates at the immediate downstream of the hole trailing edge. The strength of it has weaken when decreasing the blowing ratio as shown in Figure 2-21 [25]. This hole with 7^0 expansion angle in lateral and forward direction has not shown anti-kidney vortices. Due to this low expansion angle in the lateral direction, separation region (or lower momentum region) in the downstream of the hole gets smeller [13]. Since smaller expansion angles reduce the spatial extension of the separation region, movement of the coolant towards side walls in the diffuser section is not significant [13]. As a result, the bimodal pattern cannot be seen in diffuser holes with lower expansion angles as shown in Figure 2-22 which shows contour plots from experimental results and it disappears when reducing the expansion angle of shaped holes [13].

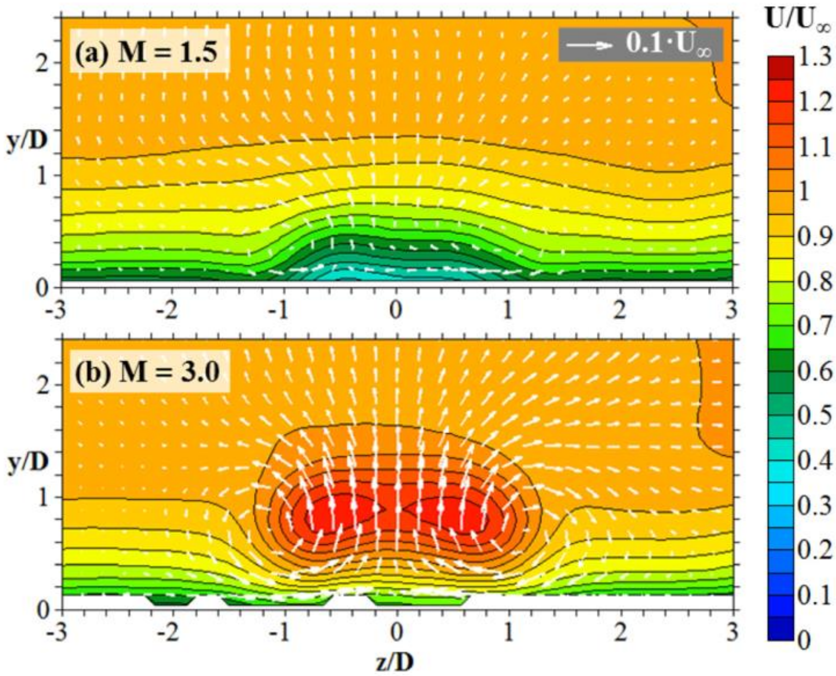

Figure 2-21: Contours of mean stream-wise velocity in the x/D = 4 cross-plane for DR = 1.5 and free stream turbulence of 0.5% [25]

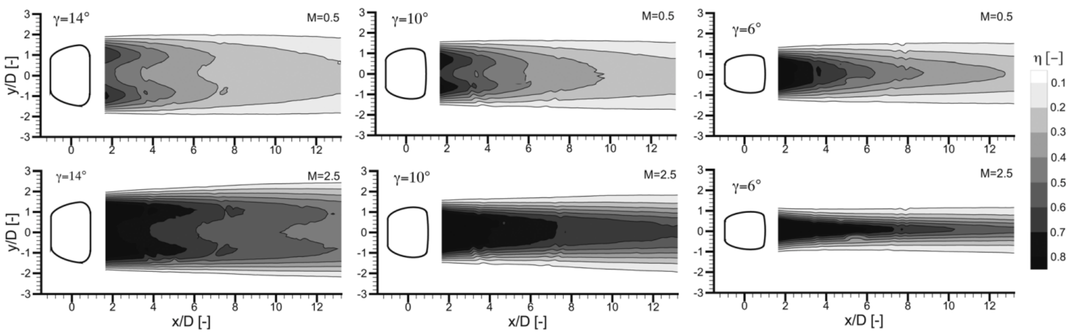

Figure 2-22: Local effectiveness variation with expansion angles at different blowing ratios [13]

The cylindrical holes formed in a shallow surface trench provides improved cooling performance over the usual cylindrical holes [12]. The geometry configuration is shown in Figure 2-23. This new design can be applied to existing film holes through the application of surface coating [12]. Significant improvement to the cooling performance has shown in the near region of hole exit [12]. The effectiveness of the geometry shows little or no sensitivity to blowing ratio over 1 to 4. This indicates that low coolant flow rates can be used to achieve same effectiveness at higher blowing ratios, which has a potential to save coolant [12].

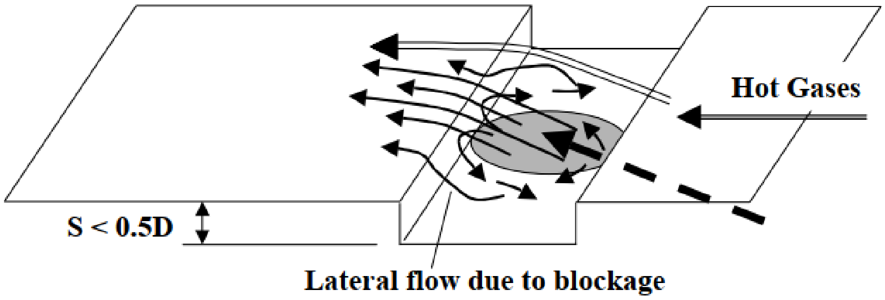

Figure 2-23: Cylindrical film hole in a trench [12]

At blowing ratios of 0.5 and 1, LES for a trenched cylindrical hole have been carried out to study the flow field and cooling performance [11]. Anti-kidney vortices can be seen in the trenched hole as shown in Figure 2-24. Spatial size of the CRVP is larger in trenched hole than that of round hole without a trench. As shown in Figure 2-25, M = 1 case provides greater extension in streamwsie direction compared to that of M = 0.5 case. Higher coolant accumulation was observed in the trench when increasing the blowing ratio as shown in black dotted line in Figure 2-25 [11].

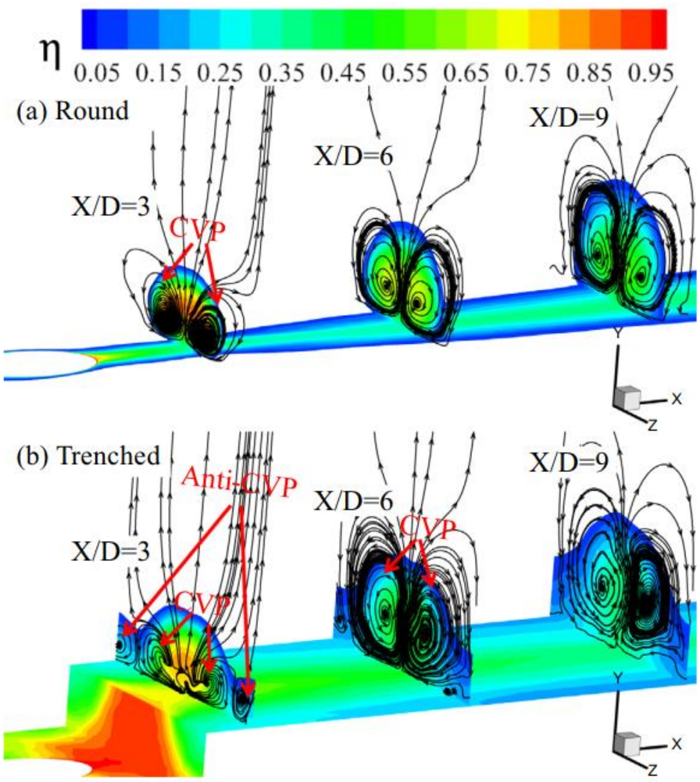

Figure 2-24: Effectiveness and streamlines on the selected planes at M = 1.0 [11]

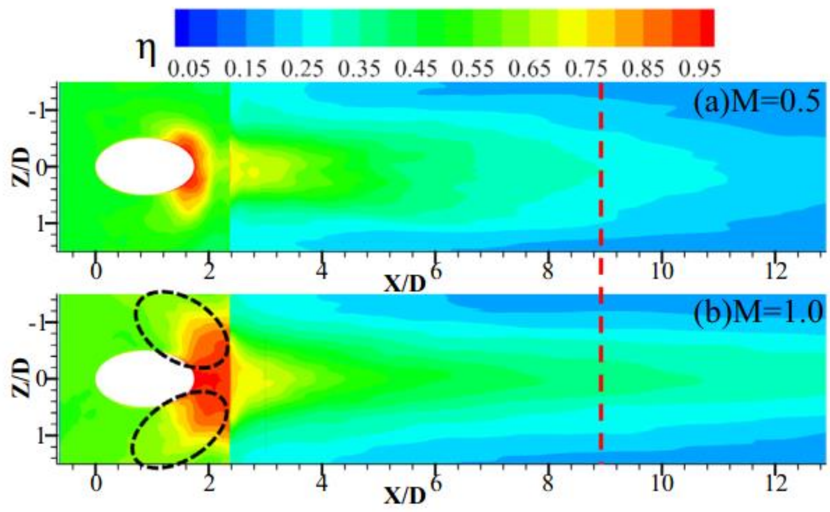

Figure 2-25: Time-averaged effectiveness for trenched holes at M = 0.5 and M = 1.0 [11]

2.3 Numerical studies – RANS simulations

Numerical studies have been performed on fluid flow and heat transfer to optimize the film cooling design in gas turbine engines [28, 30, 39]. The computational cost of the turbulence models in Reynolds Average Navier-Stokes equation is lower than LES. As a result, aforementioned studies of hot jet in cross flow have been studied using this method [40] [41]. LES has been used to study the physical aspects of flow and cooling performance in an average extent. However according to the literature, LES reveals more details in the flow physics and cooling performance although it takes much computational power and consumes more time.

Heat transfer of a new cooling scheme with the comparison of existing experimental results has been studied by using numerical analysis [42]. As shown in Figure 2-26, the cooling scheme proposed in the study was a shaped hole which is comparable to exiting studied shaped holes. The research has shown that CFD can be successfully used in predictions of film cooling performance as long as used in a careful manner [42]. The similar results were observed when using standard wall functions, non-equilibrium wall functions, and two-layer zonal or enhanced wall treatment show if fine enough mesh is achieved near wall [42]. The results are compatible with the physics while two-layer zonal model performed well [42]. Two-layer zonal model or enhanced wall treatment does not meet success since all wall treatments depend on empirical mathematical relations [42].

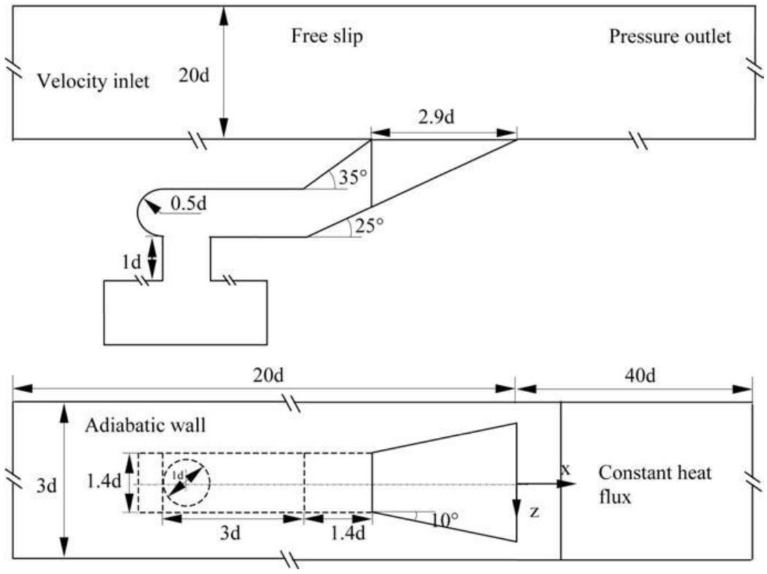

Figure 2-26: Computational domain and boundary conditions for the new scheme [42]

Three dimensional flow field of cylindrical hole has been studied using RANS with k-ε turbulence model [41]. For the blowing ratios of 0.8 and 1.0, the jet lift-off and reattachment were identified by experimental studies [41]. The phenomena has not been reproduced by the computational model with coarse grid in near wall region [41]. In this investigation, the near wall region immediate downstream of the injection were maintained at sufficient grid refinement and the lift-off and reattachment phenomena were able to capture by the numerical simulation [41]. However the wall functions has not predicted the near wall quantities accurately. For further improvements, two-layer or law-Re number turbulence model have been proposed instead of wall function [41]. The jet in cross flow is anisotropic inherently while k-e model is isotropic [41]. The research showed that the only sources of error for numerical solution are near wall treatments and turbulence modeling [41]. Another source of discrepancy is slight jet skewness observed at the experiment as shown in Figure 2-27 [41]. The centerline effectiveness are given based on geometric center line in experimental data while the actual jet centerline has slightly skewed from its geometric centerline [41]. Figure 2-28 shows close agreement of corrected jet centerline effectiveness with experimental data compared to uncorrected data [41]. The numerical results is adjusted with the skewness to be consistent to experiment.

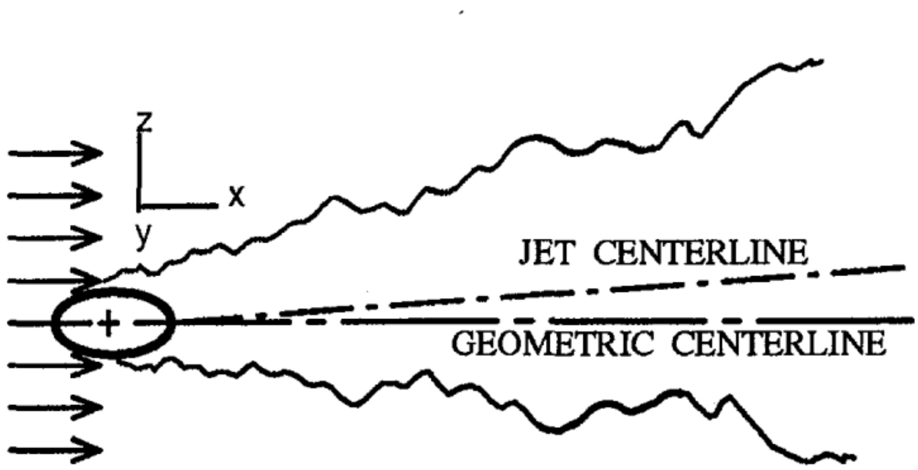

Figure 2-27: Jet skewness present in experimental test case [41]

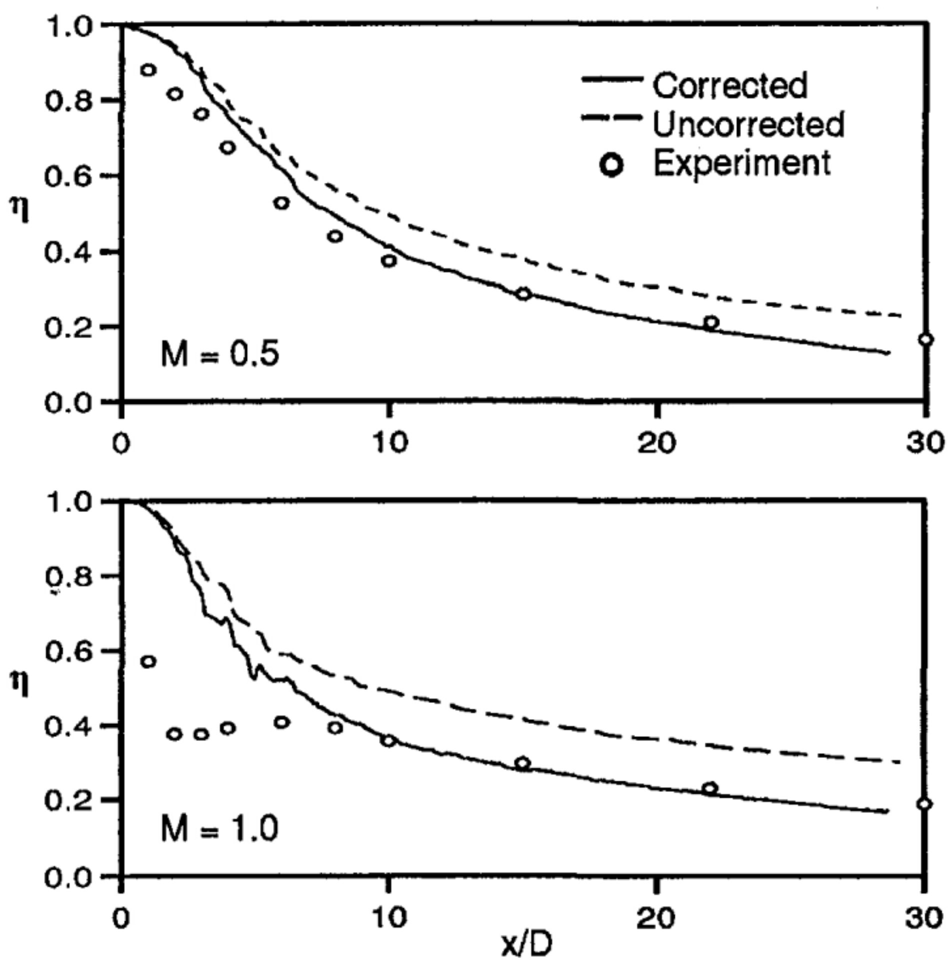

Figure 2-28: Centerline adiabatic effectiveness adjusted with skewness [41]

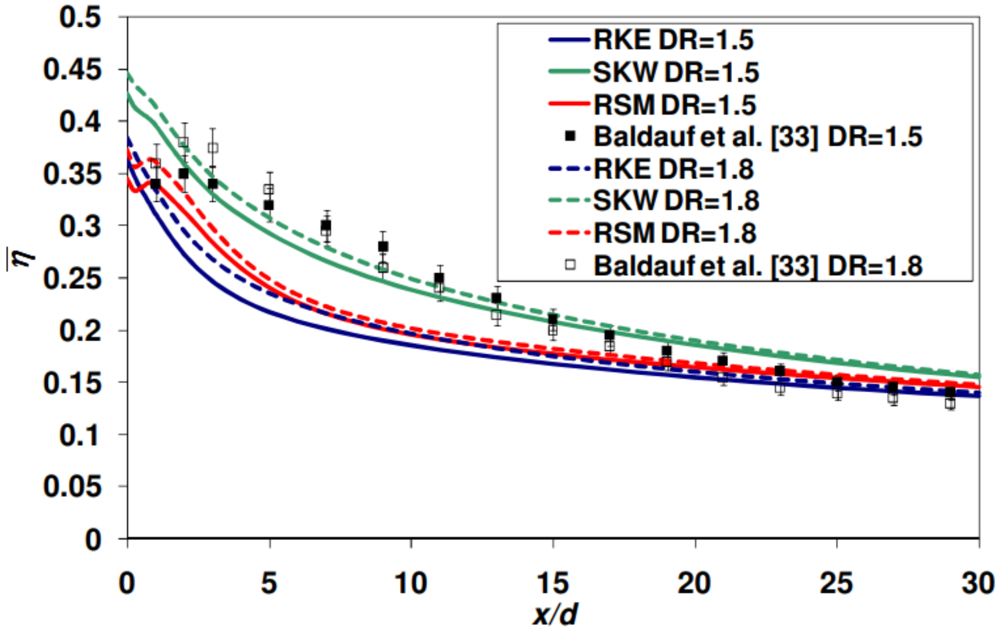

Figure 2-29: Laterally averaged effectiveness predicted by the turbulance models and experimental results for M=0.5 [40]

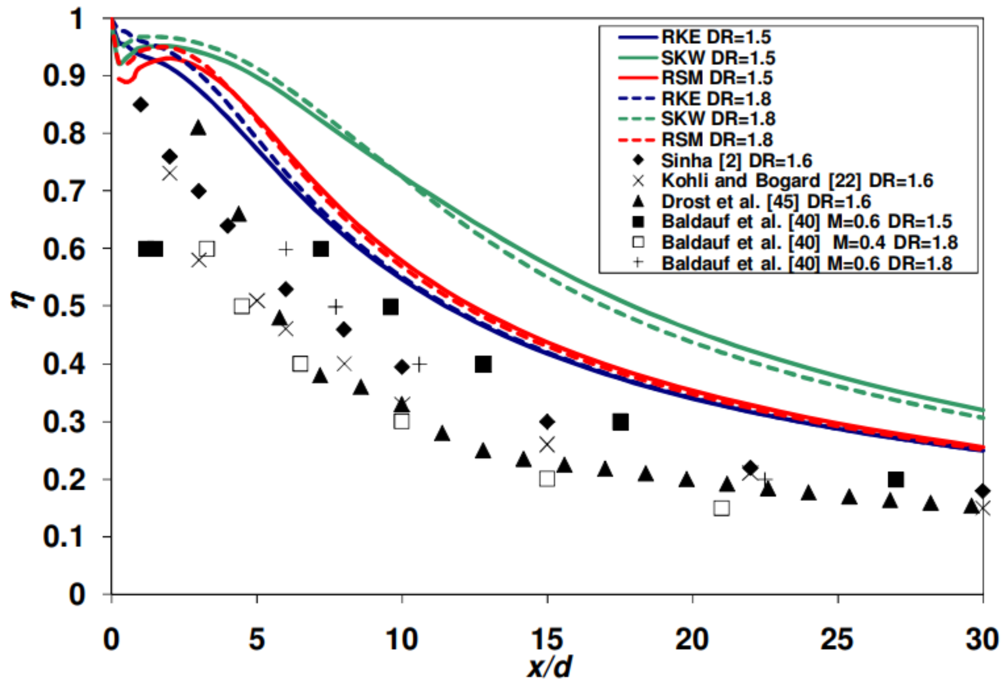

Figure 2-30: Centerline effectiveness predicted by the turbulence models and experimental results for M=0.5 [40]

Flat plate film cooling experiments have been simulated for cylindrical holes using realizable k-ε, standard k-ω and RSM turbulence models commonly described in literature [40]. Standard k-ω model has closely agreed with the laterally averaged experimental data while it was worst with centerline effectiveness data [40]. In contrast, the realizable k-ε model poorly predicted the laterally averaged experimental data and well predicted the centerline data [40]. The anisotropic RSM model has not predicted actual lateral spreading compared to the other models even though the jet in cross flow is anisotropic in nature [40]. The predicted results by realizable k-ε, standard k-ω and RSM turbulence models have been depicted by Figure 2-29 and Figure 2-30. In addition, a comparison between the predictions and the experimental data has also been shown in the same figures.

A summary of several numerical simulation studies in recent past is given in Table 2-1.

Table 2-1: A summary of numerical simulation studies

Reference	**Title**	**Hole shape**	**Turbulence model**	**Year**
[43]	Cooling Effectiveness for a Shaped Film Cooling Hole at a Range of Compound Angles	Laidback fan-shaped hole (7-7-7 shaped hole)	RANS Realizable k-ε	2019
[44]	CFD Simulations of Film Cooling Effectiveness and Heat Transfer for Annular Film Hole	Cylindrical	RANS k-ω for heat transfer coefficient and RANS k-ε for effectiveness	2016
[45]	Comparison Between Different Isotropic And Anisotropic Eddy Viscosity Models	Laidback fan shaped (7-7-7 shaped hole)	RANS turbulence models k-ε, k-ω, Reynolds Stress	2018
[46]	Modeling and Simulation of Film Cooling Effectiveness on a Flat Plate	Cylindrical	RANS Realizable k-ε with enhanced wall function	2020

[47]	Analysis of Heat Transfer on film cooling performance in a flat plate	Cylindrical	RANS Realizable k-ε and Enhanced Wall Treatment	2019
[48]	Unsteady Simulations of a Film Cooling Flow from an Inclined Cylindrical Jet	Cylindrical	URANS	2010
[49]	Preliminary Computational Analysis of Film Cooling on a Flat Plate at Different Blowing Ratios	Cylindrical	RANS and LES	2020
[50]	Large Eddy Simulation of Inclined Jet in Cross Flow with Cylindrical and Fan-shaped Holes	Cylindrical and fan-shaped holes	LES	2016
[51]	Large-eddy simulation of film cooling flows at density gradients	Cylindrical	LES	2008
[52]	Near Field of Film Cooling Jet Issued Into a Flat Plate Boundary Layer: LES Study	Cylindrical	LES	2008
[53]	Large-eddy simulation of an inclined round jet issuing into a cross-flow	Cylindrical	LES	2014
[54]	Large Eddy Simulations Of Film Cooling Flow	Cylindrical and shaped holes	LES	2008

	Fields From Cylindrical And Shaped Holes			
[55]	Large Eddy Simulations of Discrete Hole Film Cooling With Plenum Inflow Orientation Effects	Cylindrical	LES	2013
[56]	Effects of Density and Blowing Ratios on the Turbulent Structure and Effectiveness of Film-Cooling	Cylindrical	LES	2018
[57]	Large eddy simulation of the trenched film cooling hole with different compound angles and coolant inflow orientation effects	Cylindrical	LES	2019
[11]	Large eddy simulation of film cooling flow from round and trenched holes	Trenched cylindrical	LES	2019
[58]	A numerical study of anti-vortex film-cooling holes designs in a 1-1/2 turbine stage using LES	Cylindrical	LES	2019
[59]	Large eddy simulation of compressible, shaped-hole film cooling	Shaped hole (7-7-7)	LES	2019
[60]	Large Eddy Simulation of Film Cooling Flow from a Fan-shaped Hole	Fan-shaped	LES	2017

[61]	LES of rotating film-cooling performance in a 1-1/2 turbine stage	Cylindrical	LES	2019
[62]	Large eddy simulation of compound angle hole film cooling with hole length-to-diameter ratio and internal cross-flow orientation effects	Cylindrical	LES	2017
[5]	Large Eddy Simulation of the Film Cooling Flow System of Turbine Blades: Public Shaped Holes	Shaped hole (7-7-7 shaped hole)	LES	2016
[63]	Hybrid LES-RANS study of an effusion cooling array with circular holes	Cylindrical	LES-RANS	2019
[64]	Large eddy simulation of the 7-7-7 shaped film cooling hole at axial and compound angle orientation	Shaped hole (7-7-7 shaped hole)	LES	2020

3 METHODOLOGY

3.1 Geometry of Computational Domain

As illustrated by Figure 3-1, the geometry of standard 7-7-7 shaped hole was created [24]. The hole exit is made of 7^0 forward expansion and 7^0 lateral expansion. The cylindrical shape is found at the inlet portion of the hole and the exit diffuser part has expansion in lateral and streamwise direction. The diameter of the cylindrical portion is 7.75 mm. All the geometry parameters are shown by Table 3-1. The computational domain is shown by Figure 3-2 for the whole geometry. It consists of a single hole with symmetry boundary conditions to simplify the domain and to save the simulation time. The distance between the centers of two adjacent cooling holes is defined as the pitch. The injection angle (α) was set to 30^0 while the laidback angle (β_{fwd}) and lateral angle (β_{lat}) were 7^0 each.

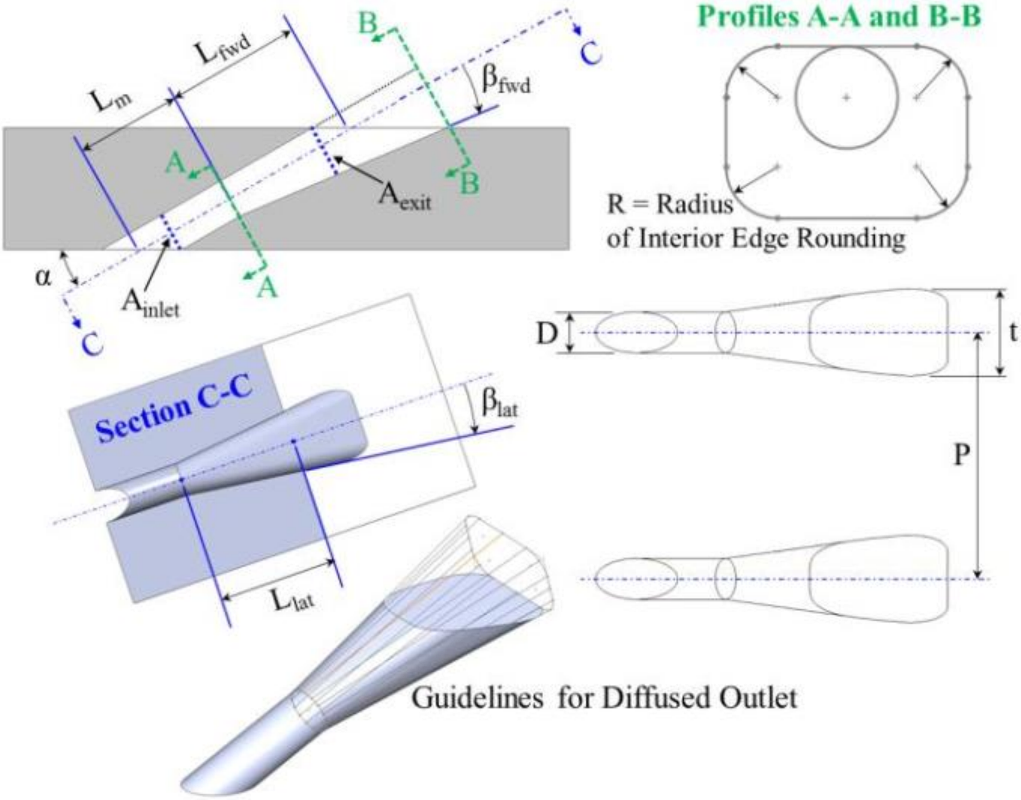

Figure 3-1: Design of Shaped Hole [24]

Table 3-1: Geometric Parameters for 7-7-7 shaped hole [24]

Geometry Parameter	Value
Injection angle, α	30^0
L_m/D	2.5
L_{lat}/D and L_{fwd}/D	3.5
L/D	7
Laidback angle, β_{fwd}	7^0
Lateral angle, β_{lat}	7^0
P/D	6
Converge, t/P	0.35
Area ratio, $AR = A_{exit}/A_{inlet}$	2.5
R/D	0.5

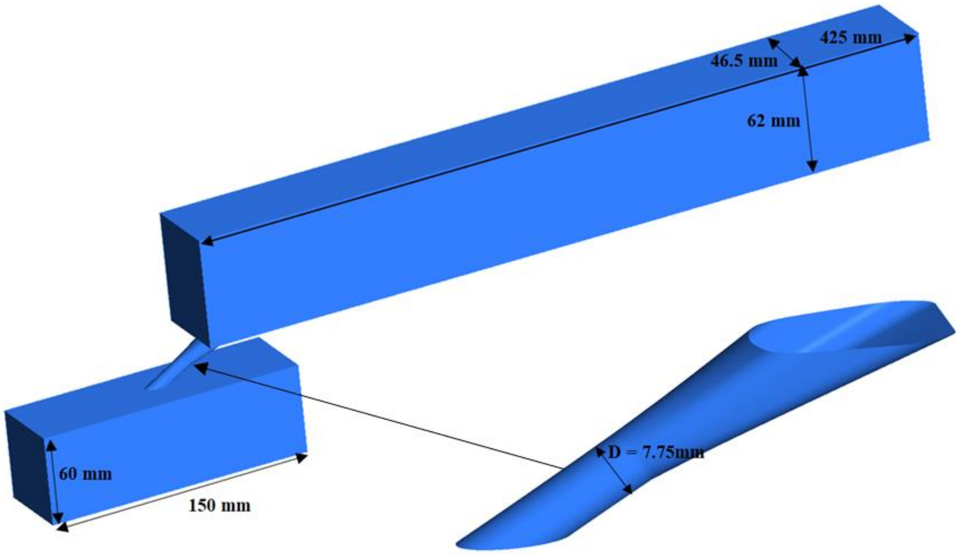

Figure 3-2: Geometry of the computational domain

In this study, the validation was performed using the results generated by the experiment done by Schroeder at el. [24]. Figure 3-3 shows the experimental set-up that they have used. Dried air produced in desiccant vent dryer is flowing through the heat exchanger to be produced cooled air by liquid nitrogen. The cooled air is then supplied to a raw of five shaped cooling holes via the plenum, which has 7.75 mm diameter of each hole. The cooling holes made on test section injects to the mainstream. Electric heating elements and chilled water heat exchanger produce the mainstream air at 295 K. The boundary layer produced by the incoming heated air flow on the flat plate is sucked before entering the test section. Then, a new boundary layer is produced at the onset of the flat plate and it is tripped to make the transition from laminar to turbulent. The surface temperature is determined by an infrared camera and then the adiabatic film cooling effectiveness is determined. Adiabatic test plate has been maintained by using heated box added below tunnel which the hot mainstream temperature was matched [65].

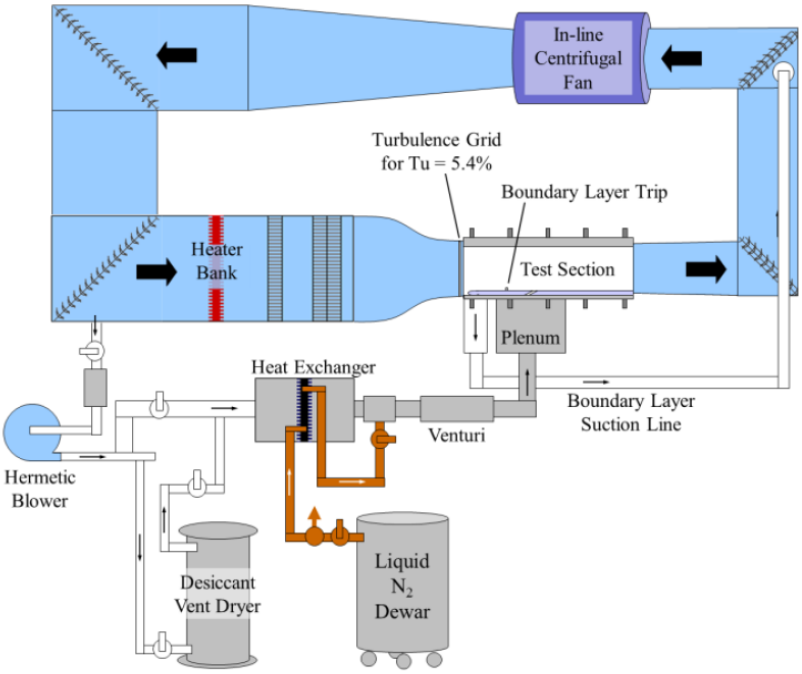

Figure 3-3: Experimental set-up [24]

As shown in Figure 3-4, downstream distance (X) is measured from the hole trailing edge while the pitchwise distance (Z) is measured from the hole center in the lateral direction. The vertical distance (Y) is measured from the surface to be cooled. Center line shown in Figure 3-4 is the geometric center line of the computational domain which is symmetric about the center line.

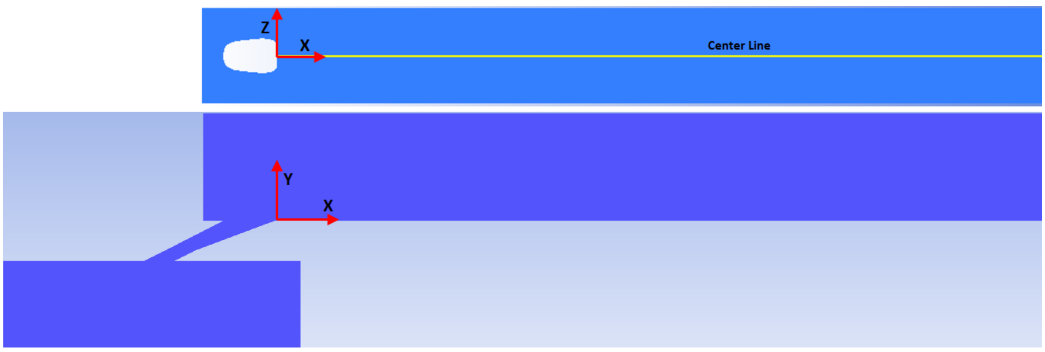

Figure 3-4: Coordinate directions for the computational domain

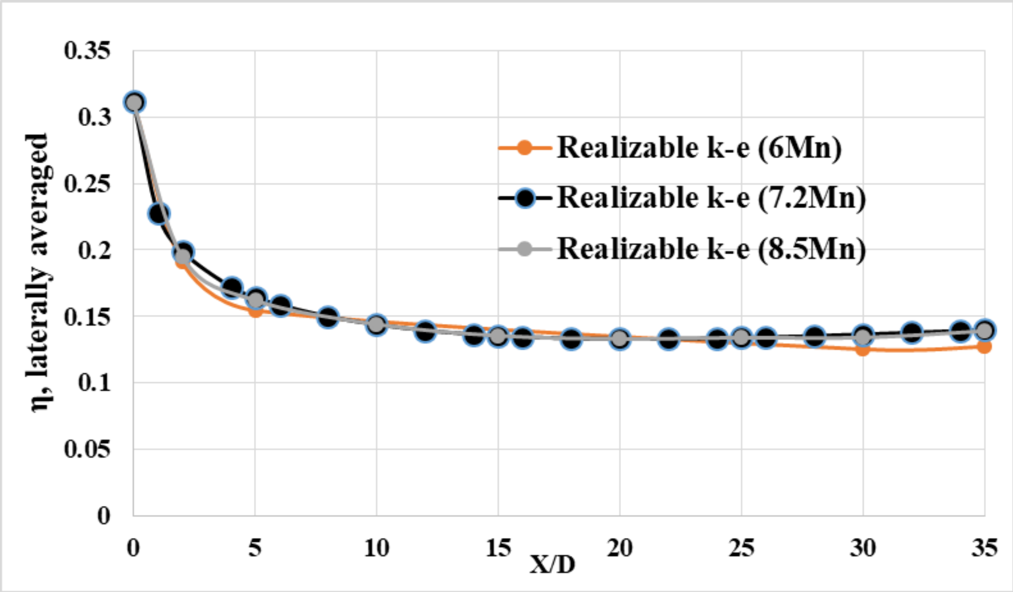

Figure 3-5: Mesh sensitivity analysis

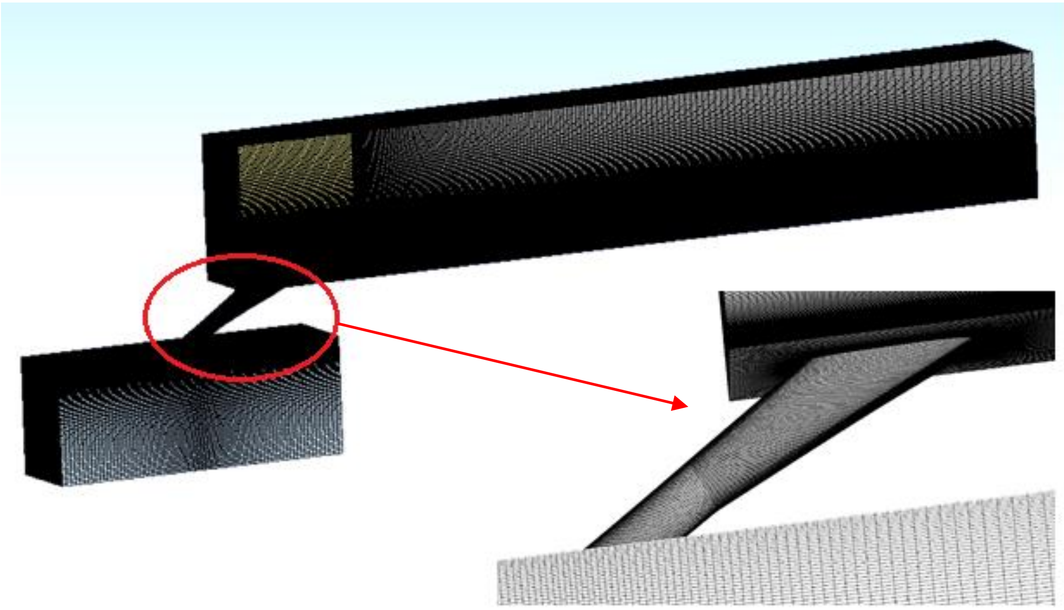

Figure 3-6: 3D computational domain for validation

3.2 Computational mesh with boundary conditions

The mesh independent solution was identified by running with several mesh levels. The laterally averaged adiabatic effectiveness data was taken at different mesh levels as shown in Figure 3-5. The hexahedra dominant mesh with 7.2 million elements was selected with the available computer performance. The mesh was refined near the bottom flat plate as shown in Figure 3-6 such that the Y+ value near the adiabatic flat plate was below 1. The distance between the hole exit and the mainstream inlet was set such that the fully turbulent boundary layer at the mainstream inlet is allowed to enter the domain. The mainstream inlet boundary conditions were set based on the given profiles of turbulent mean velocity and turbulent velocity fluctuations as shown in Figure 3-7 and Figure 3-8.

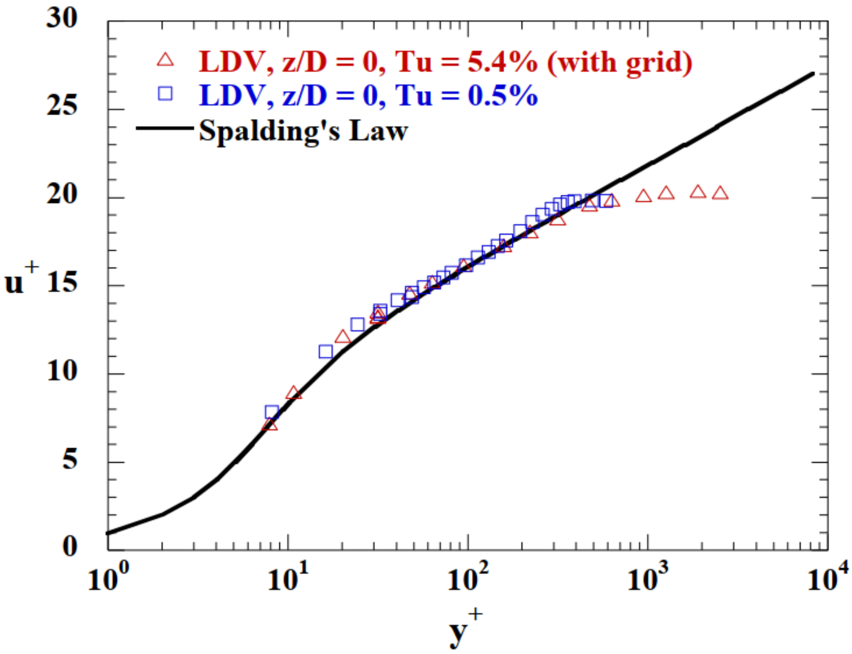

Figure 3-7: Turbulent boundary layers measured at x/D = -4.7, with and without the upstream turbulence grid [24]

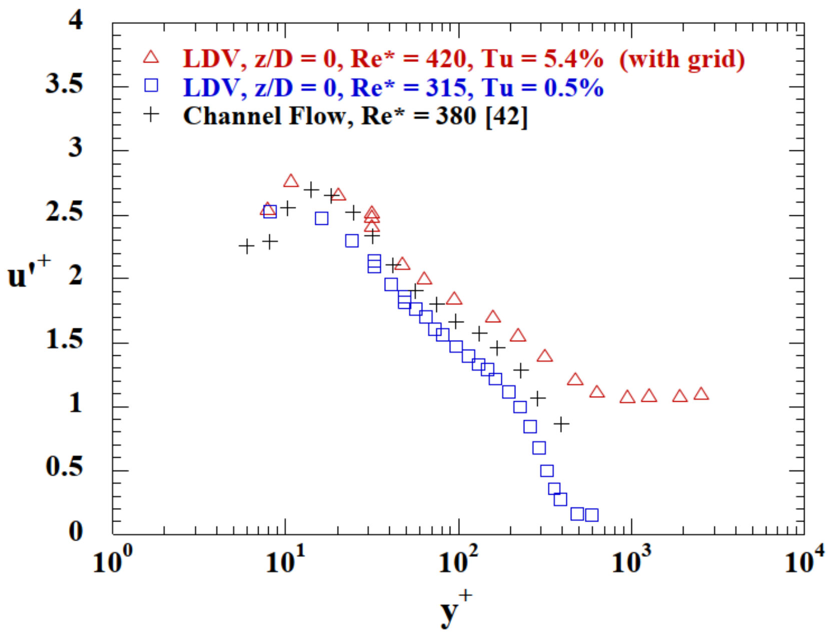

Figure 3-8: Profiles of streamwise velocity fluctuation at x/D = -4.7, with and without the upstream turbulence grid [24]

The inlet plenum located at the film hole inlet was set to pressure boundary conditions. Then, the pressure was changed to achieve the blowing ratios of the cases. Exit of the mainstream was set at the atmospheric condition as mentioned in the experimental study. The sides of the hot mainstream and inlet plenum were set to symmetry boundary conditions considering a raw of film holes while the bottom flat plate was set as an adiabatic wall to be consistent with the experimental conditions as shown in Figure 3-9. The top face of the mainstream domain was set to wall boundary condition with zero shear stress. No-slip and adiabatic wall boundary condition were set to the wall of the hole. All boundary conditions set are shown in Figure 3-9.

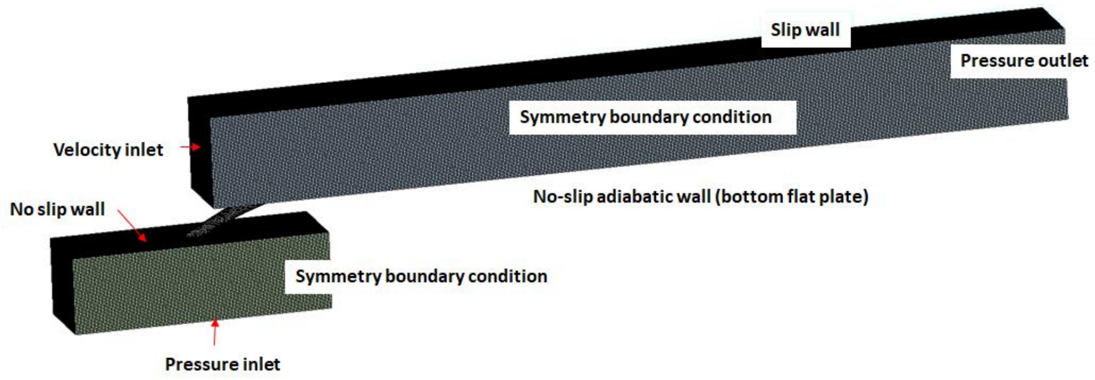

Figure 3-9: Boundary conditions

In the present study free-stream turbulence intensity and density ratio were maintained at 0.5% and 1.5 respectively. 3D geometry of the computational domain with trench geometry which is continuous slot in lateral direction has been shown in Figure 3-10. The width of the trench (w) was similar to the width of the hole exit while height of the trench (h) was non-demensionalized as h/D which has been varied in modified geometry cases with trench. Figure 3-11 shows the final 3D computational mesh of the domain with the trench geometry.

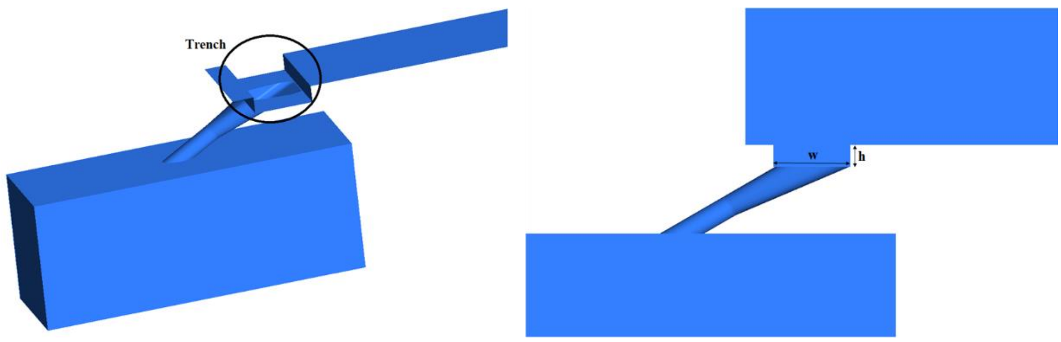

Figure 3-10: 3D geometry of computational domain with trench

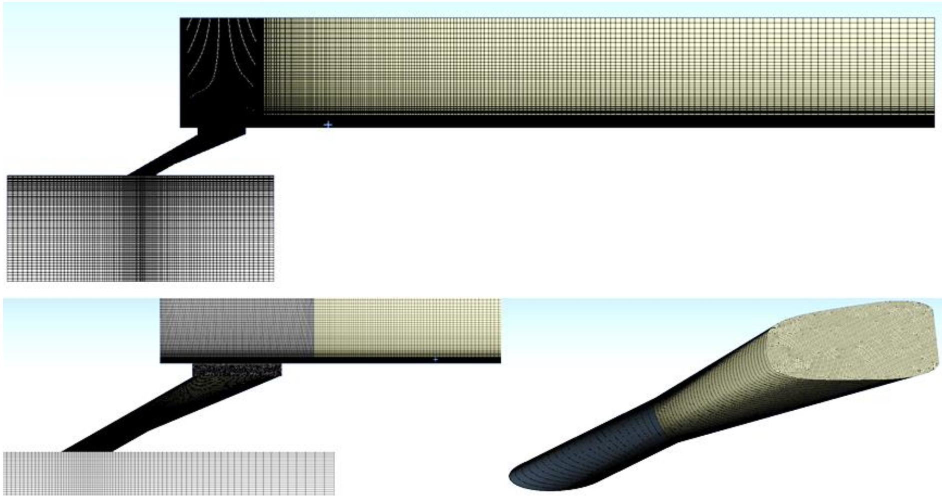

Figure 3-11: 3D computational mesh of shaped hole with trench

3.3 Numerical Simulation

Three turbulence models which are standard k-ω (SKW), SST k-ω (SST KW) and realizable k-ε (RKE) were selected based on their capability of solving boundary layer flows and the past studies to simulate cylindrical film holes and some laidback fan shaped holes. The aforementioned turbulence models were validated using the experimental results of the 7-7-7 shaped hole and performed an assessment of the predictions of film cooling performance for this specific hole. Altogether six (6) cases were set up for validation as shown in Table 3-2. As a result of the validation, it was identified a most appropriate turbulence model that can be used in this study from the three models. A geometry modification, a trench (or can be said as shallow transverse slot in lateral direction) at the exit of the shaped hole was then made and generated numerical results using the most accurate turbulence model identified through the aforementioned assessment. Altogether twelve (12) cases were set up to produce predictions for the hole with trench geometry as shown in Table 3-3.

Pressure based solver with SIMPLE algorithm was used to generate numerical results using ANSYS Fluent solver. The energy equation has turned on to solve for temperature field. Realizable k-ε (RKE) model with enhanced wall treatment was selected to investigate the effect of geometry modification to the flow field and cooling performance. This turbulence model was selected based on the aforementioned assessment since it showed closer behavior to the experimental results. 3500 iterations were run for all cases throughout the research. All results were extracted by using Ansys CFD post.

Table 3-2: Number of cases for validation

Case Number	Blowing ratio (M)	Turbulence model
1	1.5	RKE
2		SKW
3		SST KW
1	3.0	RKE
2		SKW
3		SST KW

For shaped holes, increasing free-stream turbulence intensity increases the lateral spreading of coolant due to the increase of velocity fluctuations surrounding the coolant jet as well as laterally averaged effectiveness is decreased by increasing the free-stream turbulence intensity [25]. Increasing density ratio increases laterally averaged effectiveness at higher blowing ratios such as M = 3 [24]. Therefore, free-stream turbulence intensity (Tu) and density ratio (DR) were maintained at 0.5% and 1.5 respectively for all cases throughout the research to avoid their effects. Six (6) cases were run without the trench to evaluate the selected three turbulence models. Blowing ratio (M) of 1.5 and 3 were selected to match with the experimental conditions for comparison. The cases are given in Table 3-2.

Table 3-3: Number of cases for predictions for trench geometry

Case Number	Blowing ratio (M)	Trench depth ratio (h/D)
1	1.5	0 (baseline case)
2		0.25
3		0.5
4		1
5	3	0 (baseline case)
6		0.25
7		0.5
8		1
9	5	0 (baseline case)
10		0.25
11		0.5
12		1

Twelve (12) cases were run with the trench geometry as shown in Table 3-3. The optimum trench depth for cylindrical cooling hole has been identified as 0.75D [66]. Based on that study and with the interest to analyze cooling performance and flow field, a set of cases were produced by using h/D ratios of 0.25, 0.5 and 1. Furthermore, the literature related to cylindrical cooling holes with trench geometry was used to decide the values for depth ratios [11] [12].

According to Table 3-3, the baseline cases which are without the trench (Case number 1, 5, and 9) were produced to compare with the modified cases with trench geometry. Other nine cases were used to produce predictions at different depth ratios. In turn, the effect of trench geometry was analyzed on the film cooling effectiveness.

3.4 Important parameters of film cooling analysis

The present study used several important parameters for film cooling performance analysis. Adiabatic film cooling effectiveness, laterally averaged film cooling effectiveness were the primary parameters for the analysis. Increasing film cooling effectiveness implies the higher cooling of the film cooling method. Adiabatic film cooling effectiveness has been defined under Introduction chapter. Laterally averaged adiabatic film cooling effectiveness is defined as below.

$$\bar{\eta} = \frac{1}{\Delta z} \int \eta \, dz$$

η represents the local adiabatic film cooling effectiveness while z represents the length in lateral direction. The other two parameters of blowing ratio (M) and density ratio (DR) have also been defined in Introduction chapter.

3.5 Important parameters of error analysis

During the validation process, the following important parameters were used to analyze the error of the predictions generated by the turbulence models.

Absolute error

$$Error\ (\%) = \frac{|y_i - y_{pi}|}{y_i} \times 100$$

Root-mean-squared error (RMSE)

$$RMSE = \sqrt{\frac{\sum_{i=1}^{N}(y_i - y_{pi})^2}{N}}$$

N = number of data points

R-square (R^2)

$$R^2 = 1 - \frac{SSR}{SST}$$

$$SSR = \sum_{i=1}^{N} (y_i - y_{pi})^2$$

$$SST = \sum_{i=1}^{N} (y_i - \bar{y})^2$$

y_i – i^{th} experimental value of the variable

y_{pi} − i^{th} predicted value of the variable

$\bar{y}$ − Mean of experimental data set

N − Number of data points

SSR – Sum of square of residuals

SST – Total sum of squares

R-square (or called coefficient of determination) was used to understand the degree to which the predictions fit the experimental results.

3.6 Turbulence model – Realizable k-ε

The RANS turbulence model which was used for the study was realizable k-ε after an evaluation of three turbulence models of standard k-ω, SST k-ω and realizable k-ε. The three models were used without any modifications and as provided by Ansys Fluent solver [67] [68] [69]. Realizable k-ε model used in the study of trench geometry is described below.

To close Reynolds Averaged Navier Stokes Equations (RANS), the nine Reynolds stresses have to be solved by using nine transport equations, which extremely costs in terms of time and computational power. Therefore the Reynolds stresses in RANS are modeled by using the equations of different turbulent quantities such as turbulent kinetic energy (k), turbulence dissipation rate (ε), and specific turbulence dissipation rate (ω). The realizable k-ε model used in this study, which is an eddy viscosity model, provides to calculate eddy viscosity using a new model equation for turbulent dissipation rate, ε. The turbulence model has adopted the following in contrast to the other two equation models.

- C_μ in the new eddy-viscosity equation is a variable and it is originally proposed by [70]
- The equation of the mean-square vorticity fluctuation is used to derive the new dissipation rate (ε) [69]

3.6.1 Model equations for k and ε

The model equation for k is,

$$\frac{\partial}{\partial x}(\rho k) + \frac{\partial}{\partial x_j}(\rho k u_j) = \frac{\partial}{\partial x_j}\left[\left(\mu + \frac{\mu_t}{\sigma_k}\right)\frac{\partial k}{\partial x_j}\right] + G_k + G_b + \rho k + Y_M + S_k \quad \text{------------- 3-1 [71]}$$

The model equation for ε is,

$$\frac{\partial}{\partial x}(\rho \varepsilon) + \frac{\partial}{\partial x_j}(\rho \varepsilon u_j) = \frac{\partial}{\partial x_j}\left[\left(\mu + \frac{\mu_t}{\sigma_\varepsilon}\right)\frac{\partial \varepsilon}{\partial x_j}\right] + \rho C_1 \varepsilon - \rho C_2 \frac{\varepsilon^2}{k+\sqrt{\nu\varepsilon}} + C_{1\varepsilon}\frac{\varepsilon}{k}C_{3\varepsilon}G_b + S_\varepsilon \quad \text{------------- 3-2 [71]}$$

Where

$$C_1 = max\left[0.43, \frac{\eta}{\eta+5}\right],\ \eta = S\frac{k}{\varepsilon},\ S = \sqrt{2S_{ij}S_{ij}}$$

G_k represents the turbulence kinetic energy created by the mean velocity gradients [71]. The turbulence kinetic energy generated by buoyancy is denoted by G_b [71]. Y_M denotes the fluctuating dilatation in turbulence of compressible flows. [71]. C_1 and $C_{1\varepsilon}$ represents constant [71]. The turbulent prandlt numbers are denoted by σ_k and σ_ε for k and ε respectively [71]. S_k and S_ε are source terms and defined by user" [71].

The equation for ε is derived using the model equation of mean-square vorticity fluctuation, $\overline{\omega_\iota\omega_\iota}$ [69]. For large turbulent Reynolds number, $\varepsilon = \nu\overline{\omega_\iota\omega_\iota}$ [72, 69]. It is derived a new equation for ε applying this relationship to the model equation of $\overline{\omega_\iota\omega_\iota}$.

3.6.2 Modeling turbulent viscosity

In other k-ε models, the turbulent viscosity is calculated as follows,

$$\mu_t = \rho C_\mu \frac{k^2}{\varepsilon} \quad \text{------------- 3-3}$$

In contrast to other k-ε models, C_μ as shown in equation 3-3 is no longer constant in RKE. The following realizability conditions were used to produce a formula for C_μ.

The first realizability condition is to maintain positivity of normal Reynolds stresses shown below, which is obtained based on the Bosseneque hypothesis.

$$\overline{u^2} = \frac{2}{3}k - 2\nu_t \frac{\partial U}{\partial x}, \nu_t = \frac{\mu_t}{\rho}$$

$\overline{u^2}$ which is positive by definition is negative when the large strain occurs in the flow. It is needed to ensure the positivity of the normal Reynolds stresses,

Therefore, $\overline{u_\alpha^2} \geq 0, (\alpha = 1, 2, 3)$

The second realizability condition is to satisfy Schwarz's inequality between any fluctuating components shown as below.

$$\frac{\overline{u_\alpha u_\beta}^2}{\overline{u_\alpha^2}\,\overline{u_\beta^2}} \leq 1, (\alpha = 1, 2, 3;\ \beta = 1, 2, 3)$$

According to the realizability conditions, Shih et al [73] proposed the following formula for C_μ.

$$\boldsymbol{C_\mu = \frac{1}{A_0 + A_S \frac{kU^*}{\varepsilon}}} \quad \textbf{------------- 3-4}$$

Where

$$U^* = \sqrt{S_{ij}S_{ij} + \tilde{\Omega}_{ij}\tilde{\Omega}_{ij}}$$

And

$$\tilde{\Omega}_{ij} = \Omega_{ij} - 2\varepsilon_{ijk}\omega_k \ , \quad \Omega_{ij} = \bar{\Omega}_{ij} - \varepsilon_{ijk}\omega_k$$

Where $\bar{\Omega}_{ij}$ represents mean rate-of-rotation tensor relative to a moving reference frame which the angular velocity is ω_k.

A_0 and A_S which are constants are given by,

$$A_0 = 4.04 \ ; \quad A_S = \sqrt{6}\cos(\phi)$$

Where

$$\phi = \frac{1}{3}\cos^{-1}\left(\sqrt{6}\mathrm{W}\right), \qquad W = \frac{S_{ij}S_{jk}S_{ki}}{\tilde{S}^3}, \qquad \tilde{S} = \sqrt{S_{ij}S_{ij}}\,, \qquad S_{ij} = \frac{1}{2}\left(\frac{\partial U_j}{\partial x_i} + \frac{\partial U_i}{\partial x_j}\right)$$

It can be seen that the mean strain and rotation rates, the angular velocity of the system rotation, and the turbulence fields (k and ε) are the variables of the function of C_μ [71].

3.6.3 Two layer model in enhanced wall treatment

Enhanced wall treatment method was used to solve the flow near to the wall. This method was used with realizable k-ε turbulence model. In this method, viscosity-affected region very close to the wall and fully turbulent outer region are considered as the two regions to perform calculations [71]. The two regions are demarcated by turbulent Reynolds number as defined below.

$$Re_y = \frac{\rho y \sqrt{k}}{\mu}$$

Where, y represents the distance normal to the wall, calculated at the cell center.

In fully turbulent region, ($Re_y > Re_y^*$; $Re_y^* = 200$) the k-ε models such as standard, RNG, and realizable k-ε models or the Reynolds Stress Models (RSM) are utilized [71]. In the viscosity-affected region($Re_y < 200$), Wolfstein's one-equation model is used [71]. The momentum equation and the k equation used in standard, RNG, and realizable k-ε models and Reynolds Stress Model (RSM) are utilized [71].

The turbulent viscosities in the two regions are calculated separately using the k and ε quantities as mentioned above [71]. Then the two viscosities are blended using blending function to produce smooth variation of turbulent viscosity over the two regions [71]. The blending function helps to converge the solution due to the smooth variation [71]. If the entire flow domain can be considered in the viscosity-affected region ($Re_y < 200$), ε is obtained algebraically without using transport equation [71].

4 RESULTS AND DISCUSSION

4.1 Validation

The validation of RANS modeling was done using the numerical results generated by the selected three turbulence models, which are standard k-ω (SKW), SST k-ω (SST KW), and realizable k-ε (RKE). The numerical results of cooling effectiveness obtained from the simulations were compared with the experimental results presented by Shroider and Thole [24]. The simulated velocity profiles were compared with the experimental results generated by Shroider and Thole [25]. All cases were simulated with DR = 1.5 and M = 3.0 and 1.5 while the free-stream turbulence is 0.5%.

Figure 4-1, Figure 4-2, Figure 4-3, Figure 4-4, Figure 4-5, and Figure 4-6 show the mean streamwise velocity profiles at different locations of x/D = -2.4, -0.4 and 1.6 on the centerline plane. x/D = -2.4 and -0.4 are the locations where are over the outlet of the shaped hole. Large deviations from experimental results have been generated near the wall while simulation results are very close to the experimental results when perpendicularly moving upward from the wall.

4.1.1 Velocity distribution in cross flow

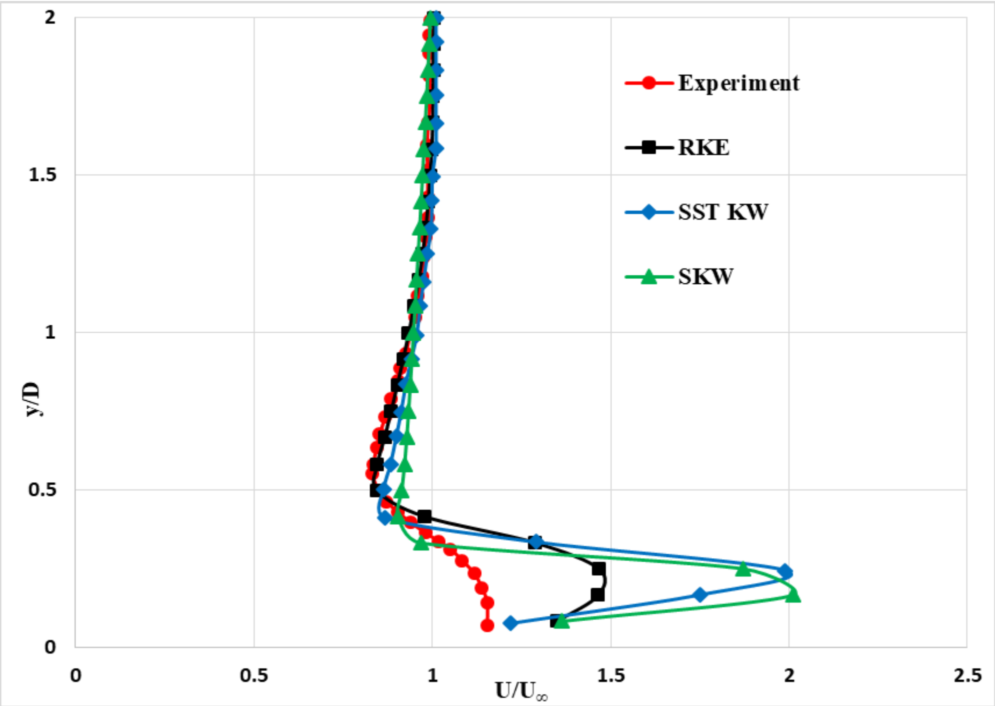

Figure 4-1: Streamwise velocity profiles in the centerline plane at X/D = -2.4 for M = 3, DR = 1.5, and Tu = 0.5%

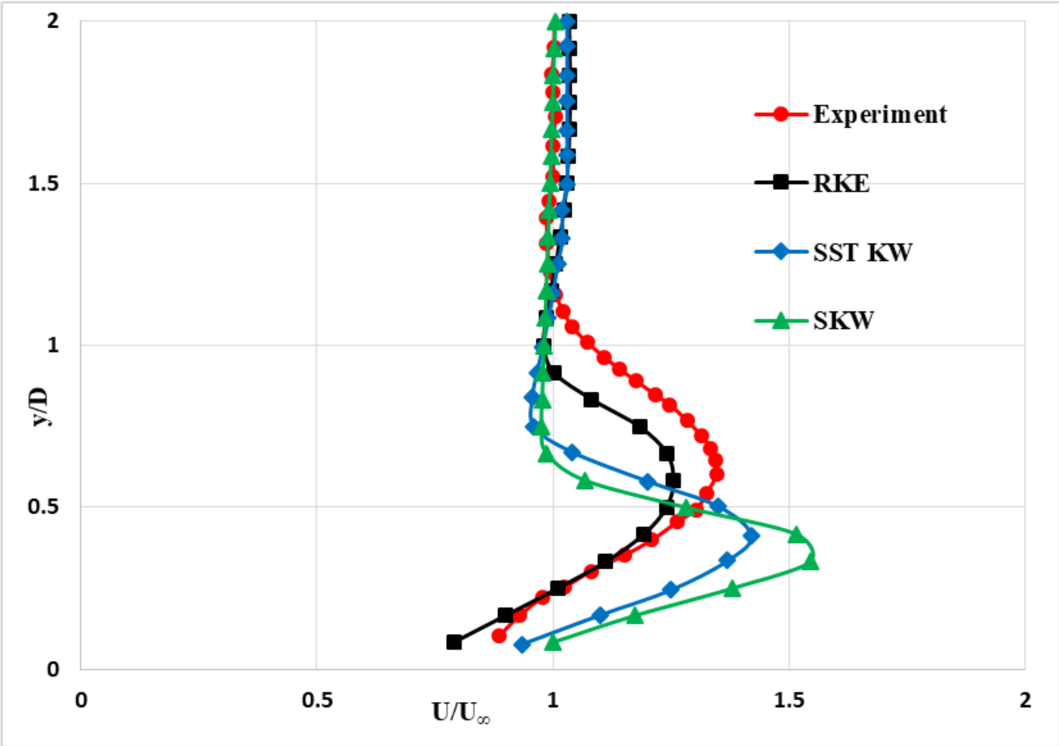

Figure 4-2: Streamwise velocity profiles in the centerline plane at X/D = -0.4 for M = 3, DR = 1.5, and Tu = 0.5%

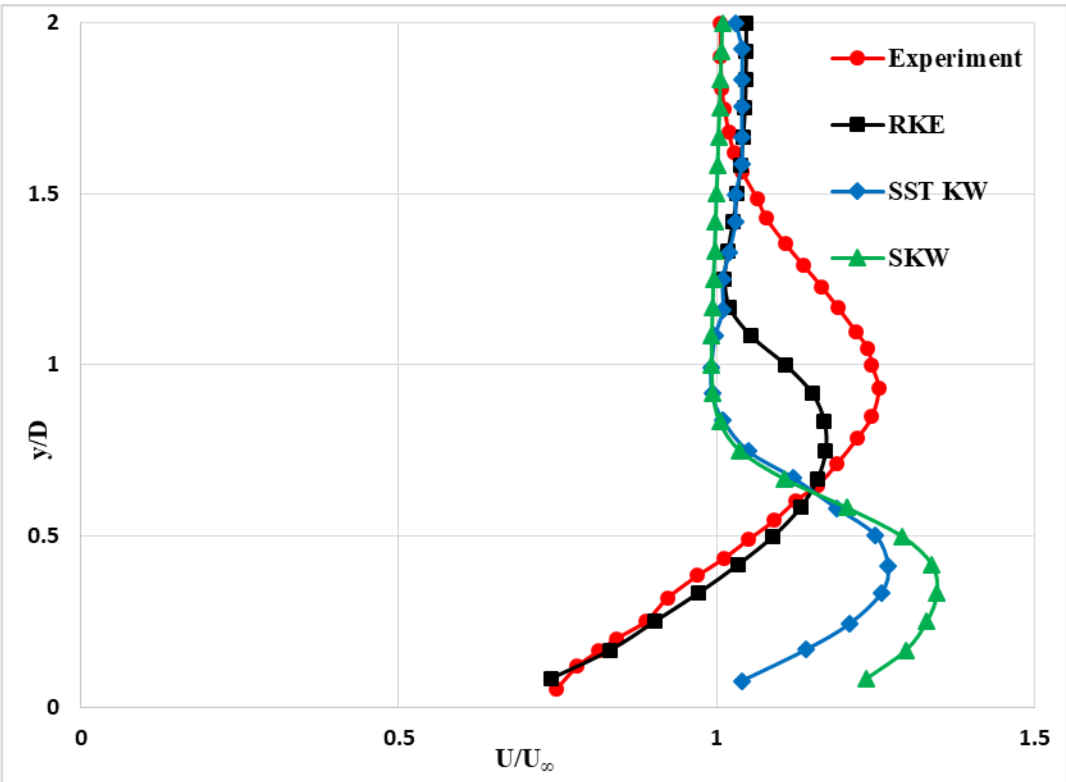

Figure 4-3: Streamwise velocity profiles in the centerline plane at X/D = 1.6 for M = 3, DR = 1.5, and Tu = 0.5%

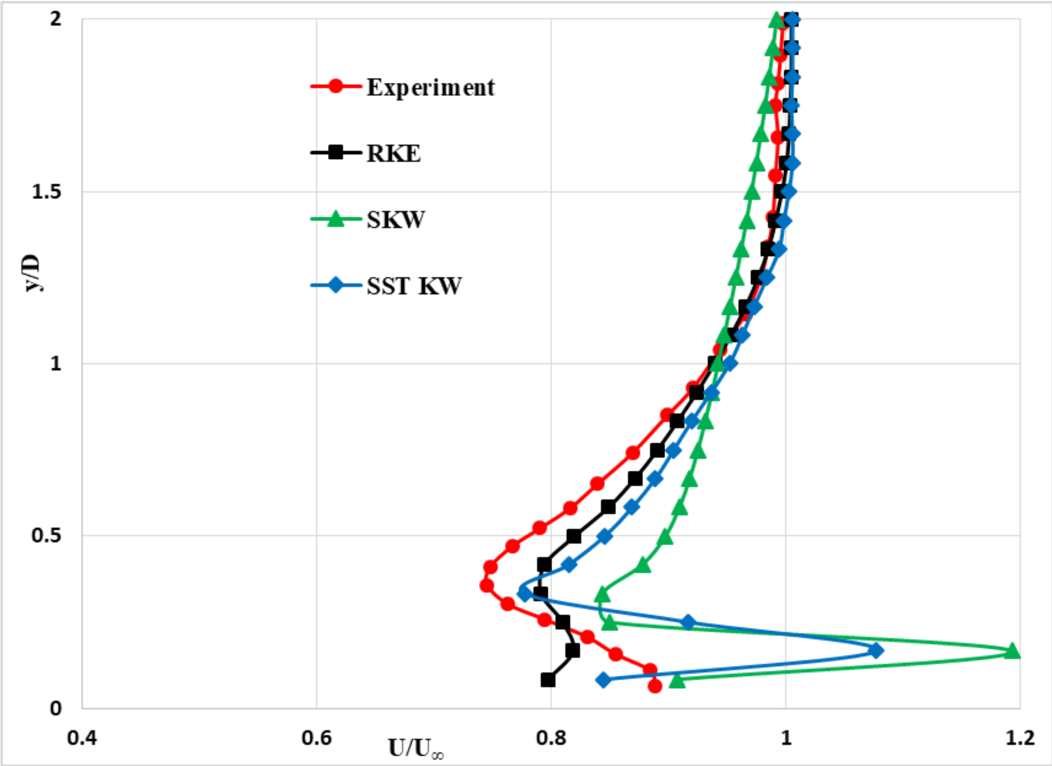

Figure 4-4: Streamwise velocity profiles in the centerline plane at X/D = -2.4 for M = 1.5, DR = 1.5, and Tu = 0.5%

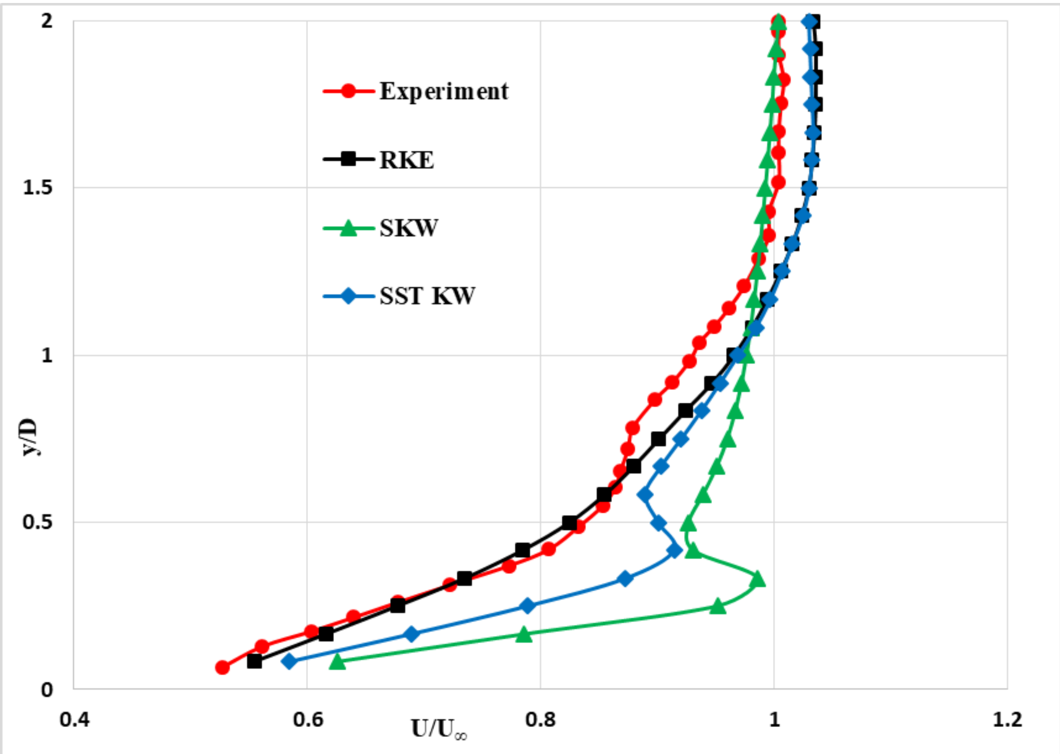

Figure 4-5: Streamwise velocity profiles in the centerline plane at X/D = -0.4 for M = 1.5, DR = 1.5, and Tu = 0.5%

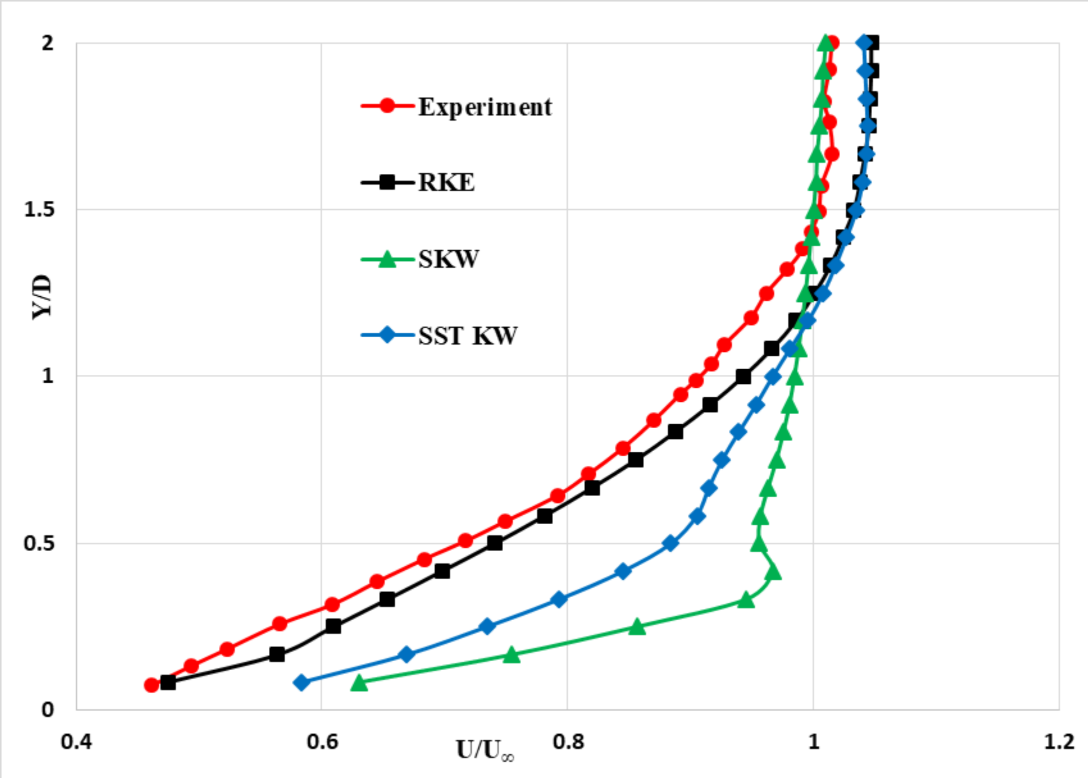

Figure 4-6: Streamwise velocity profiles in the centerline plane at X/D = 1.6 for M = 1.5, DR = 1.5, and Tu = 0.5%

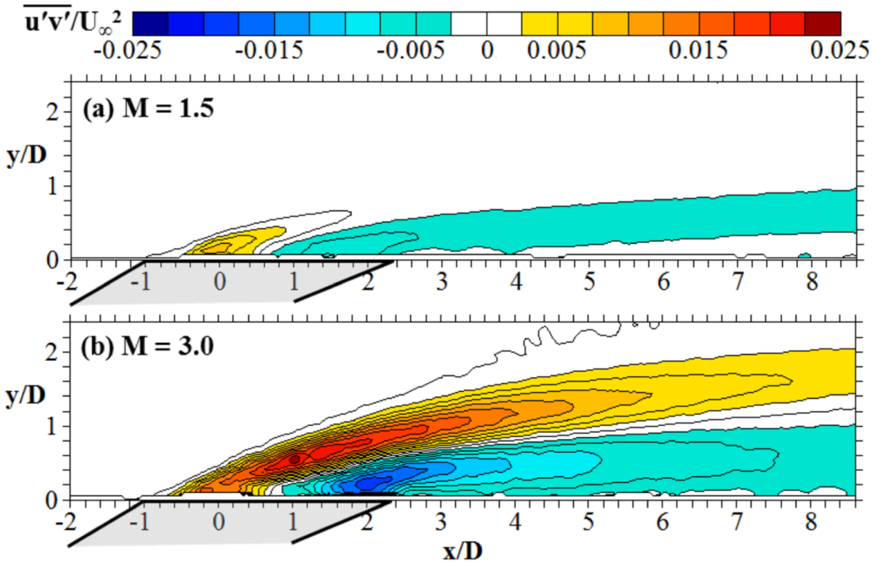

Figure 4-7: Contour of turbulent shear stress in the centerline plane for (a) M = 1.5 (b) M = 3 [25]

Based on the experiment results shown in Figure 4-7, turbulent shear stress $(\overline{u'v'}\ U_{\infty})$of the coolant jet region after injection is high at M = 3 compared to M = 1.5 case as well as is spread over large area above the surface [25]. Due to the jet penetration into the mainstream at M = 3, the coolant jet lifts off from the surface and the highest turbulent shear stress has taken place above the surface than that of the M = 1.5 case as shown in Figure 4-7 (a). High turbulent mixing in jet-mainstream shear layer region is high due to high turbulent diffusion of momentum. These processes have not been properly modeled by the selected RANS turbulence model. However, RKE model has predicted to a considerable extent for M = 3 in comparison to the other two. On the other hand, the coolant jet is highly anisotropic therefore isotropic turbulence models are barely captured the actual flow field in the near wall region in y direction (approximately up to y/D = 1 for M = 3) [64]. As shown in Figure 4-1, Figure 4-2, and Figure 4-3, large deviations in mean streamwise velocity plots in near wall region can be explained by that the high turbulent shear stress with high turbulent diffusion and the anisotropy are dominant. However the deviations for M = 1.5 are less than that of M = 3 as shown in Figure 4-4, Figure 4-5, and Figure 4-6, since the aforementioned turbulence processes are not strong as shown by M = 3 case.

4.1.1.1 Error analysis of velocity profiles

Table 4-1: Error analysis of velocity predictions

	M = 1.5			M = 3		
	RKE	**SST KW**	**SKW**	**RKE**	**SST KW**	**SKW**
x/D = -2.4						
Max error (%)	10.73	29.34	43.27	34.44	82.37	73.77
Min error (%)	0.11	0.07	0.09	0.17	0.23	0.13
RMSE	0.028	0.063	0.089	0.122	0.229	0.242
x/D = -0.4						
Max error (%)	4.87	18.20	40.57	13.57	25.55	36.72
Min error (%)	0.07	1.76	0.01	0.16	0.25	0.41
RMSE	0.025	0.058	0.100	0.070	0.149	0.190
x/D = 1.6						
Max error (%)	10.53	31.07	53.76	14.74	39.43	61.47
Min error (%)	1.47	2.55	0.27	0.84	1.03	0.70
RMSE	0.033	0.099	0.152	0.077	0.188	0.239

Table 4-1 has shown maximum and minimum percentage error and root-mean-squared error (RMSE) of velocity predictions from the three turbulence models at the locations of x/D = -2.4, -0.4 and 1.6. The lowest maximum percentage error has occurred by RKE model for M = 1.5 and 3 though the model has shown higher maximum error (34.44%) for M = 3. The lowest RMSE of the velocity profiles for each locations has occurred in RKE results compared to the other models. In general, the maximum percentage error for M = 3 is larger than that of M = 1.5 since the degree of turbulence diffusion and anisotropy of the coolant jet is higher for M = 3 compared to M = 1.5. Based on the error analysis of velocity profiles, it can be concluded that RKE model is used to predict the flow field for the 7-7-7 shaped hole with trench in the present study.

Table 4-2 has shown R-square values of the predictions generated by each turbulence model. In comparison to the other models, higher R^2 values are available for RKE model at the all locations for M = 1.5 and 3 except x/D = -2.4 for M = 3. The exception was due to the very large deviation of predicted results from the experimental results in the region below y/D = 0.5. The higher R^2 values from RKE represent the best fit to the experimental results. Based on R^2 values in Table 4-2, RKE model has shown better suitability to predict velocity profiles than the other two models.

Table 4-2: R-Square values for each turbulence model

	M = 1.5			**M = 3**		
	RKE	**SST KW**	**SKW**	**RKE**	**SST KW**	**SKW**
x/D = -2.4						
R^2	0.890	-0.141	0.426	-1.206	-6.763	-7.669
x/D = -0.4						
R^2	0.965	0.443	0.814	0.721	-0.254	-1.033
x/D = 1.6						
R^2	0.963	0.228	0.671	0.654	-1.072	-2.361

4.1.2 Film cooling effectiveness distribution

As shown in Figure 4-8, laterally averaged film cooling effectiveness, which is length averaged in the lateral direction, calculated by each turbulence model was compared. Realizable k-ε model with enhanced wall treatment (EWT) predicted the experimental results well while standard k-ω and SST k-ω show considerable deviations. However, all three turbulence models have shown good agreement far downstream.

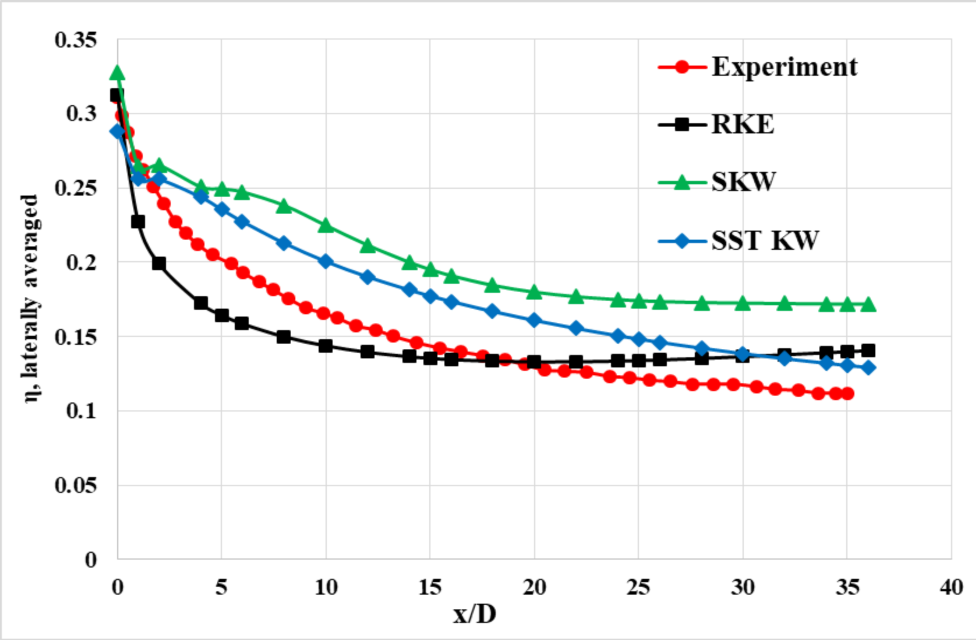

Figure 4-8: Laterally averaged film cooling effectiveness for M = 3

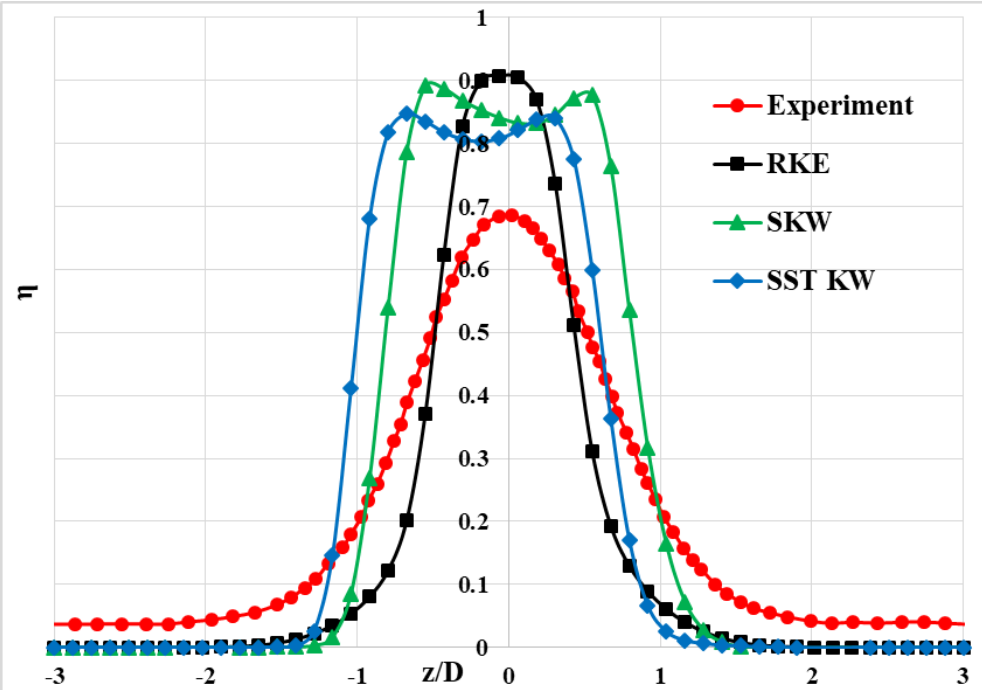

Figure 4-9: Lateral film cooling effectiveness at x/D = 5 for M = 3

Figure 4-9 shows local lateral film cooling effectiveness at downstream location, x/D = 5 while Figure 4-10 shows the same at x/D = 30. The separation region formed inside the diffuser section caused the bimodal effectiveness pattern. 7-7-7 shaped hole has been developed with expansion angles such that the bimodal pattern disappears [24]. At x/D = 5, the symmetric pattern produced by the experimental results has been predicted by realizable k-ε model as depicted by Figure 4-9 while the other two models have shown a bimodal pattern in the effectiveness. SST k-ω has skewed to the left-hand side maintaining the bimodal pattern. At x/D = 30, even though realizable k-ε model has shown the similar symmetric pattern compared to the experimental results, it shows a large over-prediction in the centerline region as shown in Figure 4-10.

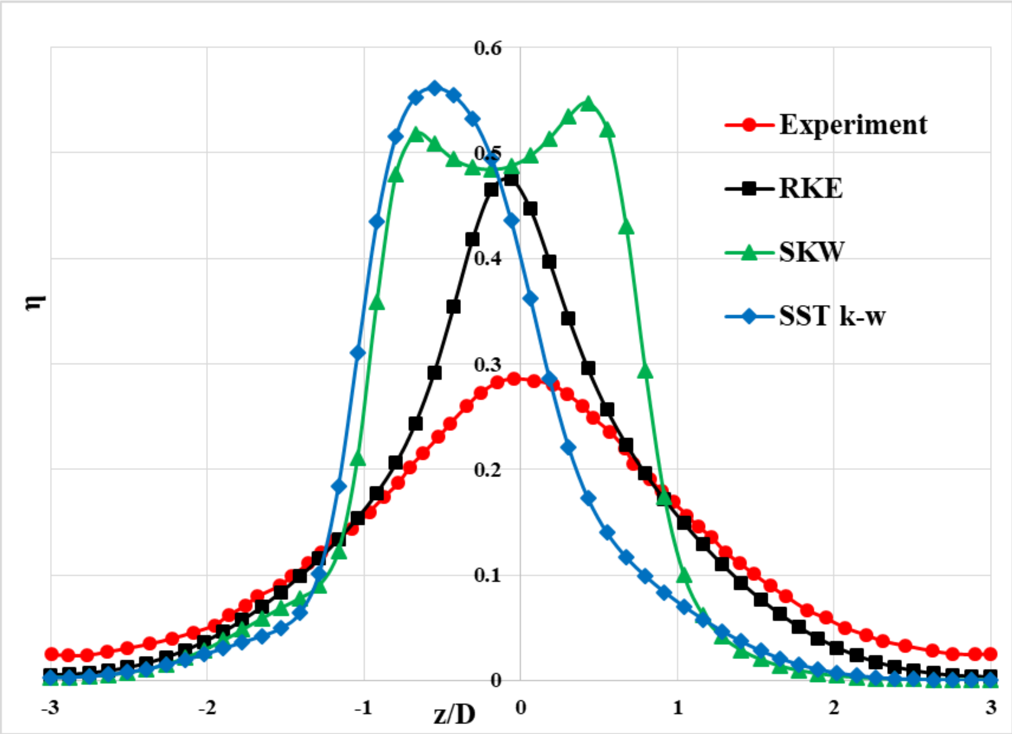

Figure 4-10: Lateral film cooling effectiveness at x/D = 30 for M = 3

Standard k-ω has shown a bimodal pattern while SST k-ω has skewed to the left-hand side. Figure 4-13 shows the predicted centerline effectiveness which shows considerable deviations. The largest deviation were found with realizable k-ε model as opposed to the other two models. However, SST k-ω and realizable k-ε have reached the experimental values far downstream. The bimodal pattern of the local effectiveness in lateral direction cannot be seen in 7-7-7 shaped hole due to its small expansion angle [13]. This small expansion angle makes the spatial extension of the separation region reduced [13]. As a result, the displacement of the fluid towards side walls of the diffuser is reduced [13]. Therefore the bimodal pattern of adiabatic effectiveness disappears. It can be seen that this behavior cannot be captured accurately by standard k-ω and SST k-ω turbulence model while realizable k-ε model has captured it to a considerable level as shown in Figure 4-9 and Figure 4-10.

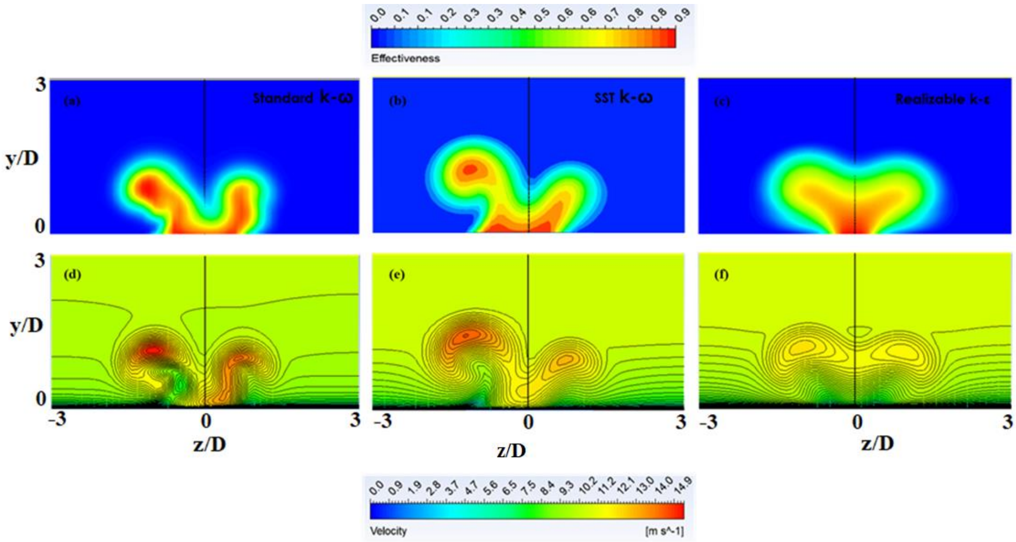

Figure 4-11: Contour plots of cooling effectiveness (a), (b), (c) and velocity (d), (e), (f) at x/D = 5 for M = 3

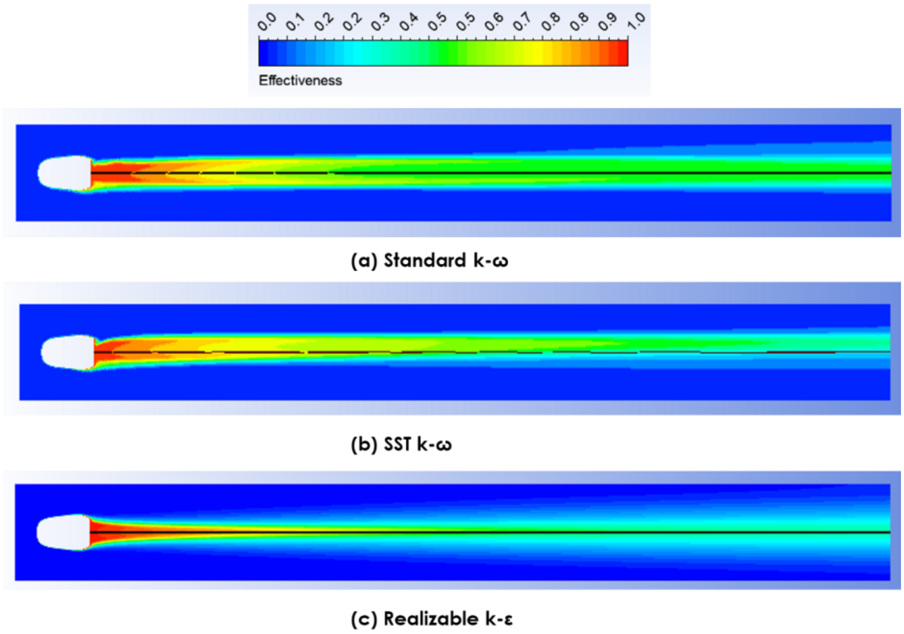

Figure 4-12: Film cooling effectiveness distributions on flat surface for M = 3

Figure 4-11 has shown contour plots of cooling effectiveness and velocity distributions generated by the results from RANS simulations with turbulence models of standard k-ω, SST k-ω and realizable k-ε. The black line shown in each plot is on centerline plane. As shown in (a) (d) and (b) (e) pairs of effectiveness and velocity plots, the two k-ω models have generated mainly two streaks of the coolant jet as the coolant exits the hole. The two streaks are thought to be generated due to poor prediction of in-hole flow field. As a result of splitting the coolant jet into two streaks, the cooling effectiveness has shown bimodal pattern as shown in Figure 4-12. However, realizable k-ε model has formed symmetric and one streak coolant jet after exiting the hole. As a result, symmetric coolant jet has developed without showing two maximums in lateral effectiveness variations as shown in Figure 4-11, Figure 4-12. It was similar to the experimental results.

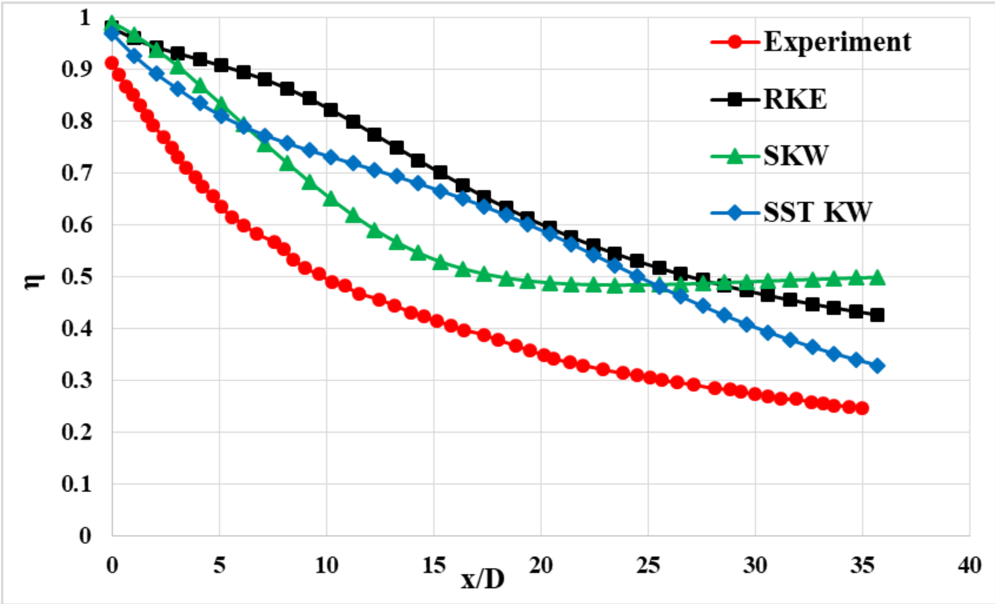

Figure 4-13: Centerline film cooling effectiveness for M = 3

For shaped holes and cylindrical holes, the jet-mainstream interaction contributed to form the CRVP which is the main flow feature generated outside of the hole [74, 38]. For shaped holes, the CRVP at a high blowing ratio such as M = 3 becomes strong and the coolant jet penetrates the mainstream [25]. The film cooling effectiveness and heat transfer are strongly affected by CRVP. The steady RANS turbulence models used in this study have been unable to produce the actual behavior of the flow field since horseshoe vortex, CRVP, wake vortices and shear layer vortices make the flow physics unsteady. However the RANS turbulence models have predicted steady characteristics of CRVP and other vortices with steady characteristics to a considerable extent. In addition, high turbulent transport and anisotropy of the flow, particularly in the near hole and centerline regions, are barely captured by the RANS turbulence models.

The models have been performed well far downstream as shown in Figure 4-8 and Figure 4-13 and near hole region as shown in Figure 4-8. The film cooling effectiveness at the downstream location of x/D = 5, as shown in Figure 4-9, are well predicted by realizable k-ε model compared to the cooling effectiveness at the location of x/D = 30 as shown in Figure 4-10. However the same pattern as the experimental results has maintained by this model. Thus it was concluded that the lateral spreading of film cooling effectiveness is not predicted well far downstream in cross flow. In conclusion, a better agreement to the experimental results was found with realizable k-ε model with enhanced wall treatment in comparison to the other two models.

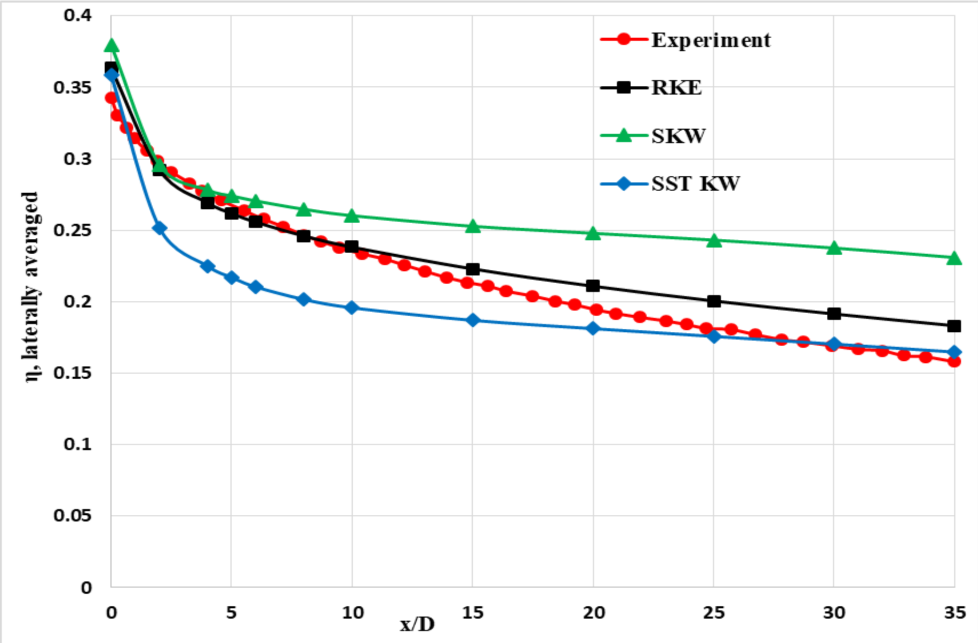

Figure 4-14: Laterally averaged film cooling effectiveness for M = 1.5

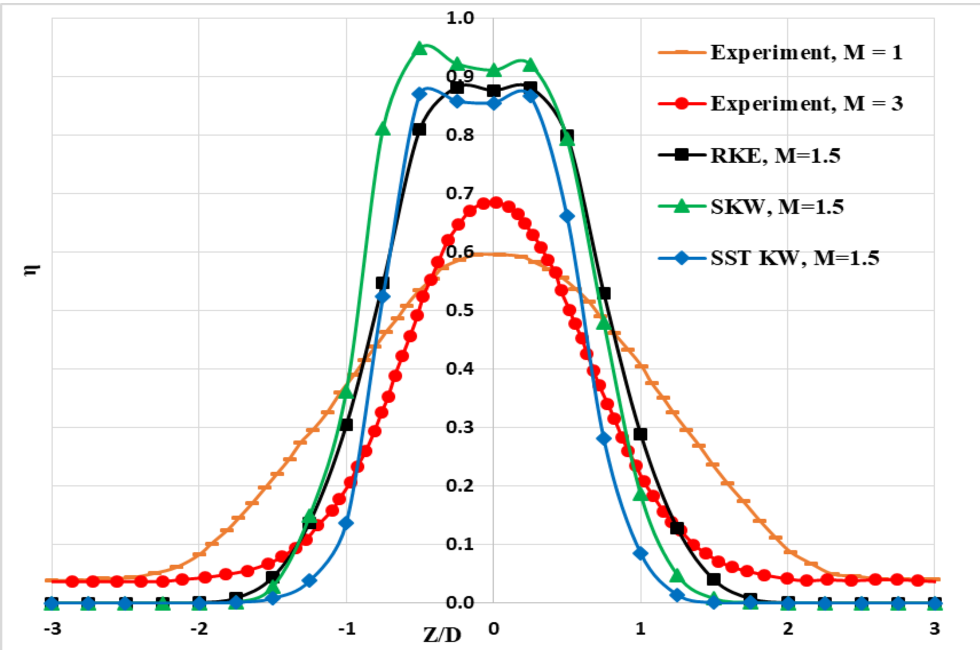

Figure 4-15: Lateral film cooling effectiveness at x/D = 5 for M = 1.5

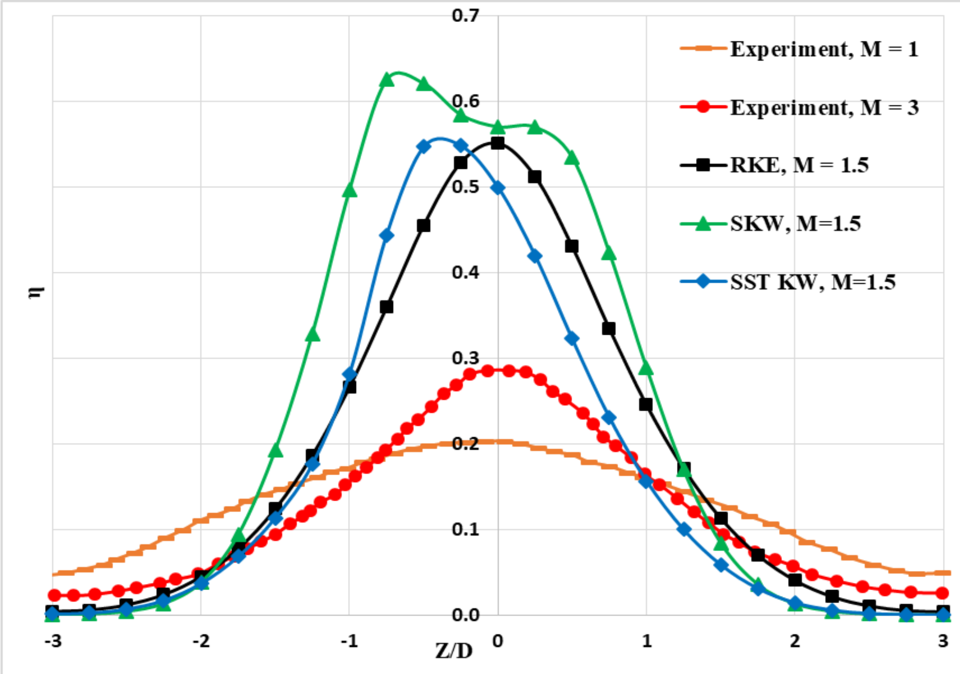

Figure 4-16: Lateral film cooling effectiveness at x/D = 30 for M = 1.5

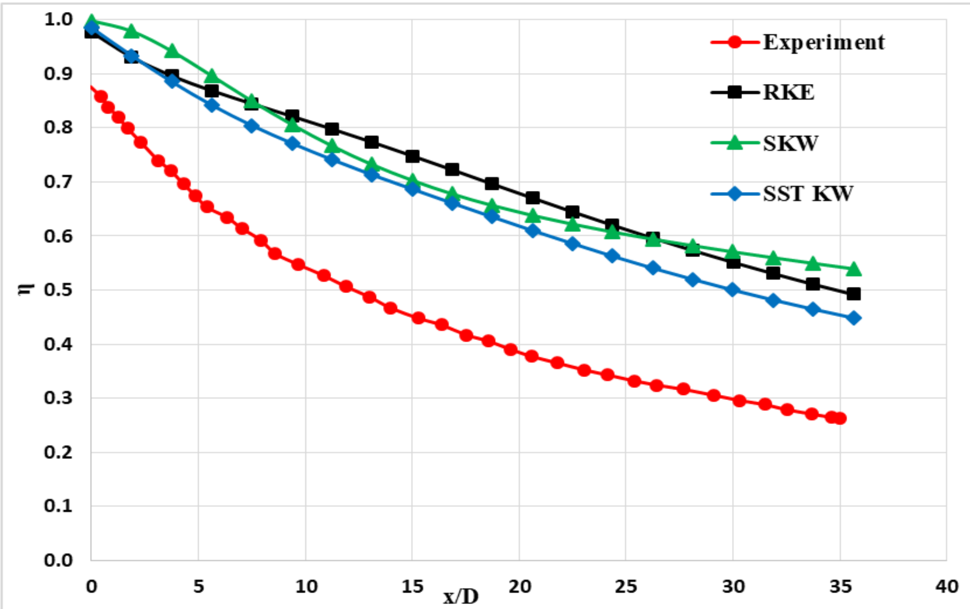

Figure 4-17: Centerline film cooling effectiveness for M = 1.5

Film cooling effectiveness variations for M = 1.5 are shown with comparisons of experimental results in Figure 4-14, Figure 4-15, Figure 4-16, and Figure 4-17. RKE model has well predicted the experimental results of laterally averaged film effectiveness. Similar symmetric pattern of the lateral effectiveness variation has been generated by RKE as shown by the experimental data while the effectiveness has over-predicted near centerline region as shown in Figure 4-15 and Figure 4-16. The over-prediction can be clearly observed in the centerline effectiveness variations as shown in Figure 4-17.

The over-prediction for centerline region cooling effectiveness may be understood by high turbulent interaction at jet-mainstream interface [75] [76] [77]. Due to the extensive turbulent thermal energy transport between mainstream and coolant flow, the core of the coolant jet emanating from the cooling hole is diluted by the mainstream hot fluid [64] [75] [76] [77]. In addition, the turbulent flow in near hole region toward centerline is essentially anisotropic since the fluctuating components of instantaneous velocities are different in different directions [64]. On the other hand, turbulent diffusivities for momentum and heat vary along the stream-wise direction in jet centerline region as well as it depends on direction [76] [77]. Due to the high turbulent transport and turbulent diffusion process, the film cooling effectiveness declines considerably in the core area of the coolant jet. Since this high turbulent flow behavior is barely captured by RANS turbulence models used in the present study, the cooling effectiveness has over-predicted in the geometric centerline region in which the core of the coolant jet more aligns and these high turbulent transport and diffusion occurs. In addition, the anisotropy of the turbulence which is not modeled by the used RANS turbulence models has contributed for the over-prediction.

4.1.2.1 Error analysis of film cooling effectiveness

Table 4-3: Error analysis of laterally averaged effectiveness

	M = 1.5			M = 3		
	RKE	**SST KW**	**SKW**	**RKE**	**SST KW**	**SKW**
Max error (%)	15.14	18.63	45.12	24.42	24.75	53.81
Min error (%)	0.24	0.61	1.01	0.42	4.24	2.59
RMSE	0.015	0.035	0.042	0.024	0.028	0.051

Table 4-4: Error analysis of centerline effectiveness

	M = 1.5			M = 3		
	RKE	**SST KW**	**SKW**	**RKE**	**SST KW**	**SKW**
Max error (%)	89.75	72.59	106.12	80.98	67.068	111.75
Min error (%)	11.41	12.57	14.16	7.073	5.87	8.26
RMSE	0.243	0.200	0.244	0.25	0.19	0.18

According to the error estimations for the laterally averaged effectiveness distributions as shown in Table 4-3, the lowest RMSE (Root Mean Square Error) has been shown by RKE model. The second has been with SST KW while the highest RMSE has been shown by SKW for both blowing ratio of M = 1.5 and 3. A significant difference in RMSE can be seen between RKE and SST KW for M = 1.5 which are 0.015 and 0.035 while no noticeable difference can be seen for higher blowing ration of M = 3, which are 0.024 and 0.028. The same behavior can be observed for the maximum error percentages values also. The lowest value for the maximum error percentage has been occurred for RKE model while the highest value has been obtained by SKW model. Based on these observation from error analysis, it can be concluded that RKE model has predicted the experimental results well compared to the other two models.

When considering the centerline effectiveness distributions as shown in Table 4-4, the maximum error percentage values are large due to the large deviation of predictions from the experimental results. These large deviation can be understood by the inability to model high turbulent diffusion and anisotropic nature in centerline region by the RANS turbulence models used.

Table 4-5: R-Square values for each turbulence model

	M = 1.5			M = 3		
	RKE	**SST KW**	**SKW**	**RKE**	**SST KW**	**SKW**
R^2 (Laterally-averaged)	0.923	0.563	0.366	0.798	0.718	0.069
R^2 (Centerline)	-0.608	-0.086	-0.618	-0.868	-0.124	0.034

According to the R-square values calculated for the laterally averaged effectiveness predictions from the each model as shown in Table 4-5, the highest R^2 values, which are 0.923 and 0.798 near to 1, have been obtained by RKE model for M = 1.5 and 3 both. It has shown the suitability of RKE model to be used in predicting laterally averaged effectiveness. However the negative R^2 values for centerline effectiveness have been shown poor for predictions of the experimental values. This is due to the large over-prediction in centerline effectiveness.

4.1.3 Comparison with LES results

Figure 4-18, Figure 4-19, Figure 4-20, Figure 4-21 have shown comparisons among experimental results, LES results and the results of three selected RANS turbulence models of the present study. The experimental and LES results were extracted from Tracy, et al. [64]. Those results have been generated for DR = 1.2 with D = 6.78 mm using large eddy simulations (LES). The LES simulation has been run in Ansys Fluent V18.2 using Wall-Adapting Local Eddy-Viscosity (WALE) subgrid-scale turbulence model. As shown in Figure 4-18, the results from the all RANS turbulence models have shown similar shape of cooling effectiveness variation in comparison to LES results at x/D = 0 for M = 3 while the deviation of RANS results from LES is not significant for all RANS models although the near-centerline region has shown considerable difference.

When moving downstream of x/D = 10, significant difference can be observed in the results of SKW and SST KE in comparison to LES results while RKE model has maintained symmetric shape of the cooling effectiveness variation as well as well-predicted the off-centerline region. Due to inability of the RANS models to capture the high turbulent transport and anisotropic nature in the core of the coolant jet in the cross flow, cooling effectiveness in the centerline region has over-predicted. SKW and SST KW have shown the same over-prediction as well as a bimodal distribution of cooling effectiveness which was not shown in experimental and LES results. LES has been predicted centerline region well compared to the RANS turbulence models. It can be concluded that LES has been well-modeled the effect of high turbulent transport and anisotropy in the coolant jet core when compared to the RANS models.

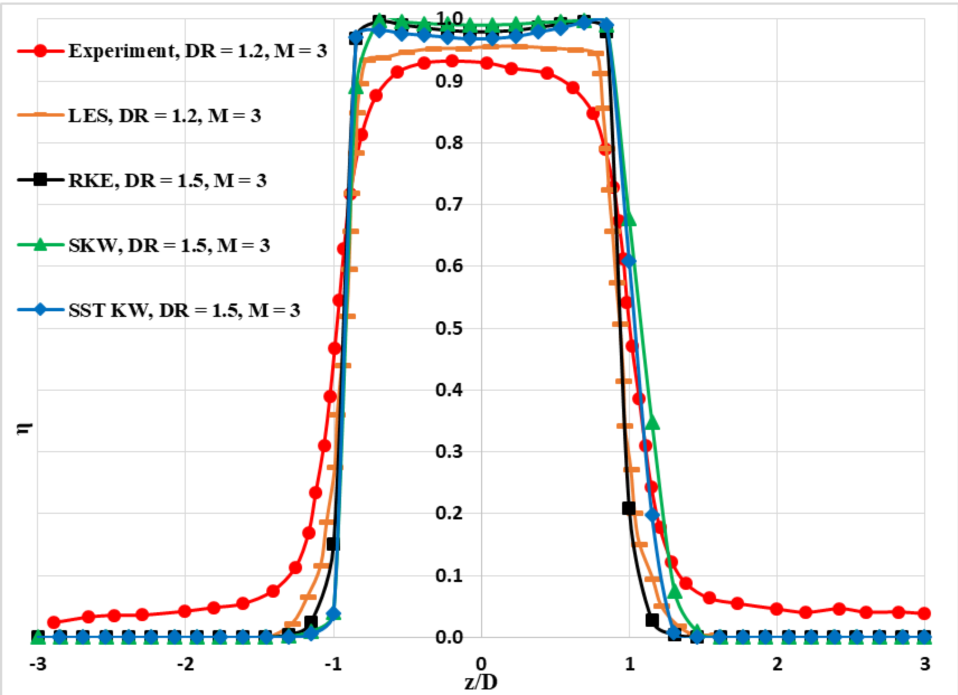

Figure 4-18: Local film cooling effectiveness in lateral direction at x/D = 0 for M = 3

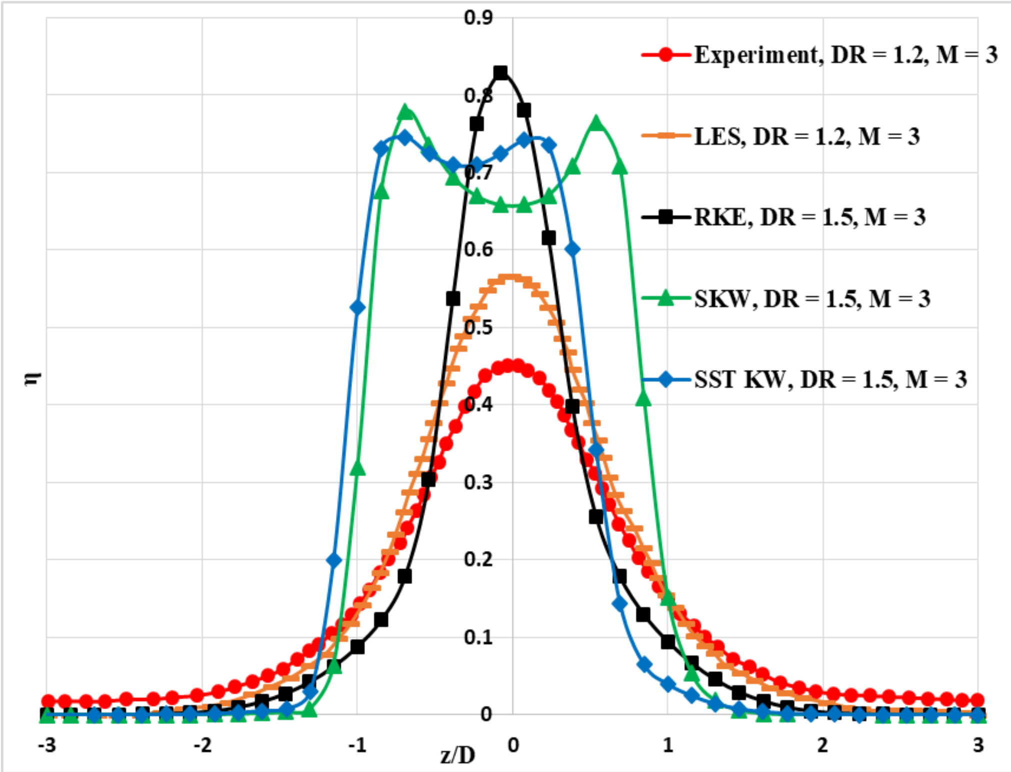

Figure 4-19: Local film cooling effectiveness in lateral direction at x/D = 10 for M = 3

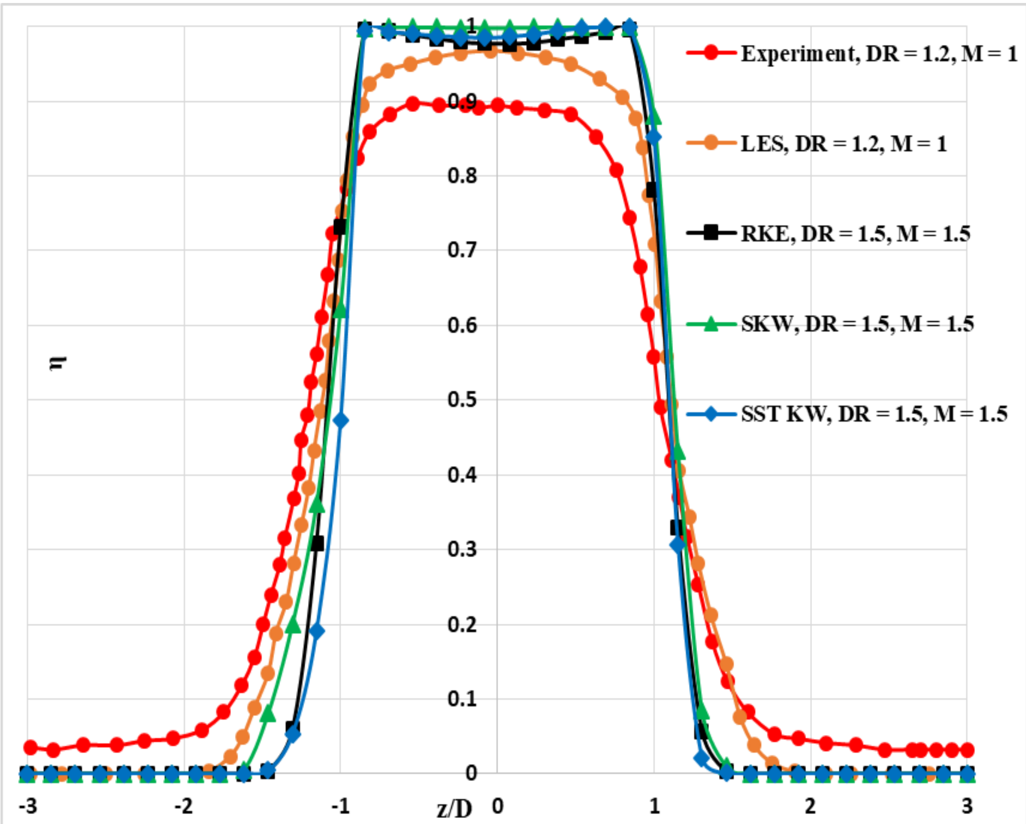

Figure 4-20: Local film cooling effectiveness in lateral direction at x/D = 0

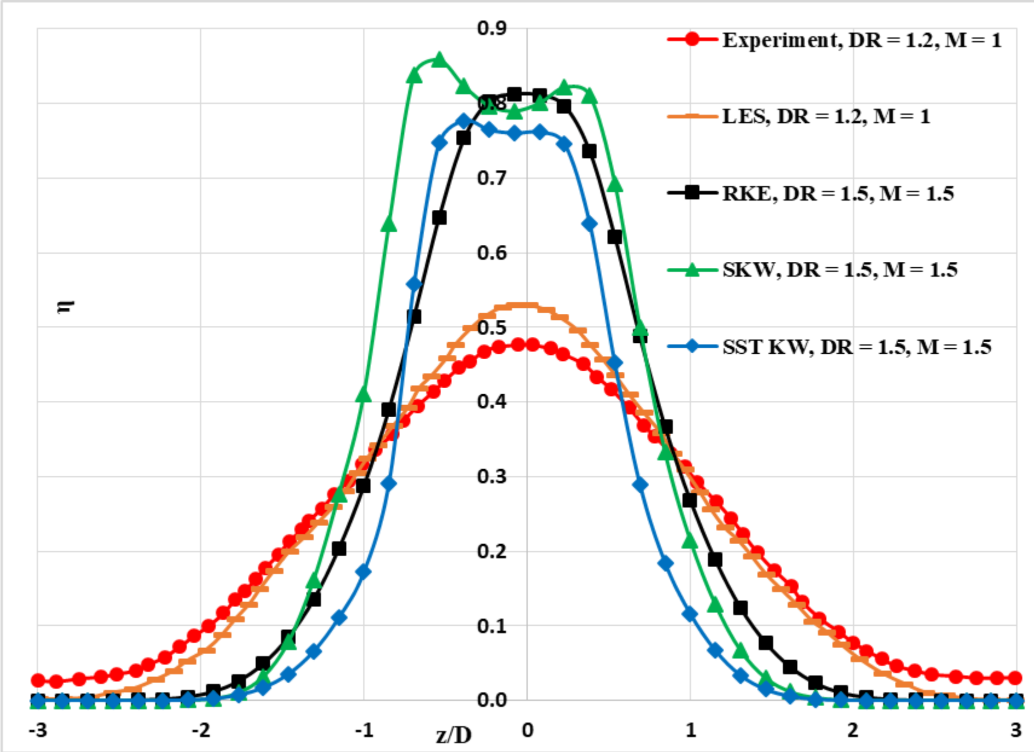

Figure 4-21: Local film cooling effectiveness in lateral direction at x/D = 10

Figure 4-20, Figure 4-21 have shown experimental and LES results for DR = 1.2 and M = 1 while RANS models' results have shown for DR = 1.5 and M = 1.5. As shown in Figure 4-20, this comparison also has shown similar behavior as explained under Figure 4-18. Figure 4-21 has shown bimodal pattern from SKW while SST KW has presented very small bimodal pattern. RKE has maintained symmetric effectiveness distribution compared to LES and experimental results. However, all RANS turbulence models have over-predicted in the centerline region as explained previously. In conclusion, RKE model was identified as the best turbulence model over the three models after performing above detailed validation.

4.2 Cooling performance of shaped hole with trench

In this study, cooling performance of 7-7-7 shaped hole were studied with a trench at the injection of the hole. Cooling performance of cylindrical hole shape with a trench has been studied in many research but no studies can be found about the effects of trench on the shaped holes. Three different slot heights of h/D = 0.25, 0.5 and 1 were used in the study. Each slots has the same width similar to the width of hole exit dimensions. Three different blowing ratios of 1.5, 3, and 5 were used at a fixed slot depth. The case of h/D = 0 in each plot represents the baseline case without trench, which can be used to compare the cooling performance of trenched cases. Figure 4-22, Figure 4-23, Figure 4-24, and Figure 4-25 present laterally averaged adiabatic film cooling effectiveness at fixed slot depths with varying blowing ratio.

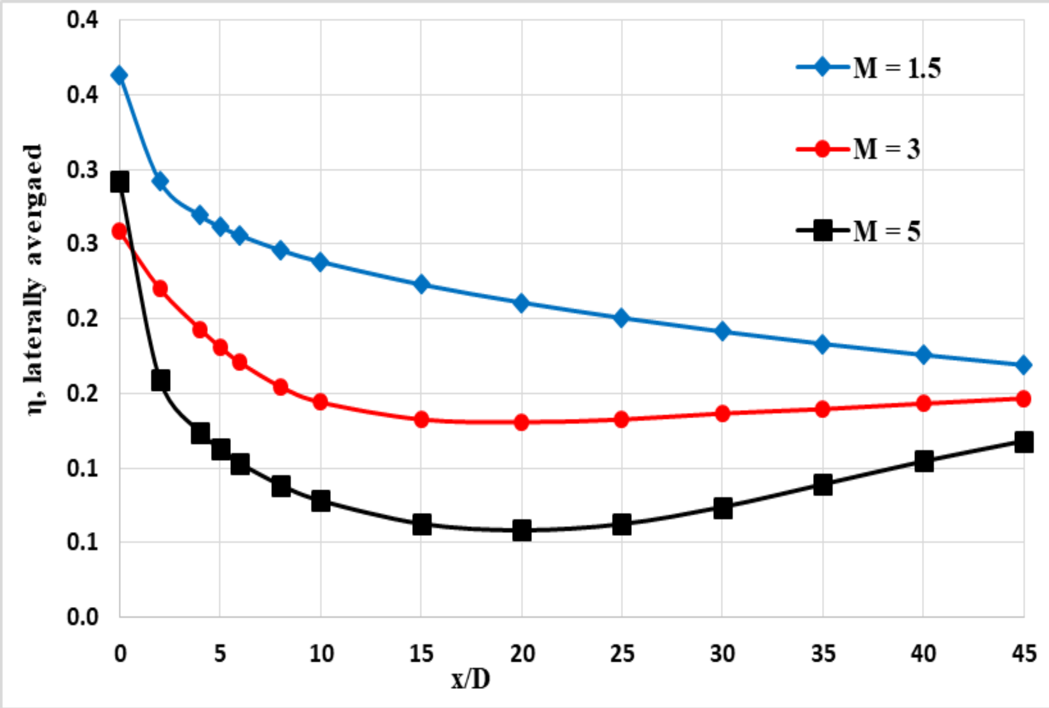

Figure 4-22: Laterally averaged effectiveness of h/D = 0

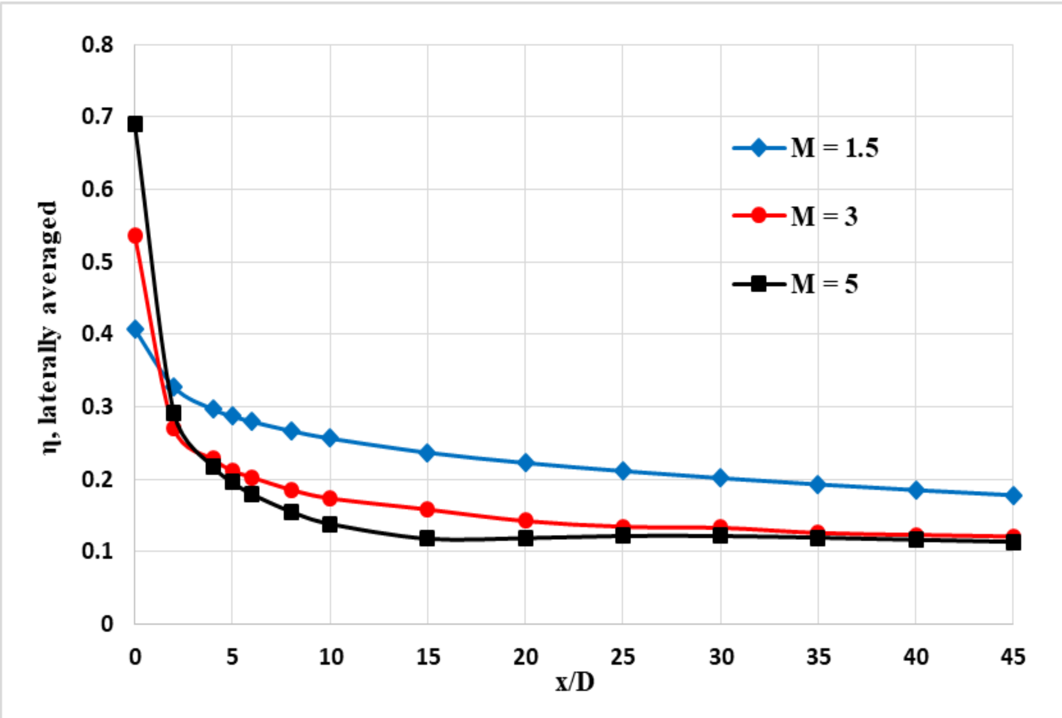

Figure 4-23: Laterally averaged effectiveness of h/D = 0.25

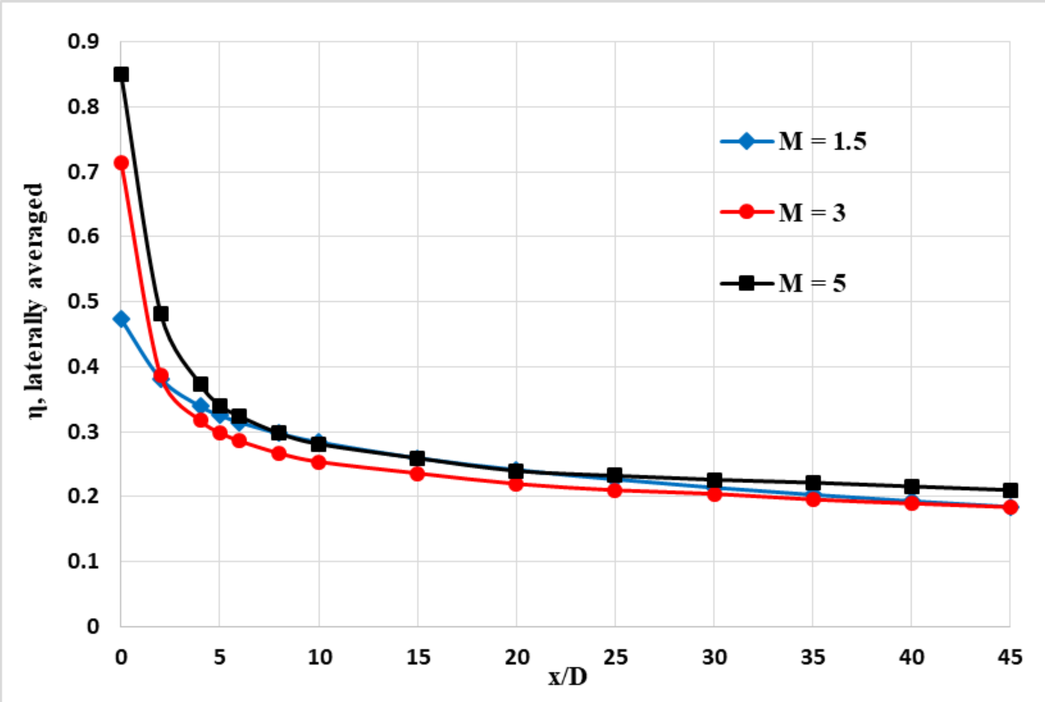

Figure 4-24: Laterally averaged effectiveness of h/D = 0.5

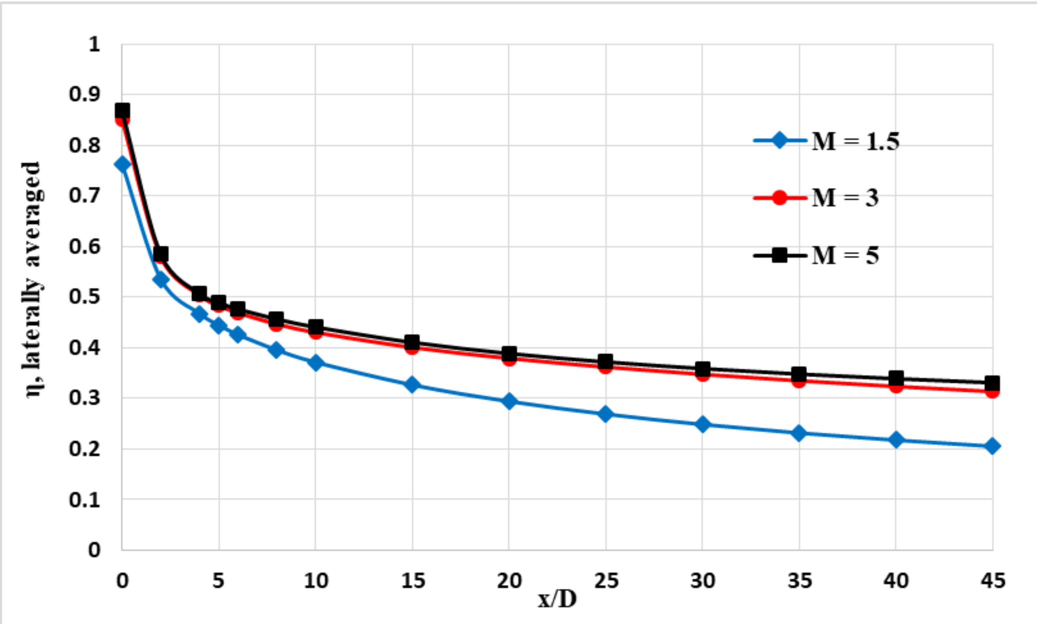

Figure 4-25: Laterally averaged effectiveness of h/D = 1

As shown in Figure 4-25, laterally averaged film cooling effectiveness is not distinct at higher blowing ratio with higher slot depth of h/D = 1 while at a fixed higher slot depth ratio such as h/D = 0.5, 1, the film cooling effectiveness increases when increasing the blowing ratio. As shown in Figure 4-24, difference between downstream film cooling effectiveness values at three blowing ratios of 1.5, 3 and 5 is insignificant while at lower slot depth, h/D = 0.5, a noticeable difference in the film effectiveness can be observed near the hole exit. However at h/D = 0 (or baseline case) film effectiveness values have shown significant difference among the blowing ratios as shown in Figure 4-22. The highest effectiveness has been shown at lower blowing ratio of 1.5 as shown by Figure 4-23 while the same behavior has maintained in the baseline case. Laterally averaged film cooling effectiveness has shown noticeably high at higher blowing ratios when increasing slot depth. A plateau can be seen at h/D = 1 when increasing blowing ratio as depicted by Figure 4-25. Centerline adiabatic film cooling effectiveness has shown the similar behavior in 7-7-7 shaped hole without a transverse slot [24]. This plateau has positive sides to the design of high performance film cooling systems. Due to the insensitivity, the coolant flow rate can be reduced in the actual designs when using the lowest possible blowing ratios in the plateau. Predictions of the film cooling effectiveness in the region might be made without considering the parameter of blowing ratio. When designing shaped film holes with exit transverse slot, higher blowing ratios at higher slot depth ratios have shown higher cooling performance. It was observed that maintaining higher blowing ratios at lower slot depth ratios is only a waste of coolant without improvements to cooling performance.

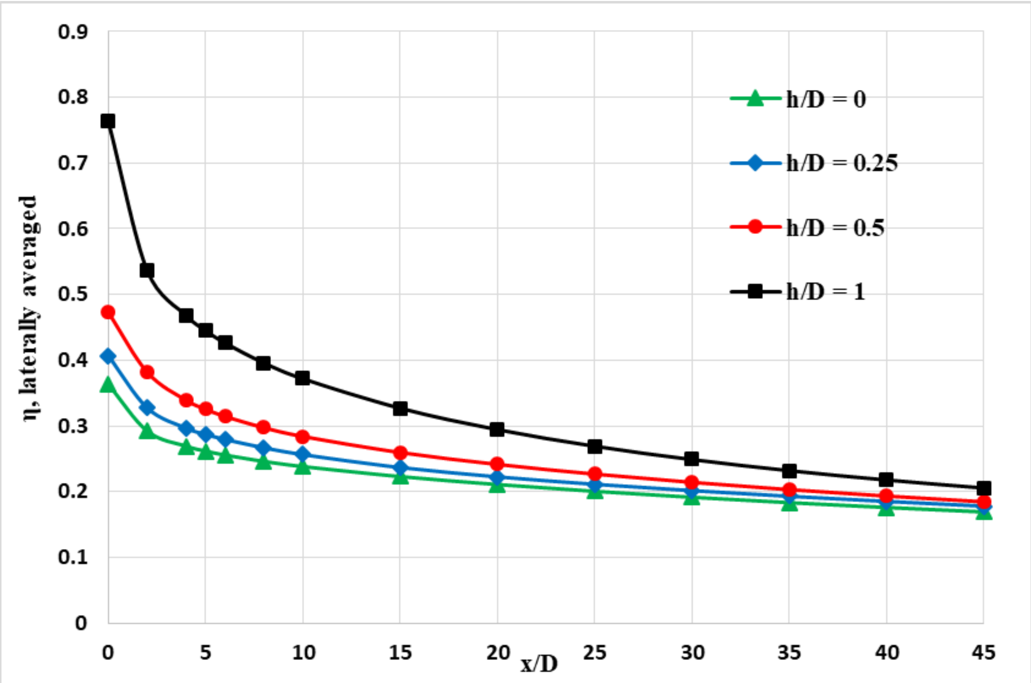

Figure 4-26: Laterally averaged effectiveness of M = 1.5

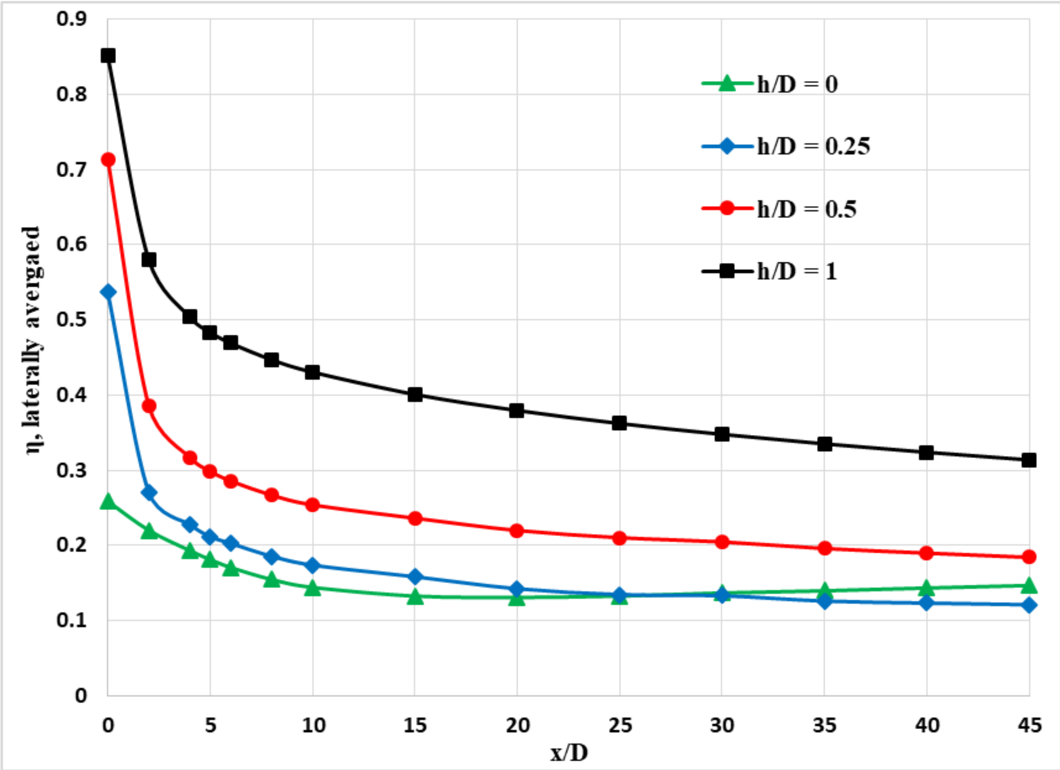

Figure 4-27: Laterally averaged effectiveness of M = 3

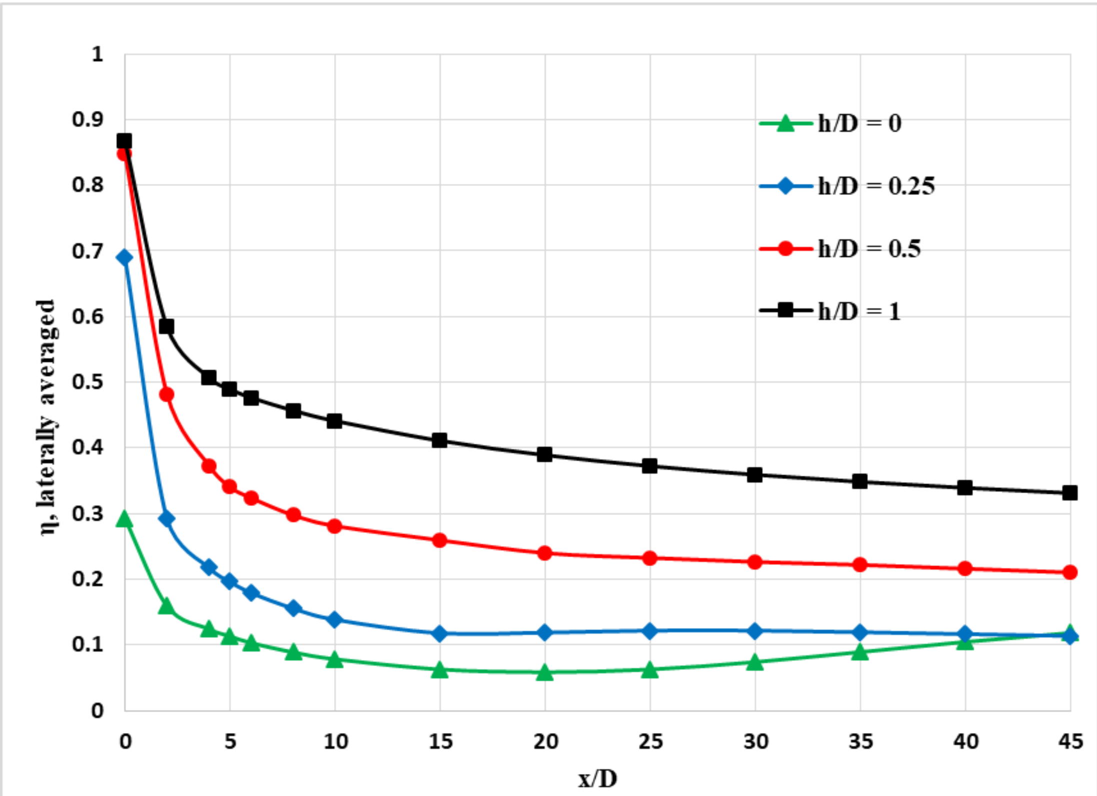

Figure 4-28: Laterally averaged effectiveness of M = 5

Variation of laterally averaged adiabatic film cooling effectiveness has been illustrated by Figure 4-26, Figure 4-27, and Figure 4-28 at fixed blowing ratios with varying slot depth ratios. At the fixed blowing ratio, laterally averaged effectiveness increases when increasing the slot depth ratio. When increasing the blowing ratio, the difference between effectiveness values associated with different depths increases as depicted by Figure 4-26, Figure 4-27, Figure 4-28. According to Figure 4-26, Figure 4-27, and Figure 4-28, the cooling effectiveness has been improved by higher slot depths at all blowing ratios relative to the baseline case. The difference between effectiveness values at various slot depths near the hole exit has reduced when increasing blowing ratio while, as a result of strong lateral spreading, the downstream difference is significant at higher blowing ratios when increasing slot depth.

The decay of the laterally averaged effectiveness in hole exit region is steeper at higher blowing ratio of M = 5 when reducing the slot depth as shown in Figure 4-28. The decay can be attributed to the jet penetration into mainstream at higher blowing ratios. Hot mainstream is drawn to the region under the coolant jet due to the penetration thereby reducing cooling effectiveness drastically in immediate downstream of the hole exit. In general it can be expected the jet penetration at higher blowing ratios and low slot depth ratios and degradation of the cooling performance.

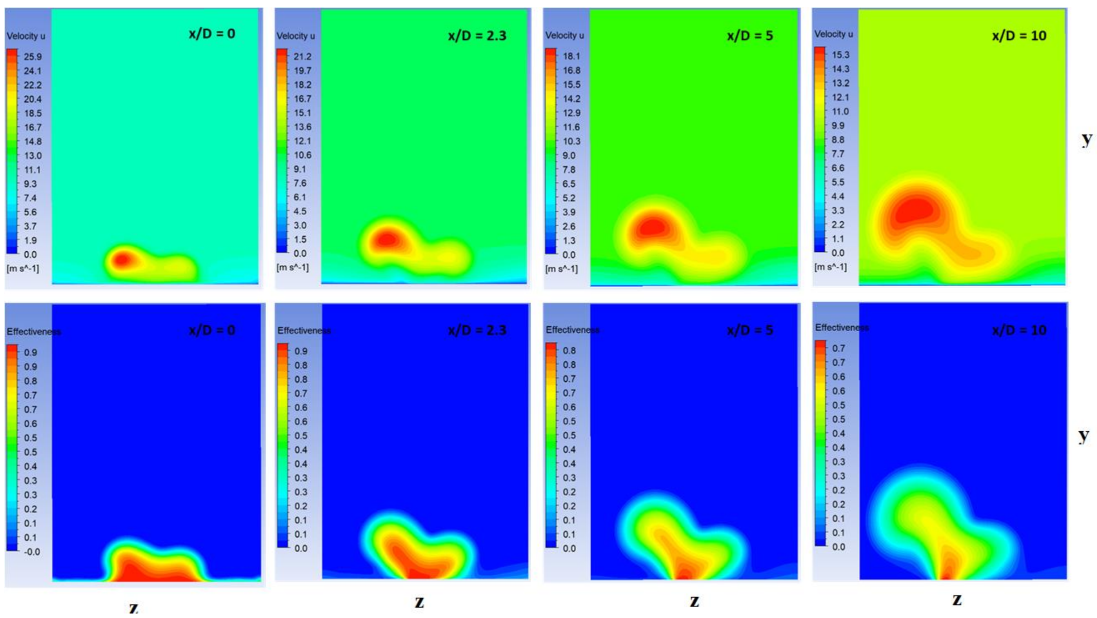

Figure 4-29: Streamwise velocity and cooling effectiveness for M = 5 and h/D = 0.25 at different streemwise locations

Streamwise velocity and cooling effectiveness distributions have been depicted at different streamwise locations of x/D = 0, 2.3, 5 and 10 as shown in Figure 4-29. When moving towards downstream, the coolant jet has lifted the surface off as shown in velocity plots in Figure 4-29. This lift of the coolant flow at the given downstream locations of x/D = 0, 2.3, 5 and 10 represents the jet penetration into the mainstream at higher blowing ratios with low trench depth ratios. Due to the jet penetration, the coolant flow contacts weakly with the surface as in Figure 4-29 whereby steeper decay in near hole region can be observed in laterally averaged film cooling effectiveness in streamwise direction.

A considerable decay in laterally averaged effectiveness was observed at low blowing ratio of M = 1.5 when increasing the sloth depth as shown in Figure 4-26. The decay at low blowing ratio is explained by the ingestion of mainstream into the coolant flow with low momentum, which reduces coolant concentration in the diffuser outlet. The jet momentum decreases furthermore with higher slot depth thereby leading to more mainstream ingestion and reducing laterally averaged cooling effectiveness.

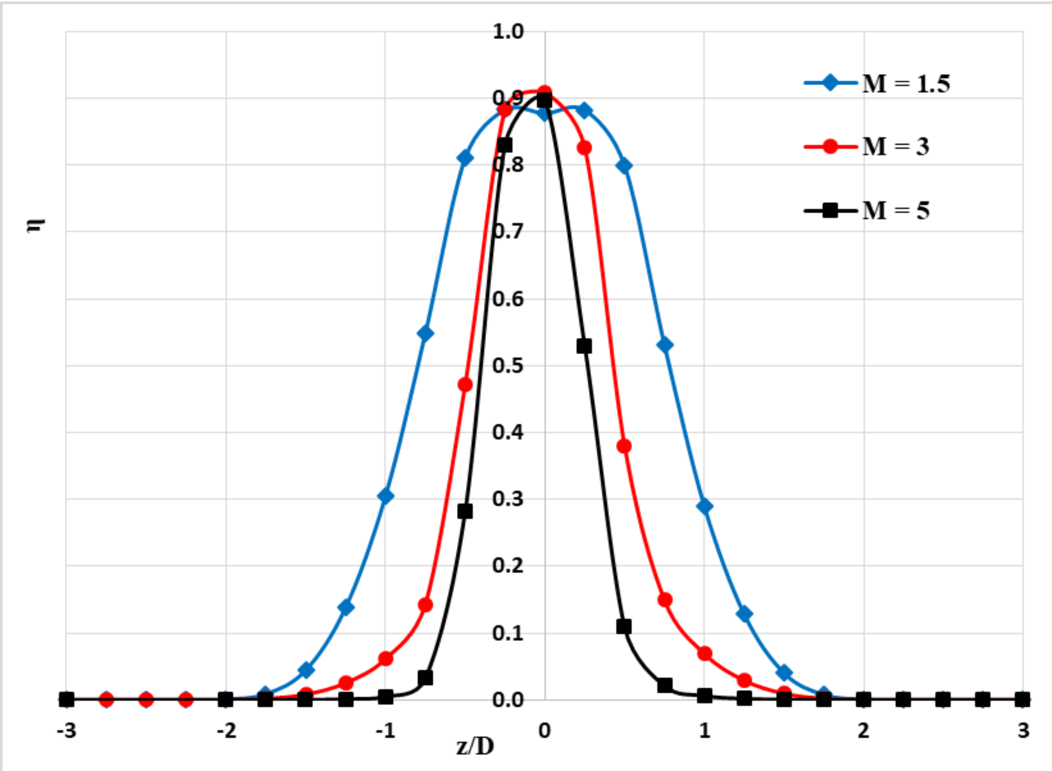

Figure 4-30: Local effectiveness in lateral direction, h/D = 0 at x/D = 5

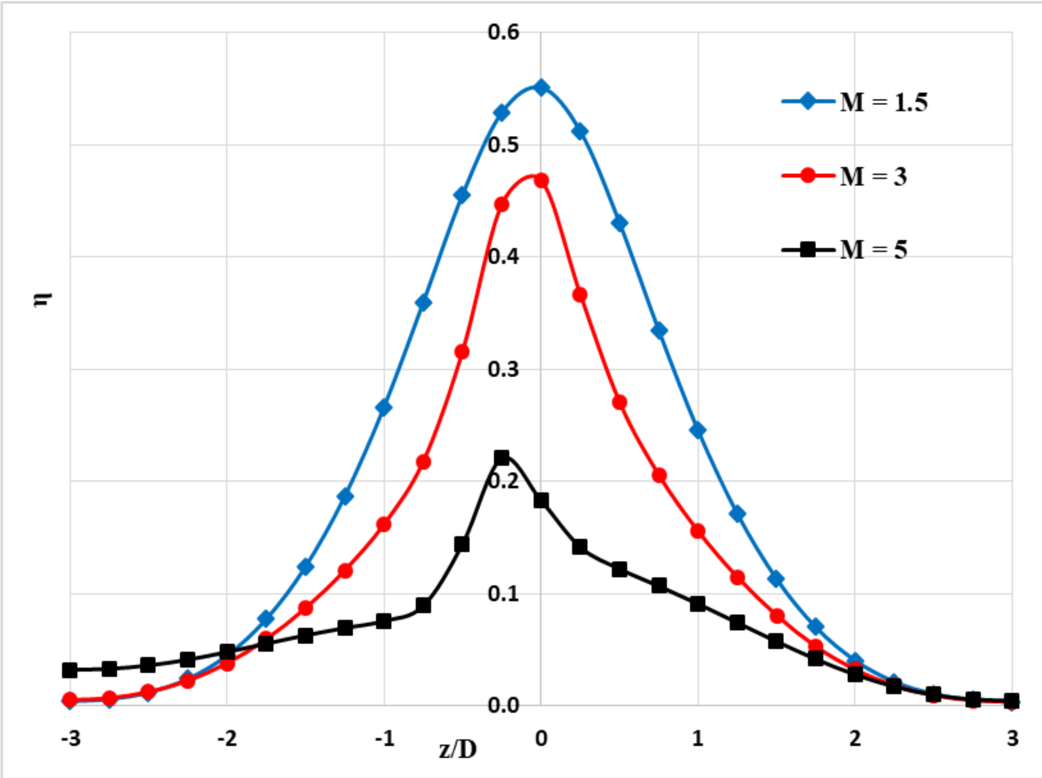

Figure 4-31: Local effectiveness in lateral direction, h/D = 0 at x/D = 30

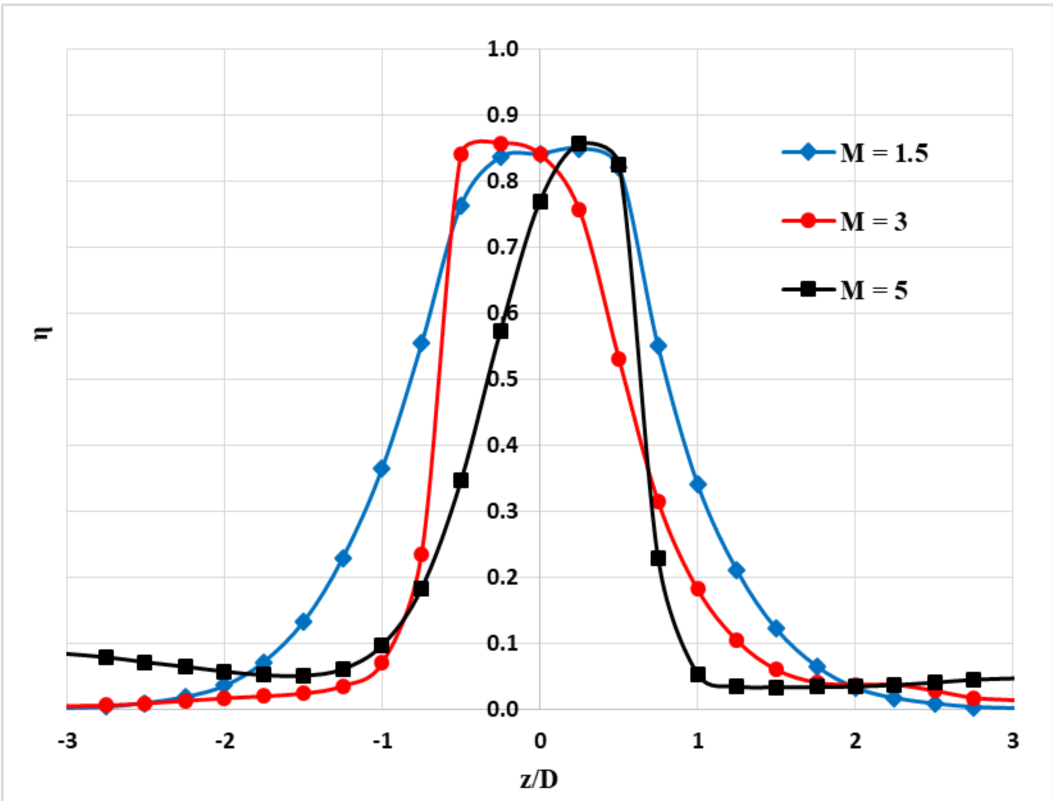

Figure 4-32: Local effectiveness in lateral direction, h/D = 0.25 at x/D = 5

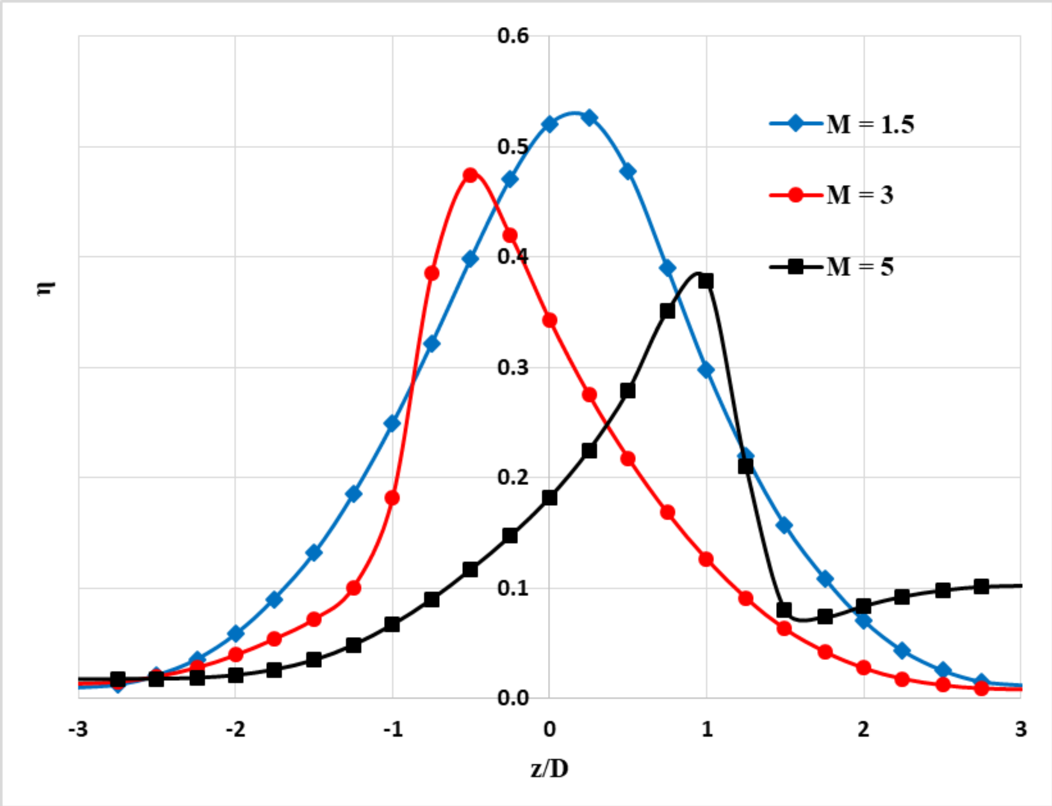

Figure 4-33: Local effectiveness in lateral direction, h/D = 0.25 at x/D = 30

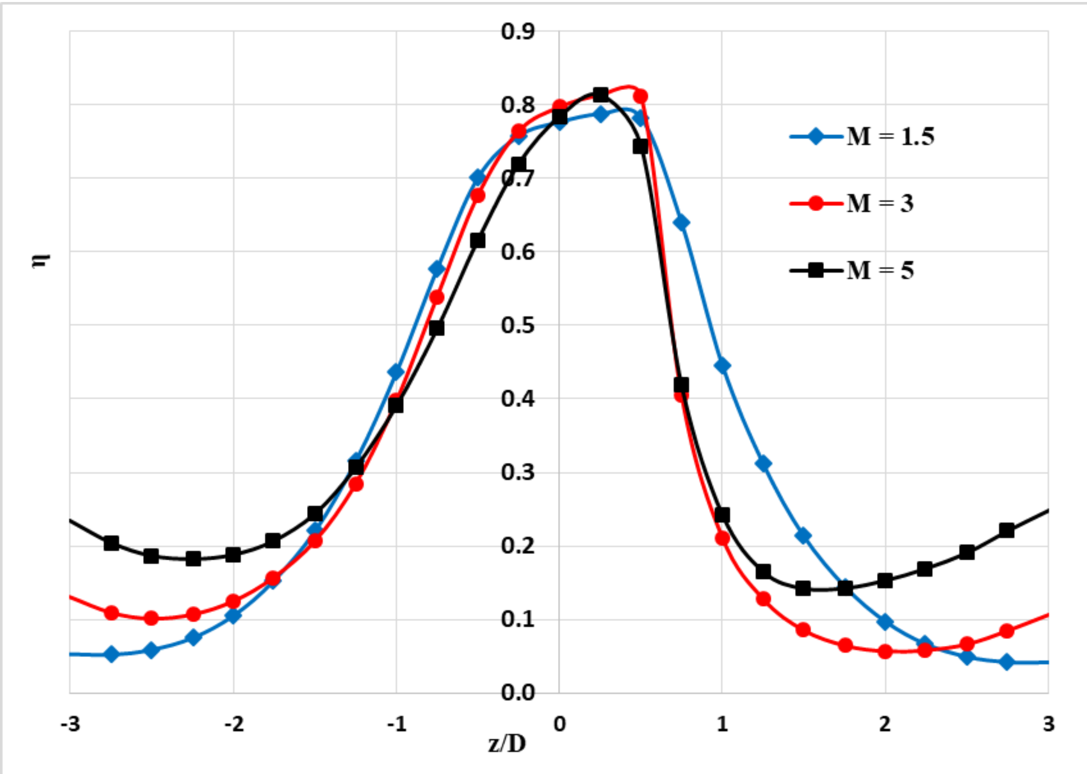

Figure 4-34: Local effectiveness in lateral direction, h/D = 0.5 at x/D = 5

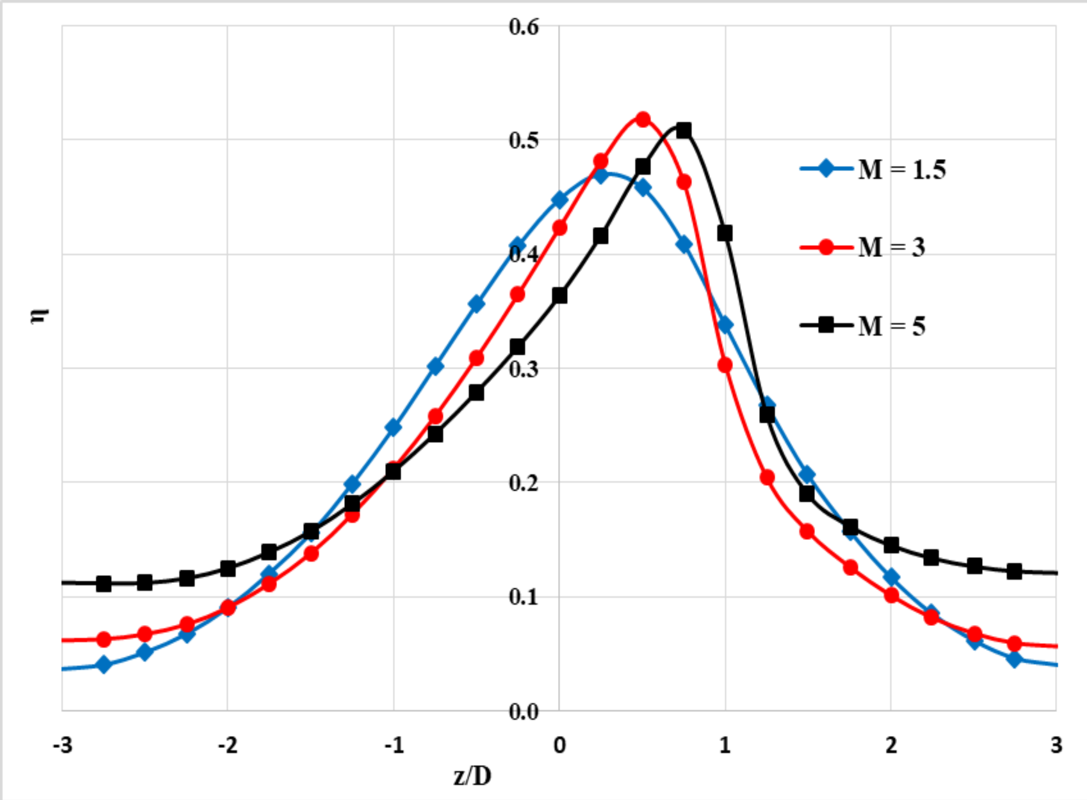

Figure 4-35: Local effectiveness in lateral direction, h/D = 0.5 at x/D = 30

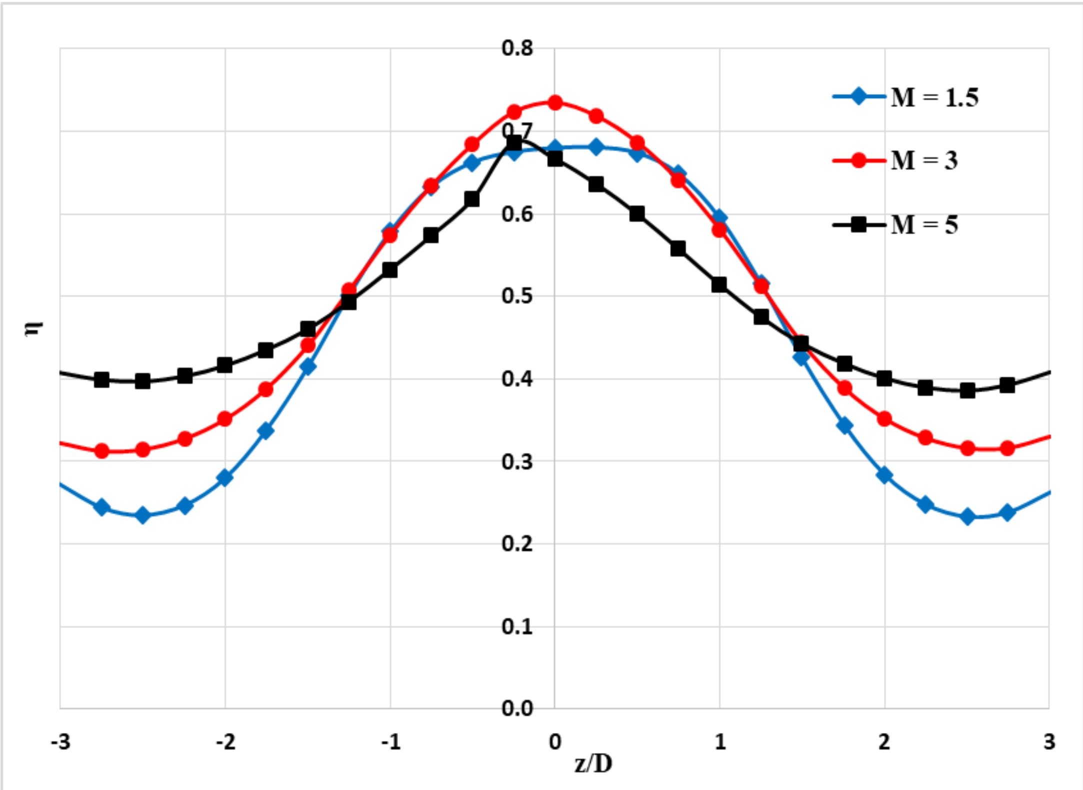

Figure 4-36: Local effectiveness in lateral direction, h/D = 1 at x/D = 5

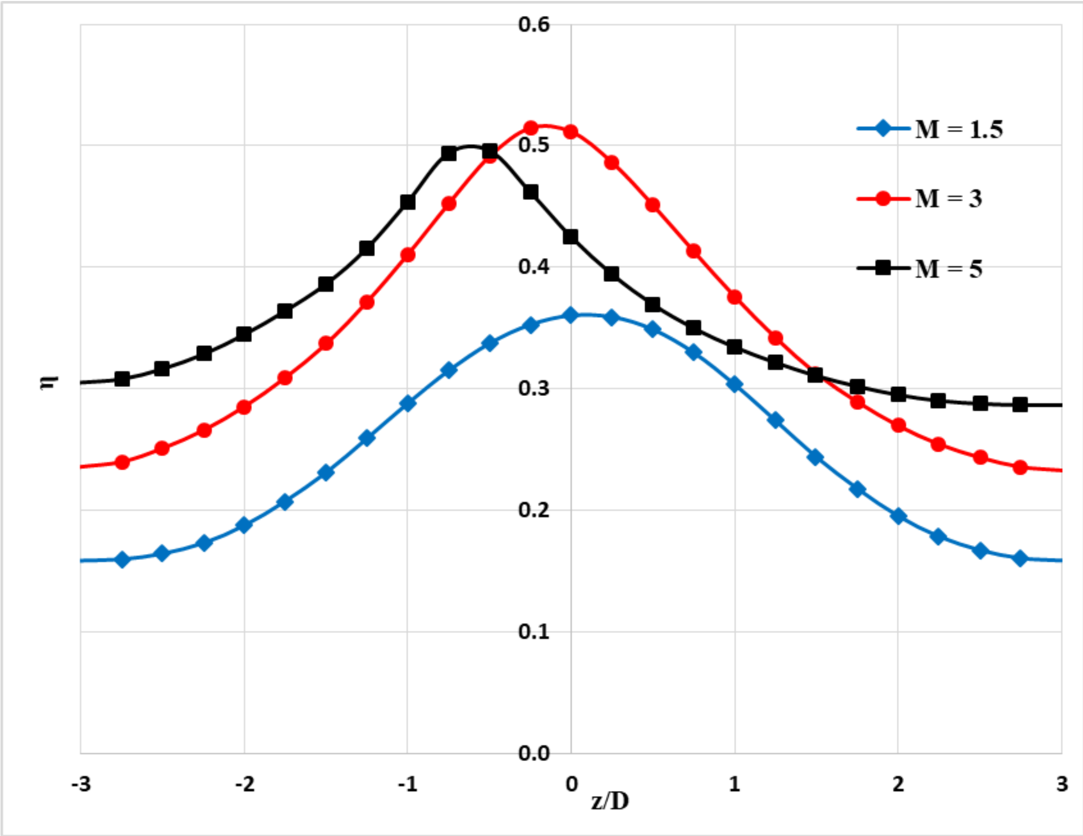

Figure 4-37: Local effectiveness in lateral direction, h/D = 1 at x/D = 30

Considering fixed slot depths, Figure 4-32, Figure 4-33, Figure 4-34, Figure 4-35, Figure 4-36, and Figure 4-37 have drawn the variation of local adiabatic film cooling effectiveness in lateral direction while that variation for baseline case has shown in Figure 4-30 and Figure 4-31. The baseline case has maintained a symmetric pattern of the effectiveness at low blowing ratios while it has shown some jet skewness at M = 5 in the downstream. At h/D = 0.25, the lateral spreading at M = 1.5 is higher than that of other blowing ratios. No significant difference can be observed in the film cooling effectiveness at h/D = 0.5 and 1 under M = 1.5, 3 and 5 as shown in Figure 4-34, and Figure 4-35. In consequence, the lateral spreading and cooling effectiveness variation are insensitive to blowing ratios. At h/D = 0.25, the cooling performance at M = 1.5 is slightly better than the other two blowing ratios. At h/D = 1, higher cooling effectiveness in off-centerline region is observed at M = 5 relative to the other two blowing ratios while the effectiveness at M = 3 has shown better cooling performance in near centerline region. Figure 4-38, Figure 4-39, Figure 4-40, Figure 4-41, Figure 4-42, and Figure 4-43 show the variations of lateral film cooling effectiveness when changing the slot depth at fixed blowing ratios.

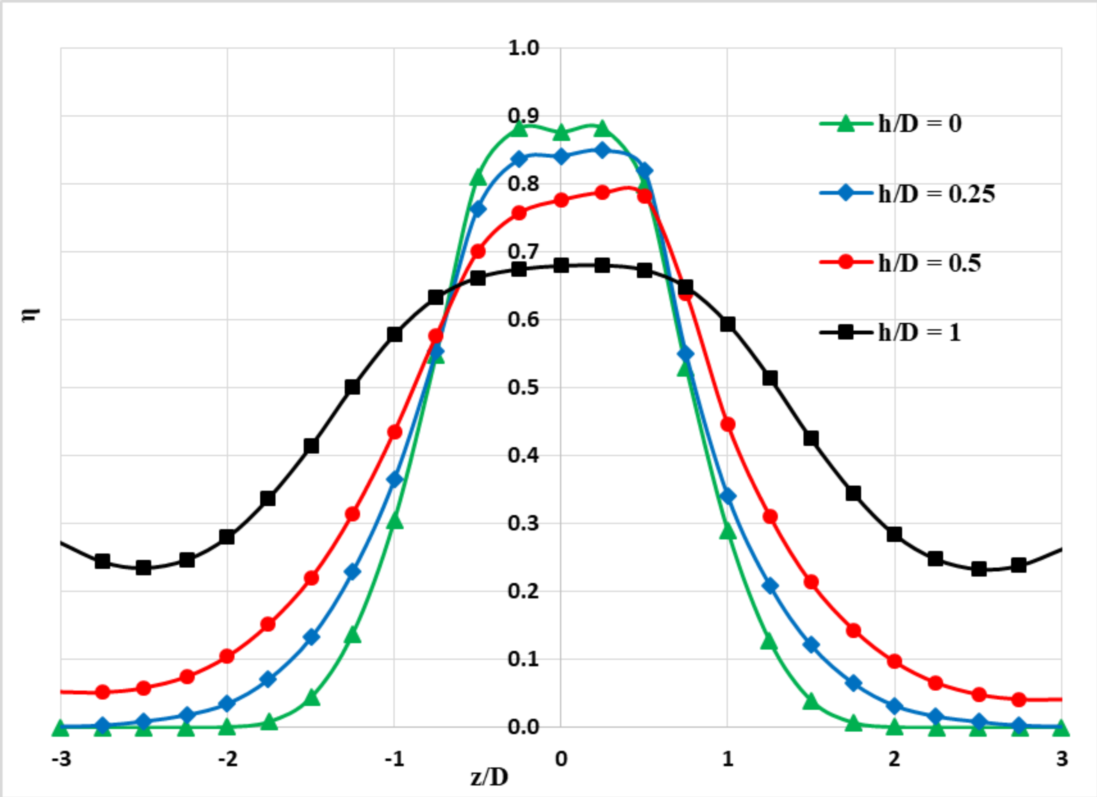

Figure 4-38: Local effectiveness in lateral direction, M = 1.5 at x/D = 5

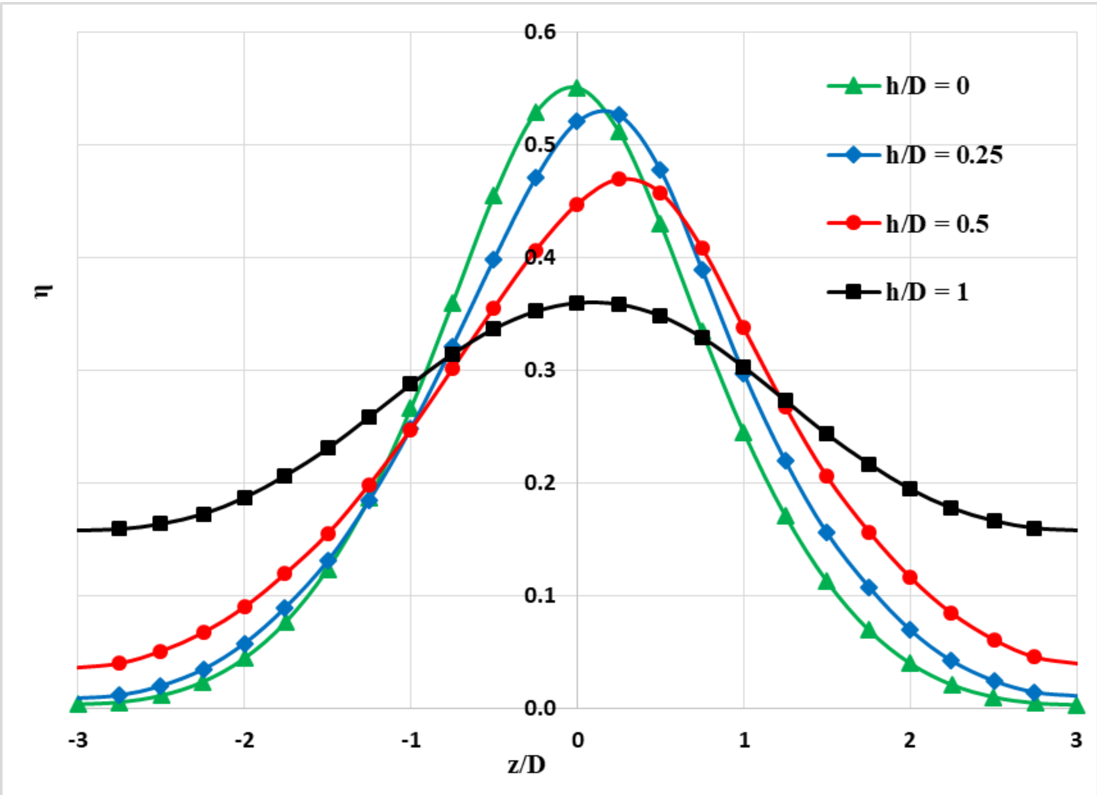

Figure 4-39: Local effectiveness in lateral direction, M = 1.5 at x/D = 30

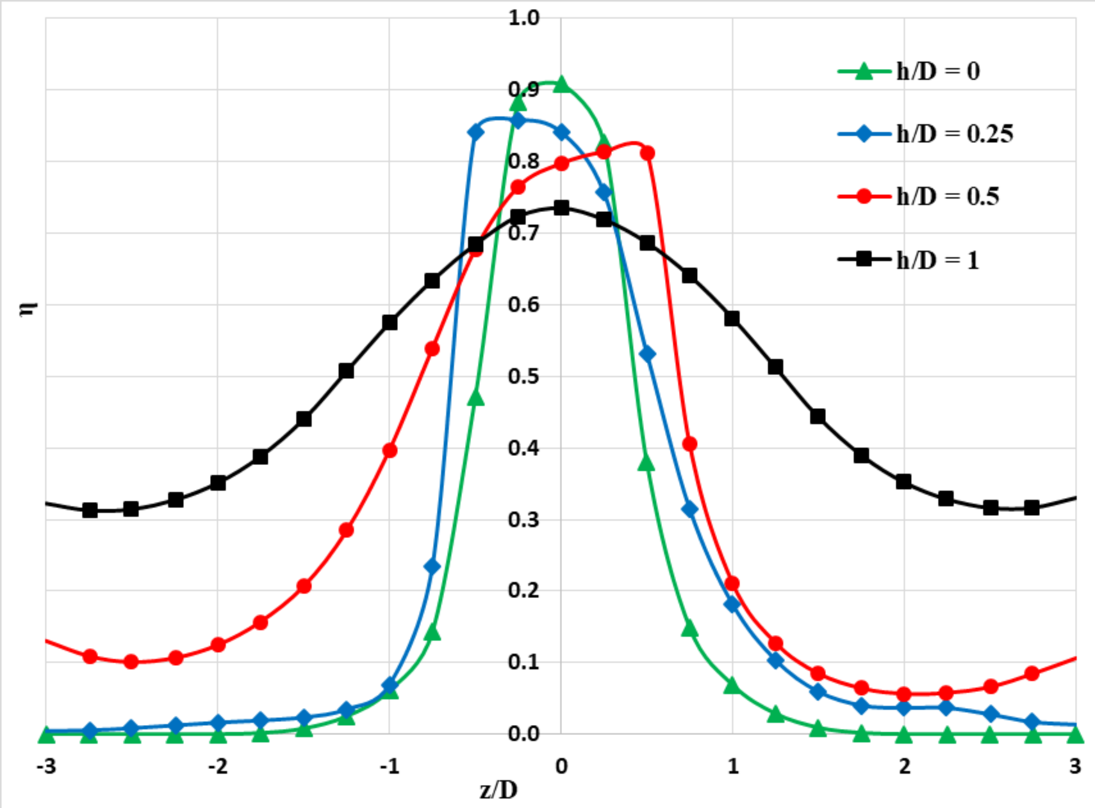

Figure 4-40: Local effectiveness in lateral direction, M = 3 at x/D = 5

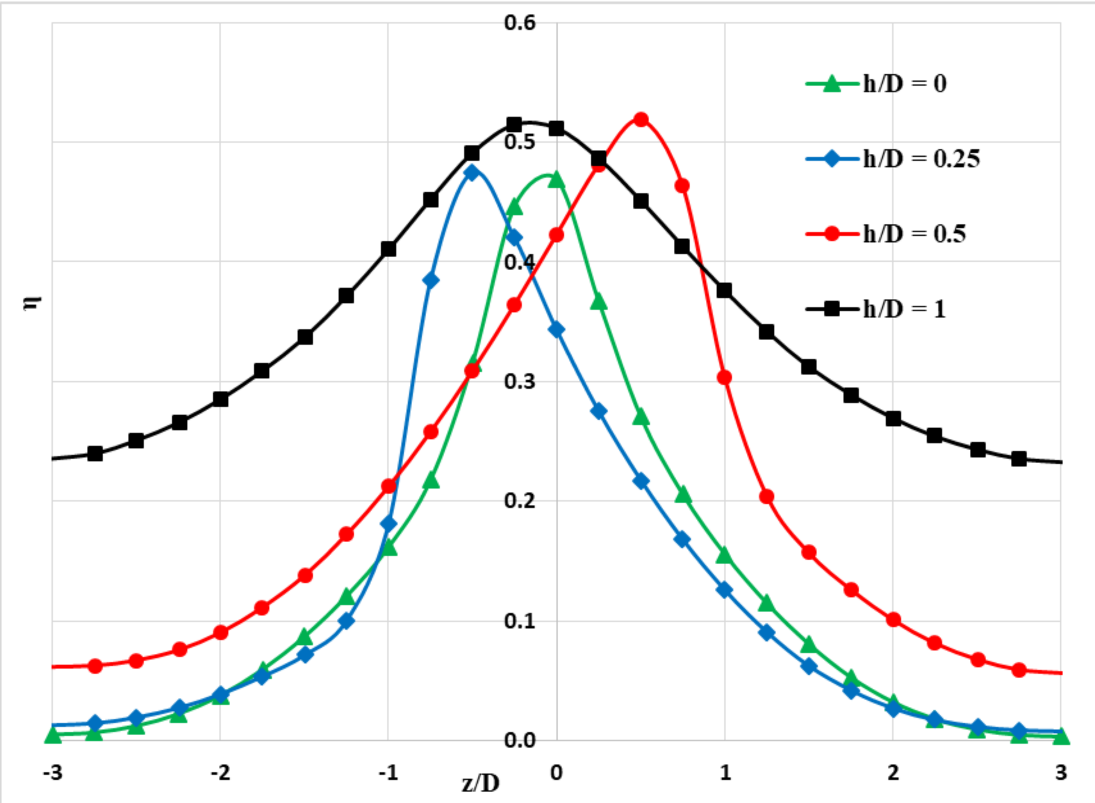

Figure 4-41: Local effectiveness in lateral direction, M = 3 at x/D = 30

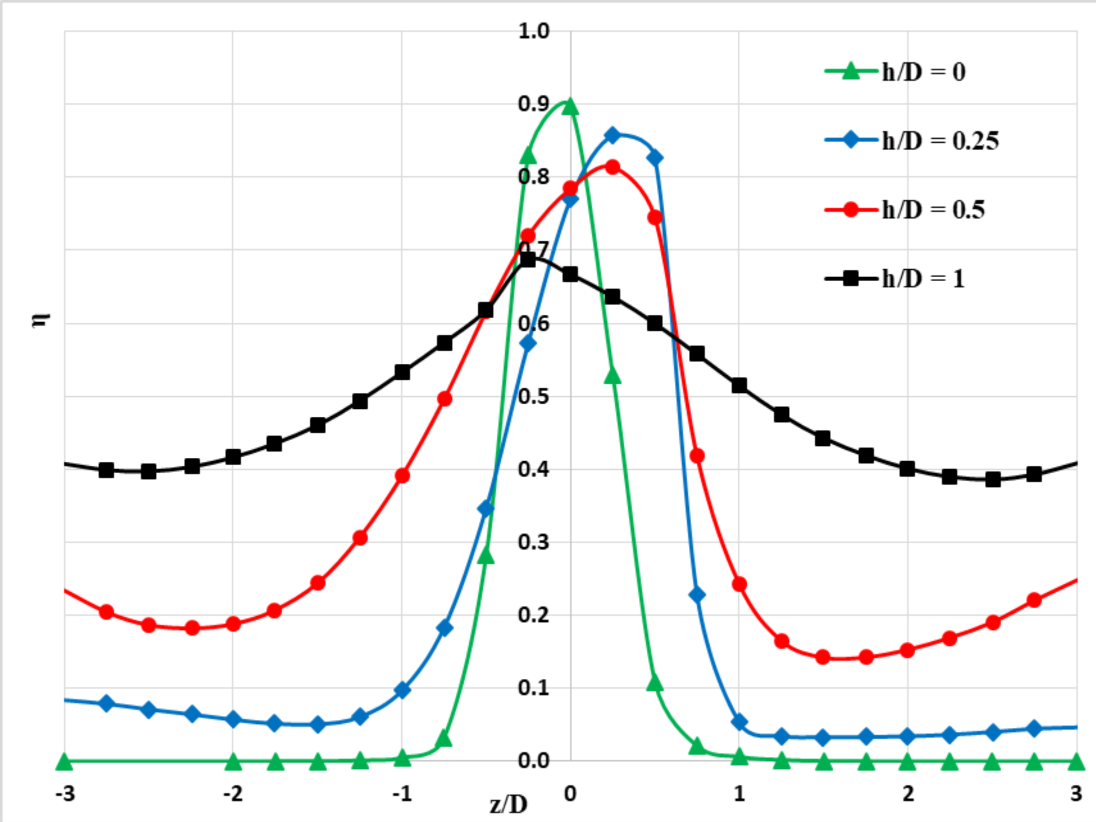

Figure 4-42: Local effectiveness in lateral direction, M = 5 at x/D = 5

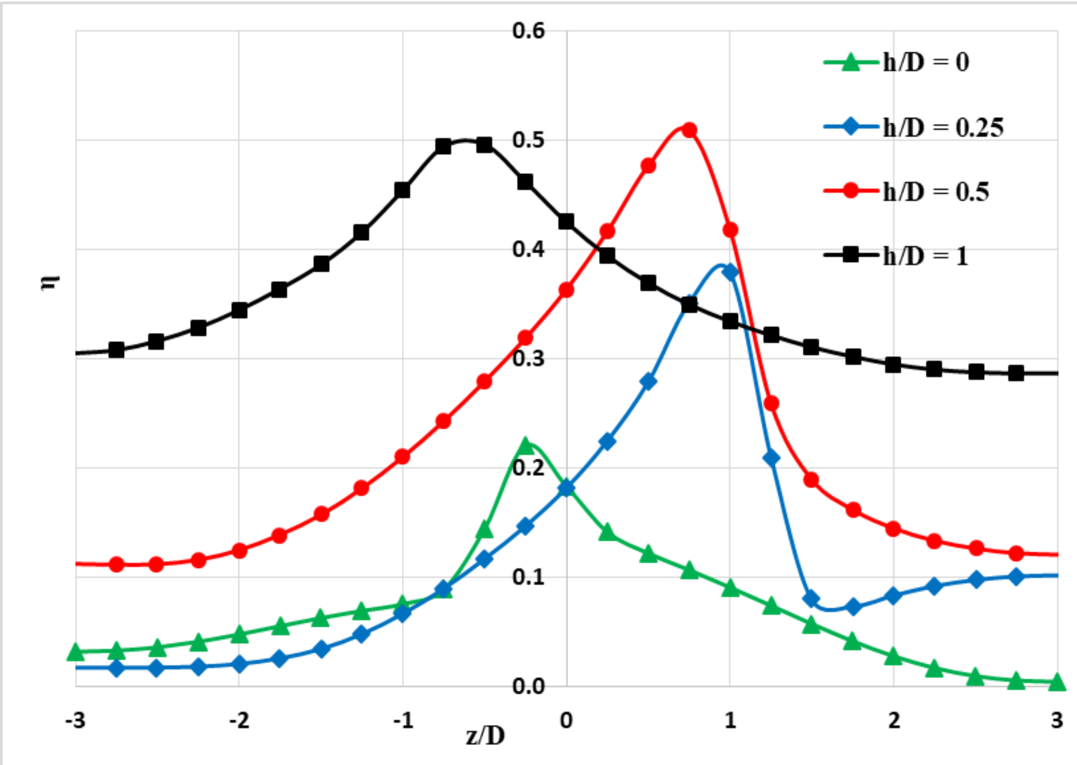

Figure 4-43: Local effectiveness in lateral direction, M = 5 at x/D = 30

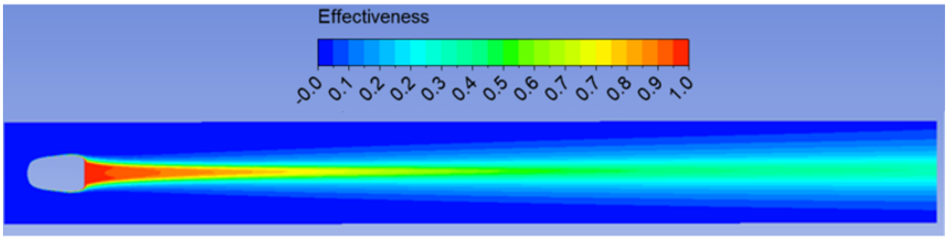

(a) h/D = 0

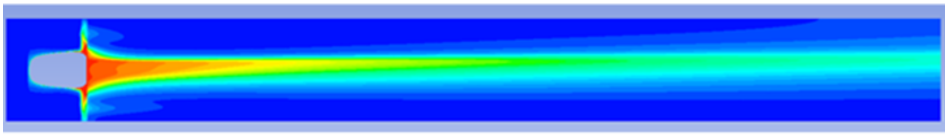

(b) h/D = 0.25

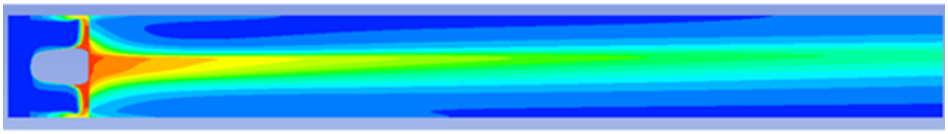

(c) h/D = 0.5

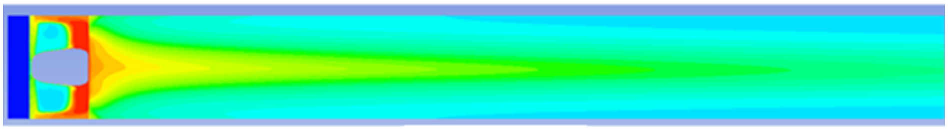

(d) h/D = 1

Figure 4-44: Local effectiveness contours of M = 3 at various slot depths

At M = 3, the coolant jet has started to skew at h/D = 0.25 and 0.5 while it is symmetric about the centerline at M = 1.5. At M= 5 and h/D = 1, the jet has shown considerable skewness relative to the geometric centerline. The skewness at M = 5 is larger than that of the other two blowing ratios. This skewness has become larger when moving to the downstream. In general, it can be concluded that the jet shows skewness relative to geometric centerline at higher blowing ratios and lower slot depths while the skewness becomes invisible at lower blowing ratios and lower slot depths. Although the jet issuing at higher blowing ratios and higher slot depths shows little skewness, it shows superior coolant spreading in lateral direction compared to other cases. A better lateral spreading has shown at h/D = 1 for each blowing ratios. The coolant jet has shown noticeable skeweness at low depth ratios of the trench at higher blowing ratios as shown in Figure 4-44 and Figure 4-53. It has not shown a significant skeweness of the jet for the baseline case, which is h/D = 0, as shown in Figure 4-38, Figure 4-39, Figure 4-40, Figure 4-41, Figure 4-42 and Figure 4-43.

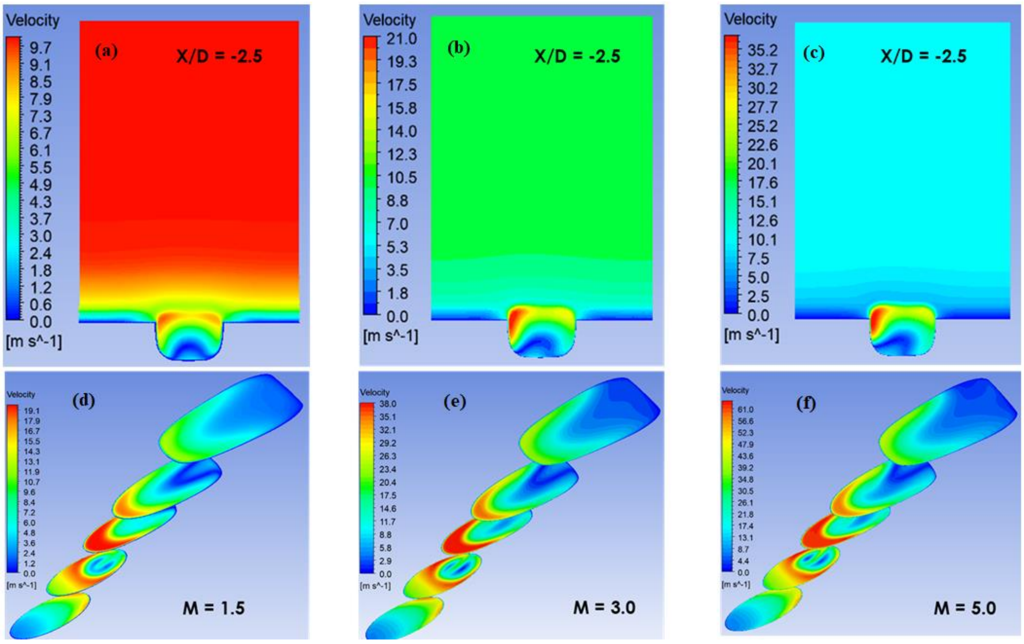

Figure 4-45: Velocity contours of h/D = 0.25 on in-trench planes of (a), (b), (c) and in-hole planes of (d), (e), (f)

Figure 4-45 has shown velocity contour plots of h/D = 0.25 on in-trench planes which were created inside the trench (x/D = -2.5) and on in-hole planes which were created inside the cooling hole. As shown in (d) plot in Figure 4-45, high velocity coolant jet region and the separation bubble (or low momentum region) inside the hole have formed symmetrically at low blowing ratio such as M = 1.5. Velocity distribution after the injection has developed symmetrically as shown in plot (a) due to the symmetricity of in-hole velocity distribution. As a result, the coolant has ejected symmetrically on the surface thereby showing symmetric effectiveness pattern on the surface. Therefore it has not shown a skewness of film cooling effectiveness on the surface at M = 1.5. However, velocity plots on in-hole planes at higher blowing ratios such as M = 3, 5 have shown non-symmetric distribution near the hole exit. It can be observed that the separation bubble has developed with a displacement to left side wall of the hole. As a result, high velocity jet region inside the hole has displaced to left side wall near the hole exit as shown in plots (e) and (f), whereby a high velocity region on the in-trench planes has developed at left side lateral edges of the hole exit as shown in plots (b) and (c). Due to this flow field developed inside the diffuser section of the hole, the coolant jet has shown skewness and developed non-symmetrically in downstream. Consequently, film cooling effectiveness distribution has shown the skewness relative to the geometric center line.

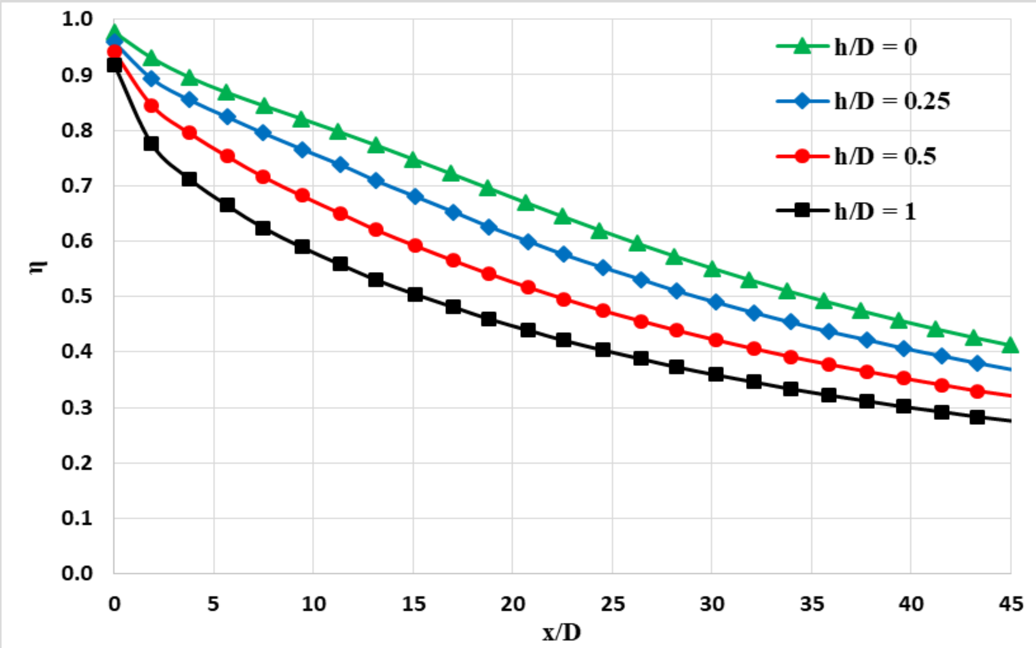

Figure 4-46: Local effectiveness along centerline, M = 1.5

Figure 4-46, Figure 4-47, and Figure 4-48 have illustrated the variation of adiabatic film cooling effectiveness along the centerline. At each blowing ratio and except baseline case, the jet of h/D = 0.25 has produced higher film cooling effectiveness along the centerline in immediate downstream region of x/D < 5 while far downstream region of x/D > 15, h/D = 1 jet has shown the higher cooling performance.

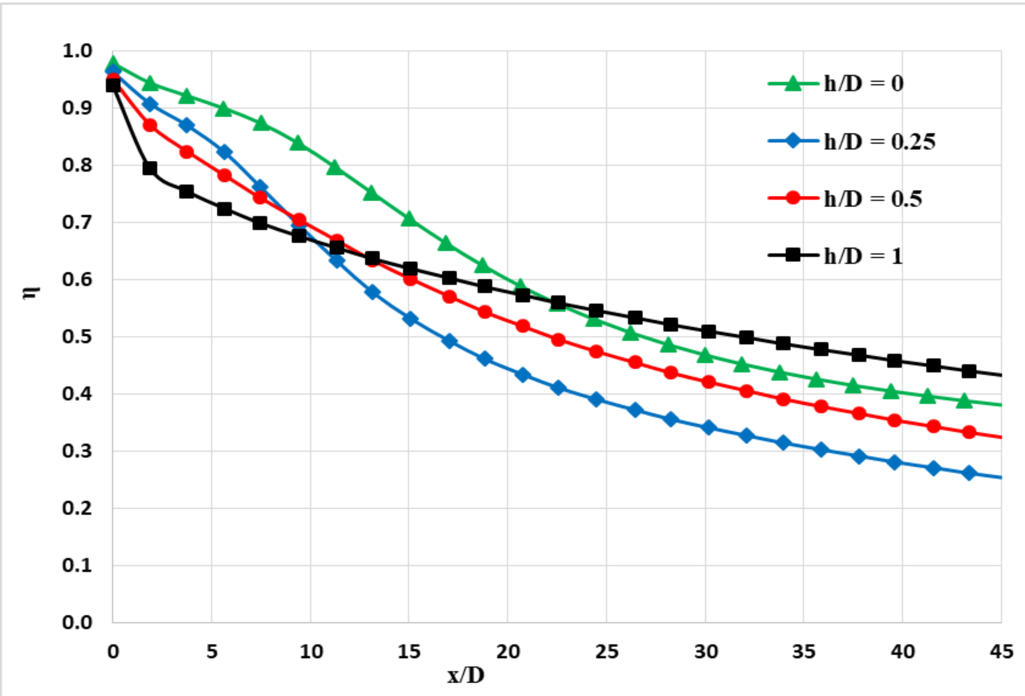

Figure 4-47: Local effectiveness along centerline, M = 3

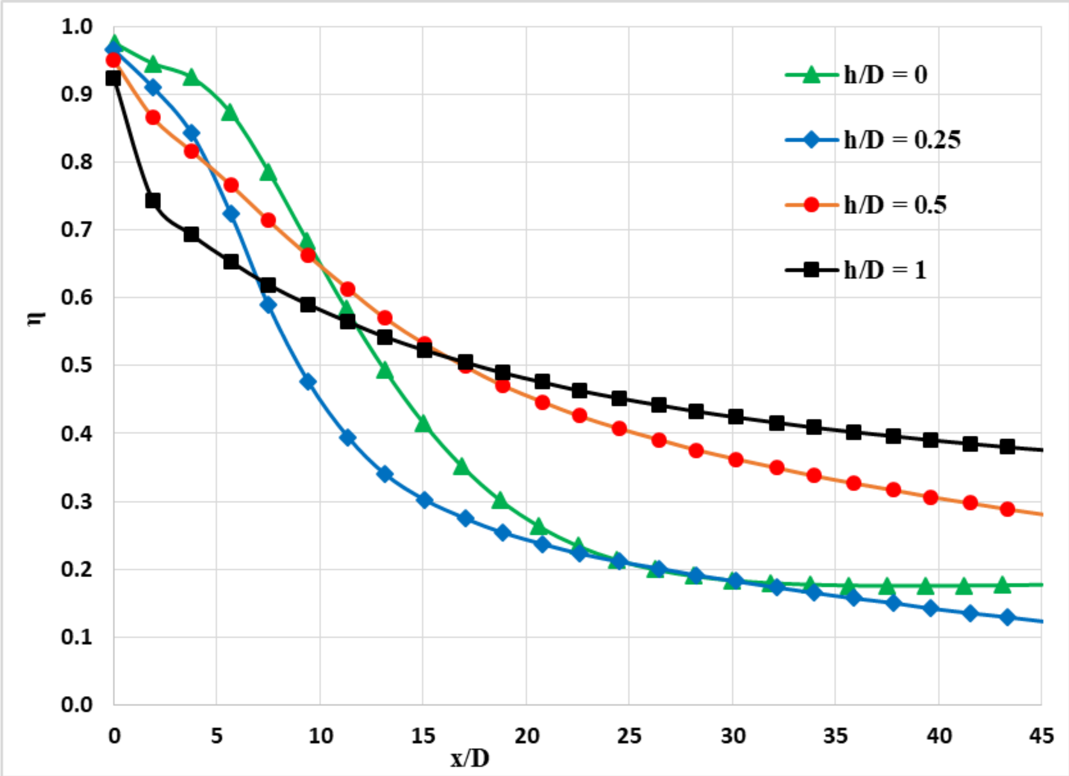

Figure 4-48: Local effectiveness along centerline, M = 5

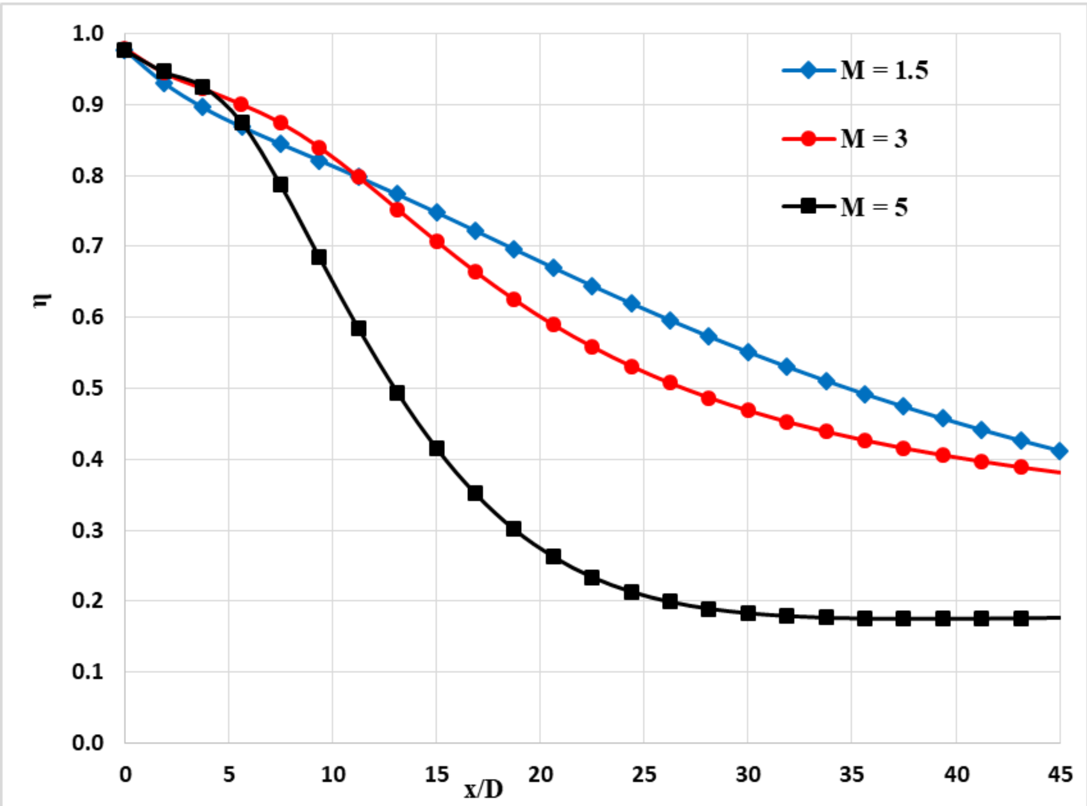

Figure 4-49: Local effectiveness along centerline, h/D = 0

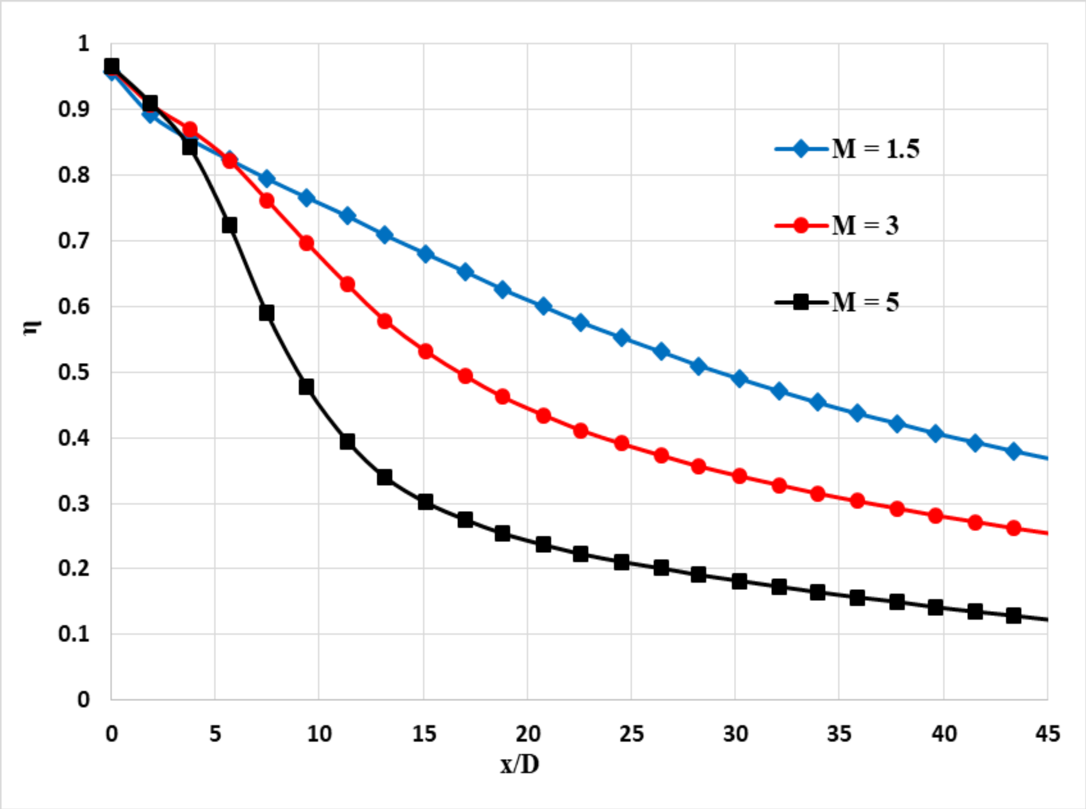

Figure 4-50: Local effectiveness along centerline, h/D = 0.25

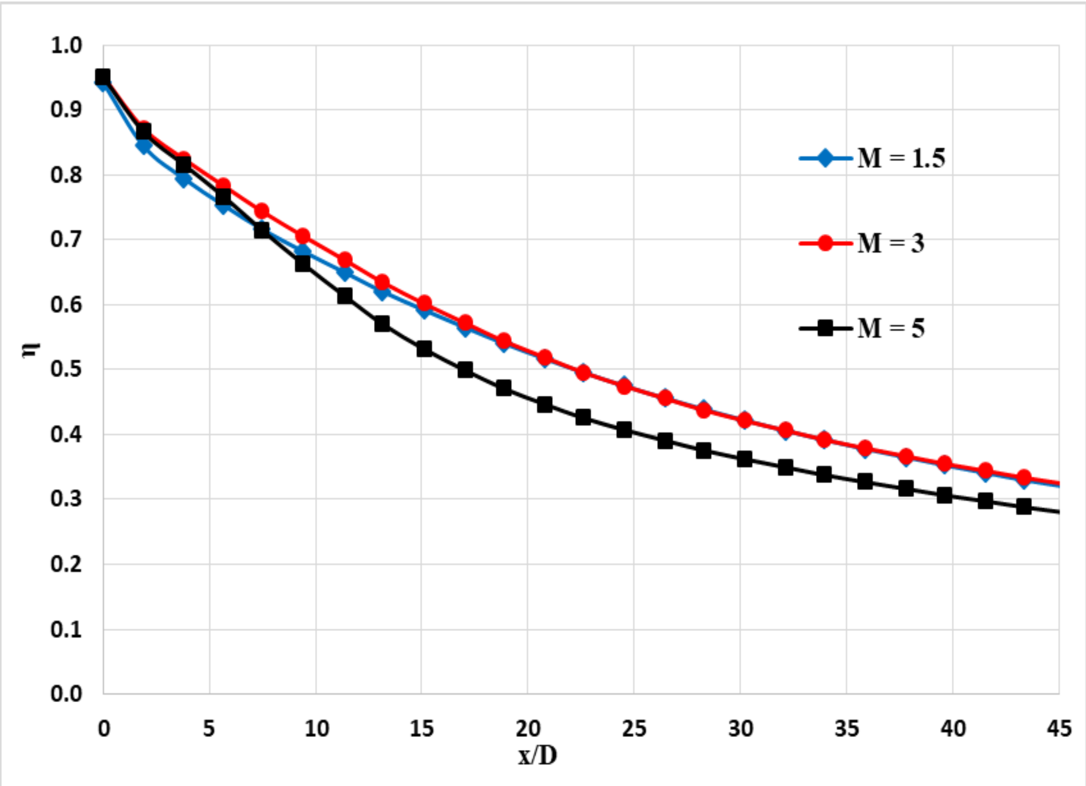

Figure 4-51: Local effectiveness along centerline, h/D = 0.5

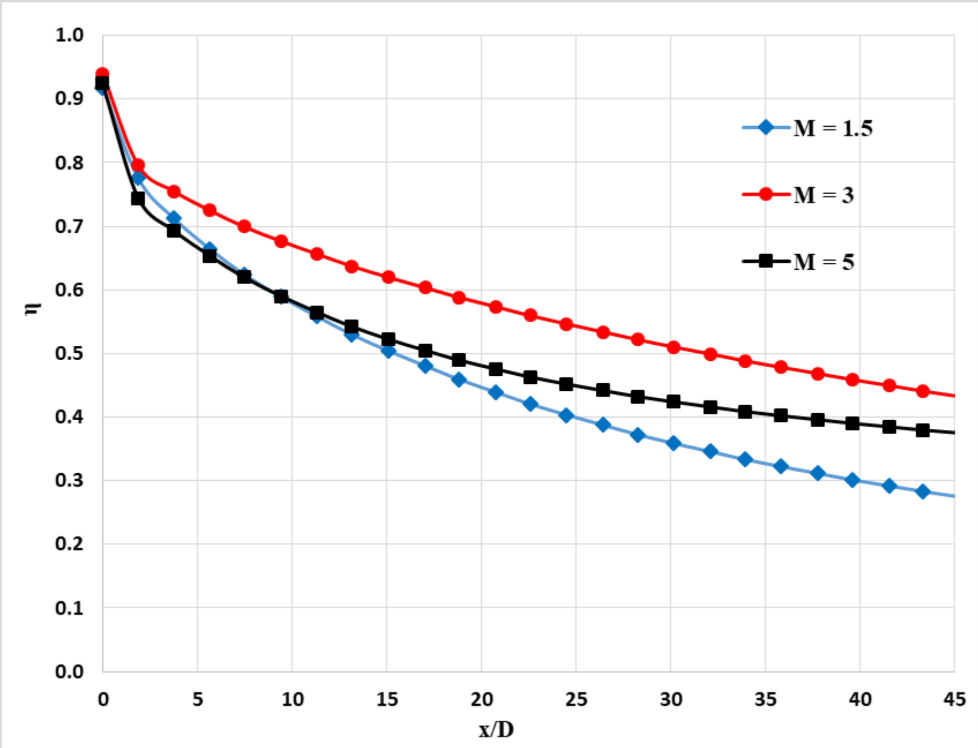

Figure 4-52: Local effectiveness along centerline, h/D = 1

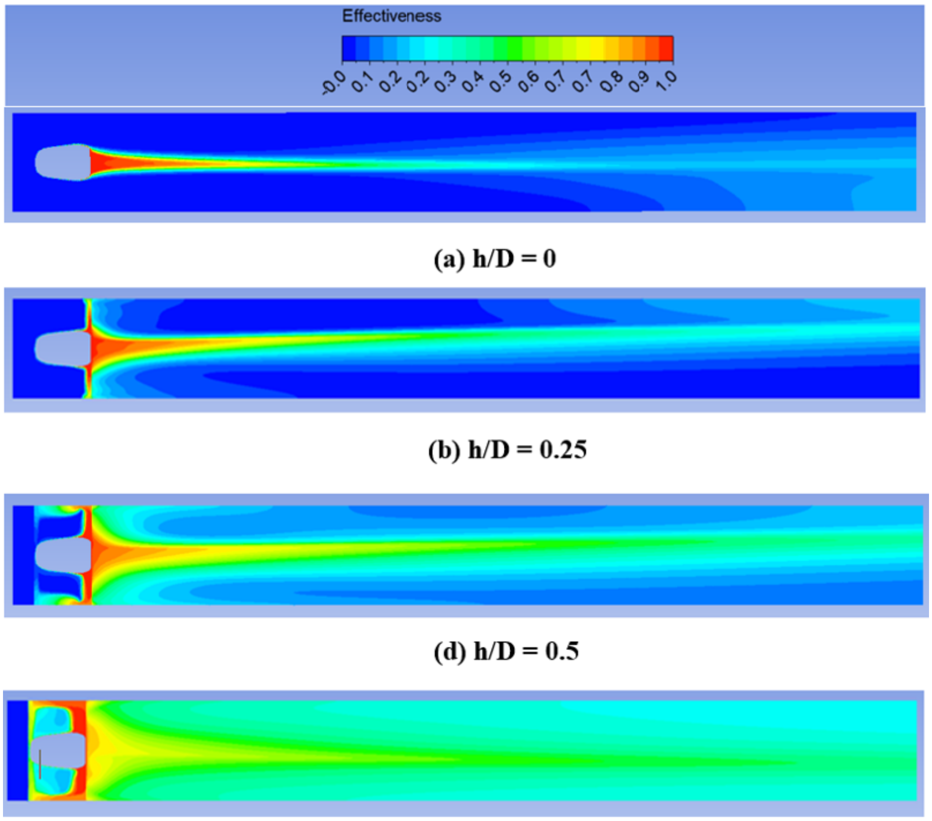

(a) h/D = 0

(b) h/D = 0.25

(d) h/D = 0.5

(c) h/D = 1

Figure 4-53: Local effectiveness contours of M = 5 at various slot depths

At all slot depths of h/D = 0.25, 0.5, and 1as shown in Figure 4-50, Figure 4-51, and Figure 4-52, centerline film cooling effectiveness has not shown a noticeable difference between each blowing ratios in the immediate downstream of x/D < 5. At h/D = 0.25 as shown in Figure 4-50, the effectiveness decreases when increasing blowing ratio. At h/D = 0.5 as shown in Figure 4-51, M = 0.25 and 0.5 cases have not shown significant difference in cooling effectiveness while the centerline effectiveness at M = 5 is noticeable and below the effectiveness values of other two cases. At h/D = 1, the highest effectiveness variation was observed at M = 3.0 as shown in Figure 4-52 whereby higher cooling performance has been provided by M = 3 jet. In general, if higher cooling effectiveness is needed with higher blowing ratios the higher slot depths should be used. If the higher effectiveness with lower blowing ratios is expected the lower slot depths should be used.

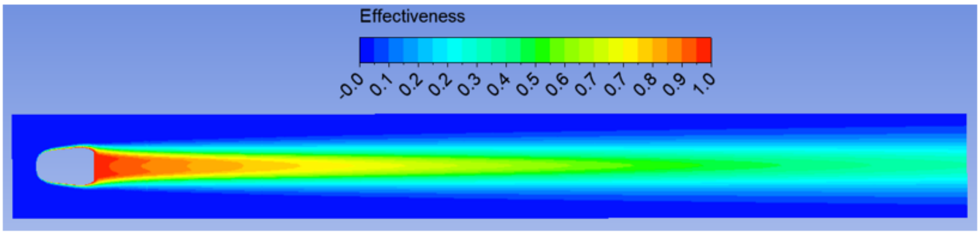

(a) h/D = 0

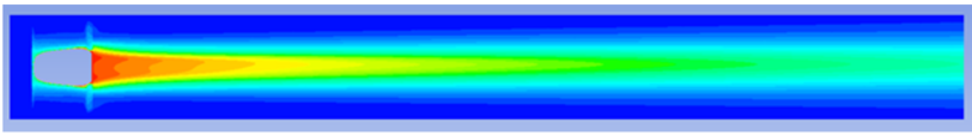

(b) h/D = 0.25

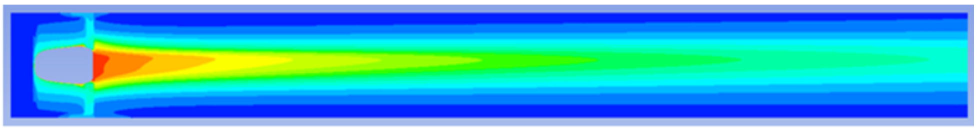

(c) h/D = 0.5

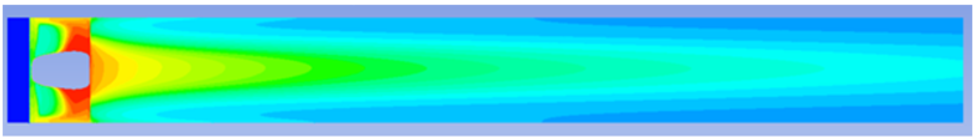

(d) h/D = 1

Figure 4-54: Local adiabatic effectiveness contours of M = 1.5 at various slot depths

Figure 4-53 shows that the coolant accumulation in the trench increases with increasing slot height. As a results, the highest adiabatic effectiveness on the surface takes place in the trench. As shown in Figure 4-53, narrowing the jet can be seen at low slot depths, h/D = 0.25 with higher blowing ratio due to the jet penetration. The coolant accumulation in the trench and strong lateral spreading can be observed as shown in Figure 4-54.

Figure 4-48 and Figure 4-50 have shown noticeable decay particularly with higher blowing ratio such as M = 5 and lower trench depth ratio such as h/D = 0.25. Both of jet penetration as well as jet skewness are thought to be the source for this decay. The graphs of centerline cooling effectiveness were drawn along the geometric centerline. However, it is expected to have deviation between geometric centerline and actual jet centerline due to the jet skewness. As a result, the deviation is affected the decay. In addition to that, the jet penetration into the mainstream contributes to the decay due to weak contact between coolant flow and the surface.

4.3 Mean flow field

As expected by the simulation, a low momentum region formed in the leeward side of the hole and the coolant concentrates to the windward side of the hole as shown in Figure 4-55. The windward region where the concentrated fluid forms high velocity jet, which is called jetting effect shown in the past studies. This effect is a result of the non-uniform velocity distribution at the diffuser's inlet and a huge turn of the fluid in the entry region, which can be seen in Figure 4-55.

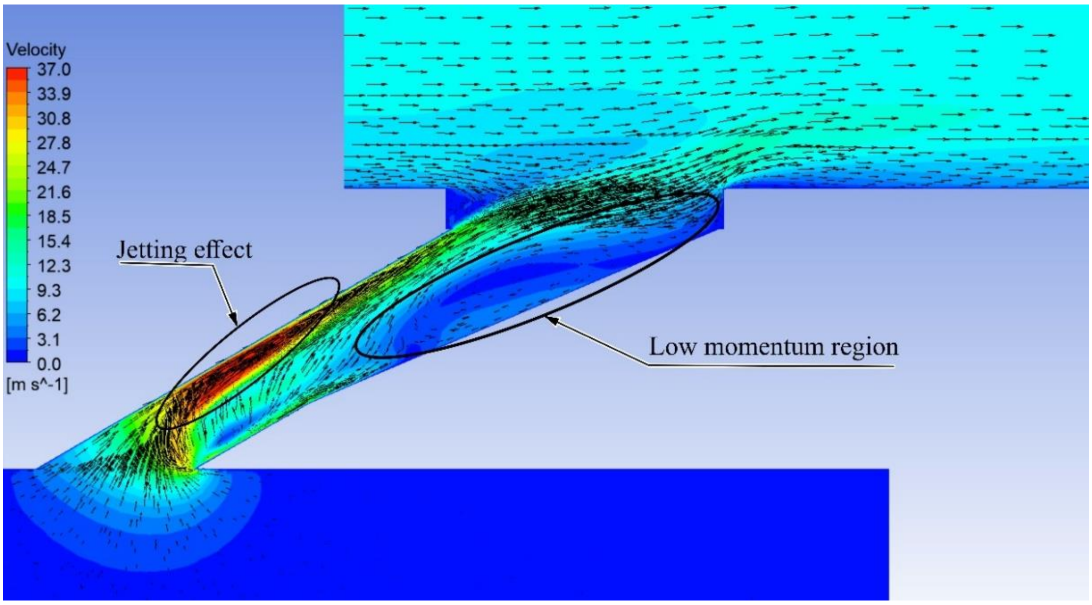

Figure 4-55: Specific flow phenomena in shaped film holes

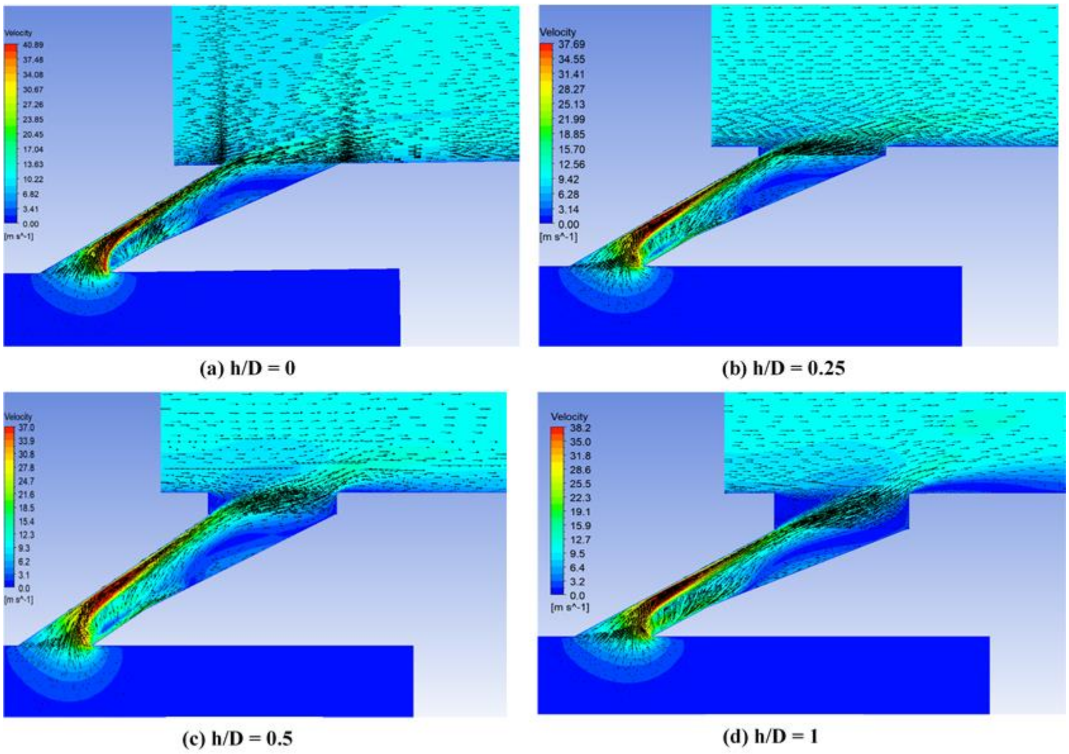

Figure 4-56: Jetting effect at M = 3 with different sloth depths

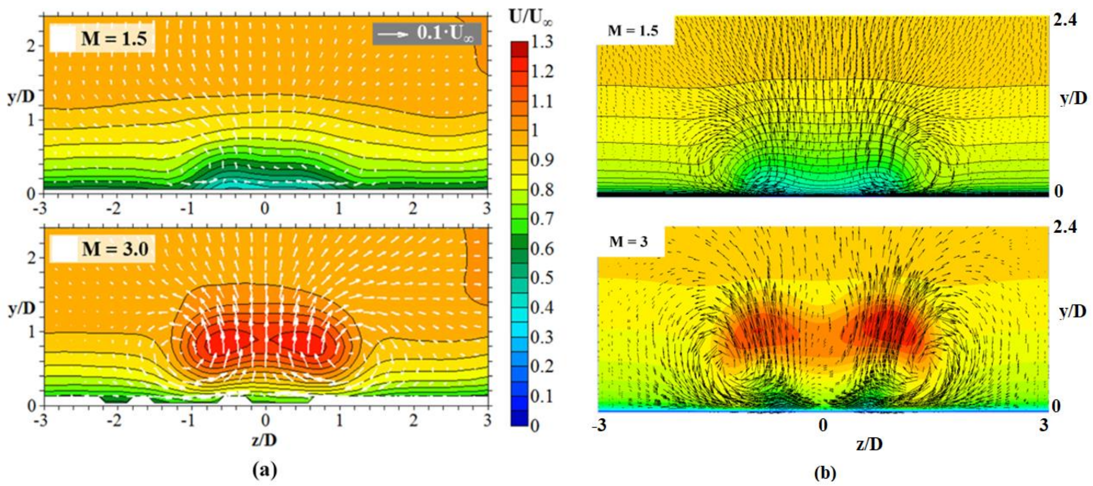

Figure 4-57: Streamwise velocity contours on x/D = 1.6 cross plane for DR = 1.5 and Tu = 0.5%
(a) experimental results [25] (b) present study

As shown in Figure 4-56, the low momentum region has shown extending to further downstream and also to the slot region when increasing the slot depth while the spatial extension of the jet region is similar in different slot depths. Therefore it can be seen that that the spatial extension of the low momentum region is affected by the slot depth. Figure 4-56 shows the jetting effect in the hole with the high velocity jet region and low momentum region at M = 3 with varying slot depth. Highest velocity in the jet region and lowest velocity in the leeward side of the hole are not distinct at different slot depths. As depicted by Figure 4-57, the simulated results generated by the present study has shown similar behavior as shown by experimental results. It can be seen that the CRVP is located above at M = 3 compared to that at M = 1.5.

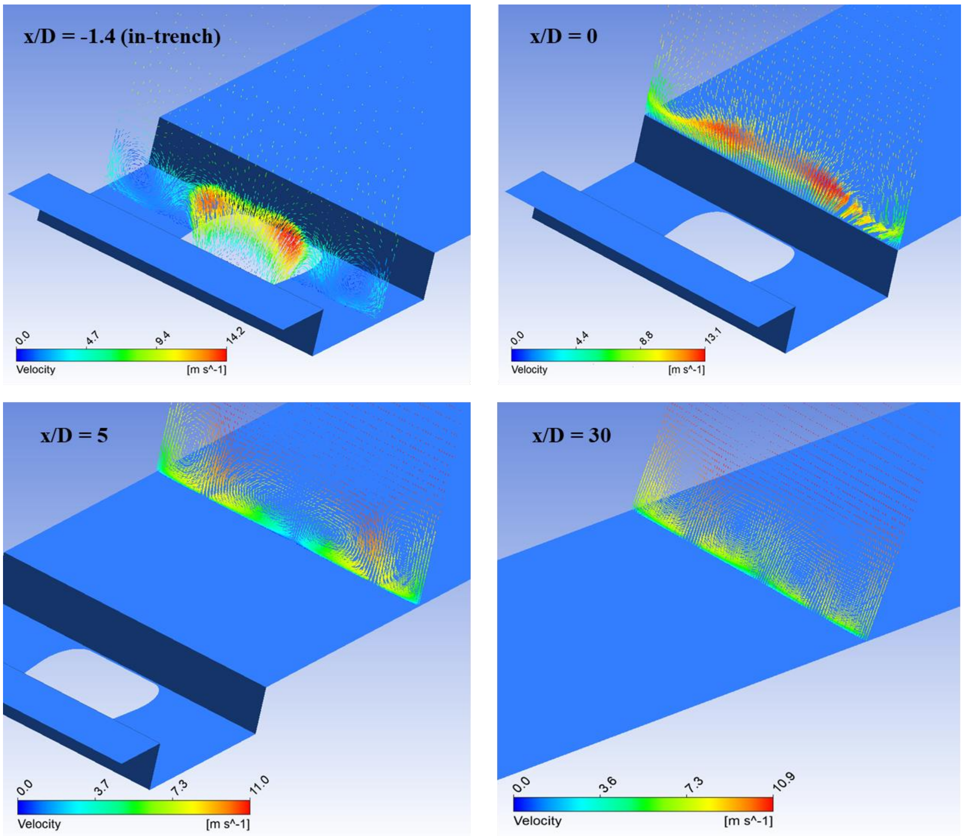

Figure 4-58: Velocity vector plots at different streamwise locations for M = 3 and h/D = 1

Figure 4-58 has shown the velocity vector plots and vortices generated in the flow. Two vortex pairs can be observed in the downstream of the injections location as shown in Figure 4-59. The left side vortex in vortex pair 2 formed in the far lateral sides is clockwise direction while the other vortex in the pair is in anticlockwise direction. This vortex pair is thought to be generated due to the interaction with the trench by mainstream. Vortex pair 1 has formed around the center line region as shown in Figure 4-59. The left side vortex in the pair is in anticlockwise direction while the other vortex is in clockwise direction. Vortex pair 1 is thought to be generated due to the shear between mainstream and coolant jet after the downstream edge of the trench. Figure 4-60 has depicted the variation of vorticity in X direction and the changes of the direction of rotation of vortices. Due to this vortex system, superior lateral spreading of the coolant can be observed in the cases of h/D = 1 at M = 3 as shown in Figure 4-44, Figure 4-53, Figure 4-54. The same vortex system can be identified for the other blowing ratios for h/D = 1 cases. In addition, the vortex system has diminished the jet lift-off and hot gas entrainment for the coolant flow as well as the coolant jet improves its contact to the surface thereby improving cooling effectiveness.

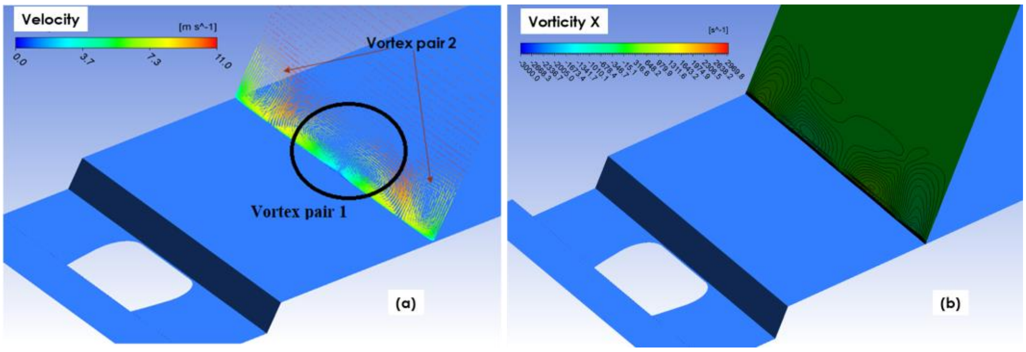

Figure 4-59: For M = 3 and h/D = 1 at X/D = 5 (a) Vortex pairs (b) Vorticity in X direction

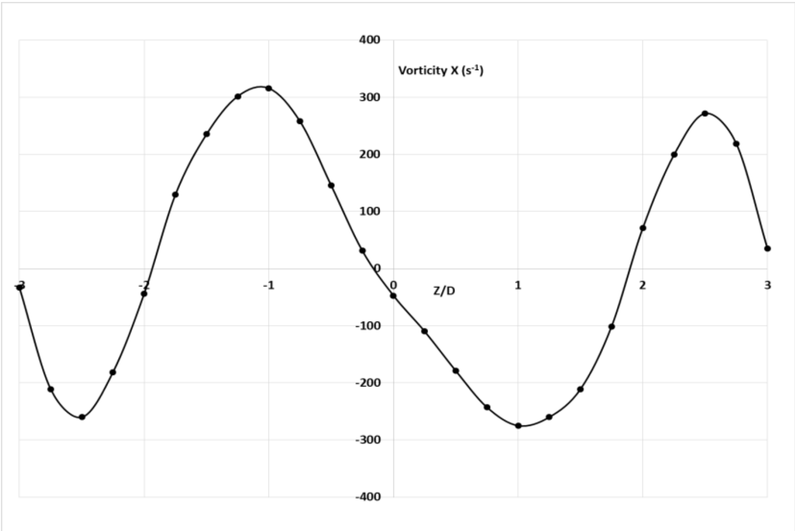

Figure 4-60: Variation of Vorticity in X direction along Y/D = 0.25 line at X/D = 5 for M =3

The vortical structures with trench depth ratio can be seen in Figure 4-61. Higher trench depths have created several vortex pairs over the lateral expansion. These vortical structures were thought to be the source for superior lateral spreading of coolant at higher trench depth ratios.

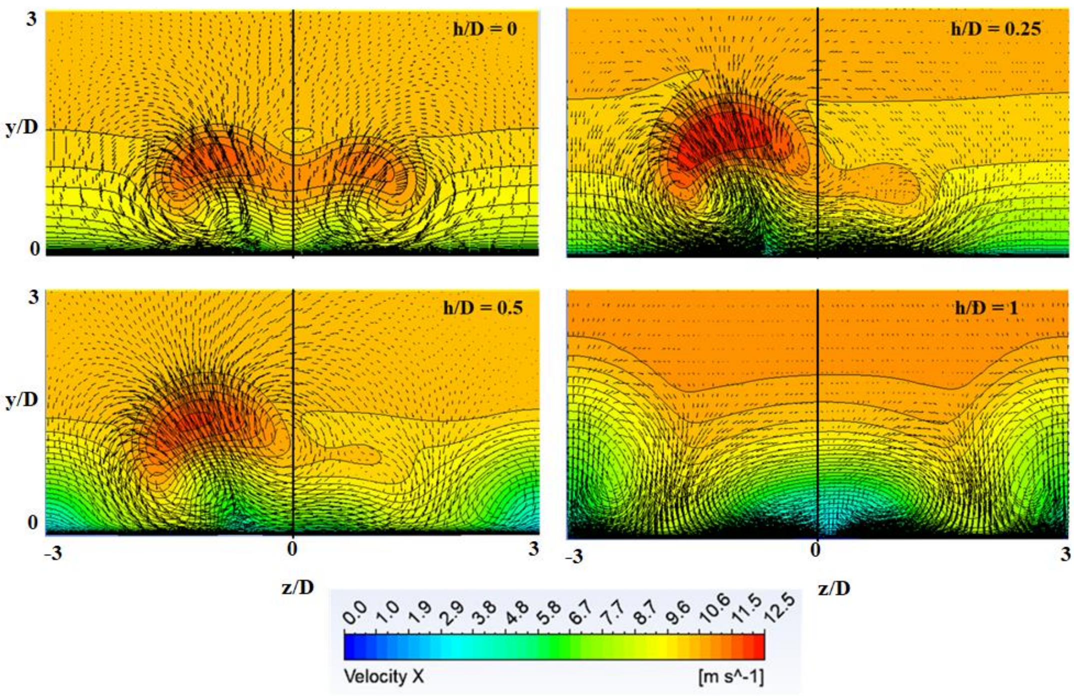

Figure 4-61: Streamwise velocity and velocity vectors at x/D = 5 for M = 3

5 CONCLUSION

The effect of geometry modification made at 7-7-7 shaped hole exit on the cooling performance was studied in the current study. A trench (or called transverse continuous slot) at the hole exit was made and numerical simulation was performed using realizable k-ε model with enhanced wall treatments as implemented in Ansys Fluent solver. The predicted results with varying geometry parameter of the trench, which was the depth ratio of the trench, have been discussed in detail and identified general behavior and trends of film cooling effectiveness and flow field.

5.1 Validation

Three cases of 7-7-7 shaped hole with M = 1.5 and 3, DR = 1.5 and Tu = 0.5% have been simulated in Ansys Fluent using standard k-ω, SST k-ω, and Realizable k-ε turbulence models. Realizable k-ε model with enhanced wall treatment has well-predicted the experimental results of laterally averaged film cooling effectiveness. The same model has simulated a similar effectiveness pattern in the lateral direction compared to the experimental results while the other two have shown a bimodal pattern. The bimodal effectiveness pattern cannot be found in the shaped hole having lower expansion angles due to the reduced effect from the separation region created inside the diffuser section. It can be stated that this effect was inaccurately calculated by standard and SST k-ω models. The increase in lateral spreading of the effectiveness in the downstream has been captured by realizable k-ε model compared to the other two models. The prediction of similar pattern in lateral direction by realizable k-ε model has implied that the effect of vortex structure in the cross-flow generated by the shaped hole on the adiabatic film cooling effectiveness is modeled to a reasonable level since the vortices contribute more on lateral spreading and cooling effectiveness. Based on the error analysis, R^2 value for the laterally averaged effectiveness predictions of RKE was 0.923 and 0.798 for M =1.5 and 3 respectively compared to the other models. Due to the over-prediction of centerline effectiveness, the R^2 values were very low for the all turbulence models.

The three turbulence models produced the three velocity profiles at different cross-flow locations. The velocities from experiments are well predicted by realizable k-ε model in comparison to other two models. Velocity contours of simulations have also shown the CRVP very close to the results presented by experimental results on cross-planes in the cross-flow downstream. In addition, RMSE of RKE for velocity profiles was lower than that of other models. At least a 200% increase could be observed in RMSE of SKW and SST KW compared to RKE model. The higher R-square values are available for RKE model at the all locations for M = 1.5 and 3 except x/D = -2.4 for M = 3 due to the very large deviation of predicted results from experimental results in the region below y/D = 0.5. It represents the best fit of the RKE predictions to the experimental results. Based on the error analyses, the comparison of flow field patterns and cooling effectiveness variations, the realizable k-ε model with enhanced wall treatment was selected to predict the modified geometry.

5.2 Cooling performance of shaped hole with trench

Realizable k-ε model with enhanced wall treatment was used to produce numerical results for 7-7-7 shaped hole with three different trench depth ratios. Altogether nine cases were simulated at M = 1.5, 3, and 5 with h/D = 0.25, 0.5, and 1 for DR = 1.5 and Tu = 0.5%. It was expected to identify the general trends and patterns of cooling effectiveness with the effect of depth ratio of the trench at different blowing ratios. Key conclusions and findings from this study are listed below.

- Shaped hole with trench presents better cooling effectiveness in comparison to the baseline case according to the laterally averaged effectiveness
- Superior lateral spreading was observed at higher depth ratio of trench relative to the baseline case.
- According to the laterally averaged effectiveness, the cooling effectiveness is improved by increasing the slot depth at all blowing ratios investigated.
- At h/D = 1, a plateau can be observed when increasing blowing ratio. Same effectiveness can be observed at M = 3 and 5. The lowest possible blowing ratios in the plateau region can be used in the actual designs in order to reduce the coolant flow rate.
- At h/D = 0.5, downstream averaged film cooling effectiveness has not shown significant difference among the three blowing ratios although a noticeable difference can be observed near the hole exit.
- Maintaining higher blowing ratios at lower slot depth ratio such as h/D = 0.25 is only a waste of coolant without improvements to cooling performance.

- Superior lateral spreading of coolant has shown at h/D = 1 at each blowing ratio.
- Based on the local lateral effectiveness variations, the coolant jet has shown a skewness at higher blowing ratios and lower slot depth ratios while the skewness becomes invisible at lower blowing ratios and lower slot depths.
- A steeper decay can be seen in laterally averaged effectiveness at higher blowing ratios (M = 5) and low slot depth ratios (h/D = 0.25) due to the jet penetration thereby degrading the cooling effectiveness.
- The coolant accumulation in the trench increases with increasing slot height. As a result, the highest adiabatic effectiveness on the surface takes place in the trench.
- A considerable decay can be observed in laterally averaged film cooling effectiveness at low blowing ratio of M = 1.5 when increasing the sloth depth due to the mainstream ingestion near the diffuser outlet. The jet momentum decreases furthermore with higher slot depth thereby leading to more mainstream ingestion and reducing cooling effectiveness.

5.3 Significance and recommendations for future work

The present study has been conducted totally based on RANS turbulence model of realizable k-ε with enhanced wall treatment which cannot inherently solve for unsteady flow field. However general trends, important observations and findings were identified with the model. Complex vortical flow structures are expected to generate with the trenched shaped holes in in-hole and the hole outside, which cannot be accurately captured their effects on the cooling behavior. It is suggested that to perform higher level unsteady simulations such as LES to verify the results and identified trends. It would be worth to perform experimental studies to validate these results and to enhance the experimental database in literature. On the other hand, turbulent diffusion, particularly in near hole region and in centerline region, is not constant in the cross-flow due to the jet-mainstream interaction. In addition, turbulent prandlt number is not constant and not equal to 1 over these regions. This contributes extensively on thermal energy transport in coolant jet region whereby the cooling effectiveness reduces in the centerline region. The turbulent transport is barely captured by Reynolds averaged method. The effects of these turbulent flow features on cooling performance of 7-7-7 shaped hole are interested in understanding by using higher order simulations as well as investigating possibilities to improve RNAS turbulence model are also important.

6 REFERENCES

[1] J. C. Han, S. Dutta and S. Ekkad, Gas Turbina Heat Transfer and Cooling Technology, CRC Press, Taylor & Francis Group, 2013.

[2] Y. A. Cengel and M. A. Boles, Thermodynamics - An Engineering Approach, 2008.

[3] R. P. Schroeder, *Influence of In-hole Roughness and High Free Stream Turbulance on Film Cooling From Shaped Hole,* PhD, 2015.

[4] D. G. Bogard and K. A. Thole, "Gas Turbine Film Cooling," *Journal of Propulsion and Power,* vol. 22, no. 2, pp. 249-270, 2006.

[5] S. Nikolaos, "Large Eady Simulation of the Film Cooling Flow Systems of Turbine Blades: Public Shaped Hole," 2016.

[6] R. J. Goldstien, "Film Cooling," in *Advances in Heat Transfer*, 1971, pp. 321-379.

[7] D. G. Bogard, "Airfoil film cooling".

[8] B. Sen, D. L. Schmidt and D. G. Bogard, "Film cooling with compound angle holes: heat transfer," *Journal of Turbomachinery,* vol. 118, pp. 800-807, 1996.

[9] S. M. Bauldauf, A. Schulz and S. Witting, "High resolution measurements of local effectiveness from discrete hole film cooling," *Journal of Turbomachinery,* vol. 123, pp. 758-765, 2001.

[10] R. S. Bunker, "A Review of Shaped Hole Turbine FilmCooling Technology," *Journal of Heat Transfer,* vol. 127, pp. 441-453, 2005.

[11] R. Hou, F. Wen, Y. Luo, X. Tang and S. Wang, "Large eddy simulation of film cooling flow from round and trenched holes," *International Journal of Heat and Mass Transfer,* vol. 144, 2019.

[12] R. S. Bunker, "Film cooling effectiveness due to discrete holes within a transverse surface slot," in *ASME Turbo Expo 2002,* Ntherland, 2002.

[13] C. Saumweber and A. Schulz, "Effect of Geometry Variations on the Cooling Performance of Fan-Shaped Cooling Holes," *Journal of Turbomachinery,* vol. 134, November 2012.

[14] R. J. Goldstein, E. R. G. Eckert and J. W. Ramsey, "Film Cooling With Injection Through Holes: Adiabatic Wall Temperatures Downstream of a Circular Hole," *Journal of Engineering and Power,* pp. 384-392, 1968.

[15] R. J. Goldstein, E. R. G. Eckert, V. L. Eriksen and J. W. Ramsey, "Film Cooling Following Injection Through Inclined Circular Tubes," NASA, 1969.

[16] J. W. Ramsey and R. J. Goldstein, "Interaction of a Heated Jet With a Diflecting Stream," *Journal of Heat Transfer,* pp. 365-371, 1971.

[17] J. Dittmar, A. Schulz and S. Wittig, "Assessment of Various Film-Cooling Configurations Including Shaped and Compound Angle Holes Based on Large-Scale Experiments," *Journal of Turbomachinery,* vol. 125, pp. 57-64, 2003.

[18] R. J. Goldstein, E. R. G. Eckert and F. Burggraf, "Effects of Hole Geometry and Density on Three-Dimensional Film Cooling," *Interanational Journal of Heat Mass Transfer,* vol. 17, pp. 595-607, 1974.

[19] M. Gritsch, W. Colban, H. Schär and K. Döbbeling, "Effect of Hole Geometry on the Thermal Performance of Fan-Shaped Film Cooling Holes," *Journal of Turbomachinery,* vol. 127, no. 4, pp. 718-725, 2005.

[20] C. Saumweber and A. Schulz, "Free-Stream Effects on the Cooling Performance of Cylindrical and Fan-Shaped Cooling Holes," *Journal of Turbomachinery,* vol. 134, 2012.

[21] M. Gritsch, A. Schulz and S. Wittig, "Adiabatic Wall Effectiveness Measurements of Film-Cooling Holes With Expanded Exits," *Journal of Turbomachinery,* vol. 120, pp. 549-556, 1998.

[22] C. Saumweber, A. Schulz and S. Wittig, "Free Stream Turbulance Effects on Film Cooling with Shaped Holes," in *ASME TURBO EXPO 2002,* Amsterdam, The Netherlands, 2002.

[23] T. a. d. Kampe, S. Vo¨lker, T. Sa¨mel, C. Heneka, H. Ladisch, A. Schulz and H.-J. Bauer, "Experimental and Numerical Investigation of Flow Field and Downstream Surface Temperatures of Cylindrical and Diffuser Shaped Film Cooling Holes," *Journal of Turbomachinery,* vol. 135, p. 011026, 2013.

[24] R. P. Schroeder and K. A. Thole, "Adiabatic effectiveness measurements for a baseline shaped film cooling hole," in *ASME Turbo Expo 2014: Turbine Technical Conference and Exposition*, Dusseldorf, Germany, 2014.

[25] R. P. Schroeder and K. A. Thole, "Effect of high freestream turbulence on flowfields of shaped film cooling holes," *Journal of Turbomachinery,* vol. 138, 2016.

[26] K. Thole, M. Gritsch, A. Schulz and S. Witting, "Flowfield measurements for film cooling holes with expanded exit," *Journal of Turbomachinery,* vol. 120, no. 2, pp. 327-336, 1998.

[27] J. H. Leylek and R. D. Zerkle, "Discrete-Jet Film Cooling: A Comparison of Computational Results With Experiments," *Journal of Turbomachinery,* vol. 116, pp. 358-368, 1994.

[28] D. K. Walters and J. H. Leylek, "A Detailed Analysis of Film-Cooling Physics: Part I—Streamwise Injection with Cylindrical Holes," *Journal of Turbomachinery,* vol. 122, pp. 102-112, 2000.

[29] D. G. Hyams and J. H. Leylek, "A Detailed Analysis of Film-Cooling Physics: Part III—Streamwise Injection with Shaped Holes," *Journal of Turbomachinery,* vol. 122, pp. 122-132, 2000.

[30] S. I. Kim and I. Hassan, "Unsteady Simulations of a Film Cooling Flow from an Inclined Cylindrical Jet," *J. Thermophys. Heat Transf.,* vol. 24, p. 145–156, 2010.

[31] R. M. Kelso, T. T. Lim and A. E. Perry, "An Experimental Study of Round Jets in Cross-Flow," *J. Fluid Mech,* vol. 306, p. 111–144, 1996.

[32] L. L. Yuan, R. L. Street and J. H. Ferziger, "Large-eddy simulations of a round jet in crossflow," *J. Fluid Mech.,* vol. 379, p. 71–104, 1999.

[33] X. Guo, W. Schroder and M. Meinke, "Large-Eddy Simulations of Film Cooling Flows.," *Comput. Fluids* , vol. 35, p. 587–606, 2006.

[34] T. F. FRIC and A. ROSHKO, "Vortical structure in the wake of a transverse jet," *J. Fluid Mech.,* vol. 279, pp. 1-47, 1994.

[35] J. E. BROADWELL and R. E. BREIDENTHAL, "Structure and mixing of a transverse jet in incompressible flow," *J . Fluid Mech.,* vol. 148, pp. 405-412, 1984.

[36] Y. M. M. Arzouk and A. F. Ghoniem, "Vorticity structure and evolution in a transverse jet," *J. Fluid Mech.* , vol. 575, p. 267–305, 2007.

[37] F. Schlegel, D. Wee, Y. . M. M. Arzouk and A. F. Ghoniem, "Contributions of the wall boundary layer to the formation of the counter-rotating vortex pair in transverse jets," *J. Fluid Mech.,* vol. 676 , p. 461–490, 2011.

[38] B. A. Haven, D. K. Yamagata, M. Kurosaka , S. Yamawaki and T. Maya, "Anti-kidney pair of vortices in shaped holes and their influence on film cooling effectiveness," in *ASME International Gas Turbine and Aeroengine Congress*, 1997.

[39] H. M. Li, W. Ghaly and I. Hassan, "The formation of counter-rotating vortex pair and the nature of liftoff-reattachement in film cooling flow," *Fluids,* vol. 1, no. 4, 2016.

[40] K. L. Harrison and D. G. Bogard , "Comparison of RANS turbulance models for prediction of film cooling performance," in *ASME Turbo Expo 2008: Power for Land, Sea and Air*, Germany, 2008.

[41] D. K. Walters and J. H. Leylek, "A Systematic Computational Methodology Applied to a Three-Dimensional Film-Cooling Flowfield," *Journal of Turbomachinery,* vol. 119, pp. 777-785, 1997.

[42] X. Z. Zhang and I. Hassan, "Numerical investigation of heat transfer on film cooling with shaped holes," *International Journal of Numerical Methods for Heat & Fluid Flow,* vol. 16, no. 8, pp. 848-869, 2006.

[43] S. Haydt and S. Lynch, "Cooling effectiveness for a shaped film cooling hole at a range of compound angles," *Journal of Turbomachinery,* vol. 141, 2019.

[44] A. M. M. Abdala and F. N. M. Elwekeel, "CFD simulations of film cooling effectiveness and heat transfer for annular film hole," *Arab J Sci Eng,* 2016.

[45] J. Dickhoff, K. Kusterer, S. K. Bhaskar and D. Bohn, "Comparison between different isotropic and anisotropic eddy viscosity models," in *Turbomachinery Technical Conference and Exposition GT2018*, Norway, 2018.

[46] A. Minj, A. K. Roy and K. Kumar, "Modeling and simulation of film cooling effectiveness on a flat plate," in *International Conference on Materials Manufacturing and Modelling*, 2019.

[47] X. Tan, X. Zhou, Y. Shan and J. Zhang, "Analysis of heat transfer on film cooling performance in a flat plate," in *International Conference on Applied Energy*, Hong-Kong, 2019.

[48] S. I. Kim and I. Hassan, "Unsteady simulations of a film cooling flow from an inclined cylindrical jet," *Journal of thermophysics and heat transfer*, vol. 24, no. 1, 2010.

[49] W. A. Acosta, D. R. Thurman and P. Poinsatte, "Preliminary computational analysis of film cooling on a flat plate at different blowing ratios," Cleveland, 2020.

[50] L. Zhong, C. Zhou and S. Chen, "Large Eddy Simulation of Inclined Jet in Cross Flow with Cylindrical and Fan-shaped Holes," in *ASME Turbo Expo 2016: Turbomachinery Technical Conference and Exposition*, Seoul, South Korea, 2016.

[51] P. Renze, W. Schro¨der and M. Meinke, "Large-eddy simulation of film cooling flows at density gradients," *International Journal of Heat and Fluid Flow,* vol. 29, p. 18–34, 2008.

[52] Y. V. Peet and S. K. Lele, "Near field of film cooling jet issued into a flat plate boundary layer: LES study," in *ASME Turbo Expo 2008: Power for Land, Sea and Air*, Germany, 2008.

[53] E. Sakai, T. Takahashi and H. Watanabe, "Large-eddy simulation of an inclined round jet issuing into a crossflow," *International Journal of Heat and Mass Transfer,* vol. 69, p. 300–311, 2014.

[54] D. H. Leedom and S. Acharya, "Large eddy simulations of film cooling flow fields from cylindrical and shaped holes," in *ASME Turbo Expo 2008: Power for Land, Sea and Air* , Germany, 2008.

[55] S. Acharya and D. H. Leedom, "Large eddy simulations of discrete hole film cooling with plenum inflow orientation effects," *Journal of Heat Transfer* , vol. 135, 2013.

[56] Z. T. Stratton and I. P. Shih, "Effects of density and blowing ratios on the turbulent structure and effectiveness of film cooling," *Journal of Turbomachinery,* 2018.

[57] R. Hou, F. Wen, S. Wang, Y. Luo and X. Tang, "Large eddy simulation of the trenched film cooling hole with different compound angles and coolant inflow orientation effects," *Applied Thermal Engineering,* vol. 163, 2019.

[58] N. Al-Zurfi, A. Turan, A. Nasser and A. Alhusseny, "A numerical study of anti-vortex film-cooling holes designs in a 1-1/2 turbine stage using LES," *Propulsion and Power Research,* vol. 8, no. 4, pp. 275-299, 2019.

[59] T. A. Oliver, D. G. Bogard and R. D. Moser, "Large eddy simulation of compressible, shaped-hole film cooling," *International Journal of Heat and Mass Transfer,* vol. 140, p. 498–517, 2019.

[60] C. Wang, J. Zhang, H. Feng and Y. Huang, "Large eddy simulation of film cooling flow from a fanshaped hole," *Applied Thermal Engineering,* 2017.

[61] N. Al-Zurfi and A. Nasser, "LES of rotating film-cooling performance in a 1-1/2 turbine stage," *Propulsion and Power Research,* vol. 8, no. 2, p. 85–107, 2019.

[62] W. Li, X. Li, J. Ren and H. Jiang, "Large eddy simulation of compound angle hole film cooling with hole length-to-diameter ratio and internal crossflow orientation effects," *International Journal of Thermal Sciences,* vol. 121, pp. 410-423, 2017.

[63] X. Chen and H. Xia, "Hybrid LES-RANS study of an effusion cooling array with circular holes," *International Journal of Heat and Fluid Flow,* vol. 77, pp. 171-185, 2019.

[64] K. Tracy and S. P. Lynch, "Large eddy simulation of the 7-7-7 shaped film cooling hole at axial and compound angle orientation," in *Proceedings of ASME Turbo Expo 2020: Turbomachinery Technical Conference and Exposition*, London, England, 2020.

[65] M. K. Eberly and K. A. Thole, "Time-resolved film-cooling flows at high and low density ratios," *Journal of Turbomachinery,* vol. 136, 2014.

[66] Y. Lu, A. Dhungel, S. V. Ekkad and R. S. unker, "Effect of trench width and depth on film cooling from cylindrical holes embedded in trench," *Journal of Turbomachinery,* vol. 131, pp. 1-13, 2009.

[67] D. C. Wilcox, Turbulence modeling for CFD, La Canada, California: DCW Industries, 1998.

[68] F. R. Menter, "Two-equation edd-viscosity turbulence models for engineering applications," *AIAA Journal,* vol. 32, no. 8, pp. 1598-1604, 1994.

[69] T. H. Shih, W. W. Liou, A. Shabbir, Z. Yang and J. Zhu, "A new - eddy-viscosity model for high Reynolds number turbulent flows," *Computers Fluids,* vol. 24, no. 3, pp. 227-238, 1995.

[70] W. C. Reynolds, "Fundamentals of turbulence for turbulence modeling and simulation," 1987.

[71] ANSYS, "ANSYS Fluent Theory Guide," Ansys Inc, 2013.

[72] H. Tennekes and J. L. Lumley, A first course in turbulence, The MIT Press, 1972.

[73] T. H. Shih, J. Zhu and J. L. Lumley, "A new Reynold stress algebraic equation model," *Computer Methods in Applied Mechanics and Engineering,* vol. 125, pp. 287-302, 1995.

[74] T. F. Fric and A. Roshko, "Vortical structure in the wake of a transverse jet," *J. Fluid Mech.,* vol. 279, 1994.

[75] A. Kohli and D. G. Bogard, "Turbulent transport in film cooling flows," *Journal of Heat Transfer,* vol. 127, pp. 513-520, 2005.

[76] A. Kholi and D. G. Bogard, "Fluctuating thermal field in the near-hole region for film cooling flows," *Journal of Terbomachinery,* vol. 120, pp. 86-91, 1998.

[77] R. W. Keszeta and T. W. Simon, "Measurement of eddy diffusivity of momentum in film cooling flows with streamwise injection," *Journal of Turbomachinery,* vol. 122, pp. 178-183, 2000.

[78] J. R. Pietrzyk, D. G. Bogard and M. E. Crawford, "Hydrodynamic Measurements of Jets in Crossflow for Gas Turbine Film Cooling Applications," *Journal of Turbomachinery,* vol. 111, pp. 139-145, 1989.

[79] M. Tyagi and S. Acharya, "Large Eddy Simulation of Film Cooling Flow From an Inclined Cylindrical Jet," *Journal of Turbomachinery,* vol. 125, pp. 734-742, 2003.

[80] D. H. Leedom, "Numerical investigation of film cooling fluid flow and heat transfer using large eddy simulations," LSU Master's Theses, 2009.